ERDC/CHL TR-21-14

Coastal and Hydraulics Laboratory

US Army Corps
of Engineers®
Engineer Research and
Development Center

Cohesive Sediment Field Study: James River, Virginia

S. Jarrell Smith, David W. Perkey, and Kelsey A. Fall

August 2021

The US Army Engineer Research and Development Center (ERDC) solves the nation's toughest engineering and environmental challenges. ERDC develops innovative solutions in civil and military engineering, geospatial sciences, water resources, and environmental sciences for the Army, the Department of Defense, civilian agencies, and our nation's public good. Find out more at www.erdc.usace.army.mil.

To search for other technical reports published by ERDC, visit the ERDC online library at https://erdclibrary.on.worldcat.org/discovery.

ERDC/CHL TR-21-14
August 2021

Cohesive Sediment Field Study: James River, Virginia

S. Jarrell Smith, David W. Perkey, and Kelsey A. Fall

Coastal and Hydraulics Laboratory
US Army Engineer Research and Development Center
3909 Halls Ferry Road
Vicksburg, MS 39180-6199

Final report

Prepared for US Army Engineer Research and Development Center
Regional Sediment Management Program
Vicksburg, MS 39180-6199

Under Funding Account Code U4356838; AMSCO Code 008303

Abstract

Estuaries trap much of the fine sediment delivered to them by rivers. This phenomenon presents challenges to the US Army Corps of Engineers (USACE) navigation mission, which maintains navigable waterways for waterborne commerce through estuarine regions. The USACE Regional Sediment Management Program and the USACE Norfolk District are conducting a regional sediment transport modeling study to identify cost-effective sediment management schemes in the James River, a tributary estuary of Chesapeake Bay. A key element of the sediment transport modeling study is the definition of cohesive sediment transport processes, such as erosion and settling velocity. This report describes field-based measurements of cohesive sediment erosion and settling velocity conducted in November 2017. The team conducted erosion testing on 15 cores collected throughout the tidal system. Additionally, two anchor stations were occupied to measure tidal variations in vertical distributions of suspended sediment concentration, particle size, and settling velocity. Recommended cohesive sediment transport parameters were developed from the field measurements.

Contents

Figures and Tables

Figures

Tables

Preface

This study was conducted for the US Army Engineer Research and Development Center (ERDC), Regional Sediment Management (RSM) Program under Funding Account Code U4356838; AMSCO Code 008303.

The work was performed by the Field Data Collection and Analysis Branch of the Navigation Division, US Army Engineer Research and Development Center, Coastal and Hydraulics Laboratory (ERDC-CHL). At the time of publication of this report, Mr. William C. Butler was Chief, Field Data Collection and Analysis Branch; Ms. Ashley E. Frey was Chief, Navigation Division; and Dr. Katherine E. Brutsché was the Technical Director for RSM. Mr. Keith W. Flowers was the Deputy Director of CHL, and Dr. Ty V. Wamsley was the Director.

The Commander of ERDC was COL Teresa A. Schlosser, and the Director was Dr. David W. Pittman.

1 Introduction

Background

One of the primary missions of the US Army Corps of Engineers (USACE) is sediment management in navigation channels across the nation. Costs associated with dredging the nation's navigable channels and ports continue to rise along with the environmental regulations associated with these maintenance operations. The USACE Norfolk District (NAO) routinely performs maintenance dredging that includes channel adjacent placement of material along multiple stretches of the James River, Virginia. NAO has previously worked with the US Army Engineer Research and Development Center, Coastal and Hydraulics Laboratory (ERDC-CHL) on sediment transport modeling studies to evaluate the fate of these placed sediments. While evaluating the fate of placed dredged material provided valuable information regarding the efficiencies of the channel adjacent placement practices, it has become apparent that focusing only on the placement of the dredged material has not answered the question of ultimately where the sediment depositing in the channel is originating. Therefore, NAO has determined a more regional approach must be taken to answer this question. NAO, with the support of the Regional Sediment Management Program, has requested ERDC-CHL to conduct cohesive sediment process measurements to be utilized in the regional sediment transport models. This report describes field experiments conducted within the lower James River to define the distribution of sediment types, cohesive sediment erosion thresholds and rates, and settling velocities to support parameterization of the sediment bed within the estuary for numerical sediment transport modeling.

Objectives

The objectives of this work are to provide spatial distributions of sediment characteristics in the lower James River (Virginia) and determine parameterized descriptions of the cohesive sediment erosion and settling processes. Subsequent numerical modeling studies will apply these sediment descriptions and parameterizations to evaluate sediment management alternatives in the lower James River.

Approach

Sediment characteristics and process descriptions were developed from bed and suspended sediment samples collected over a 150 km[1] reach of the lower James River. Grain size characteristics were developed from surface grab samples and shallow cores collected up to 50 cm depth below the sediment surface. Erosion testing was conducted with Sedflume on the shallow cores to describe erosion thresholds and rates with depth in the cores. A suite of instrumentation including the Particle Imaging Camera System (PICS) was repeatedly cast at two locations to measure tidal variations in suspended sediment concentration, size, and settling velocity. These measurements were further analyzed to produce parameterized descriptions suitable for application in future numerical sediment transport modeling.

[1] For a full list of the spelled-out forms of the units of measure used in this document, please refer to *US Government Publishing Office Style Manual*, 31st ed. (Washington, DC: US Government Publishing Office 2016), 248-52, https://www.govinfo.gov/content/pkg/GPO-STYLEMANUAL-2016/pdf/GPO-STYLEMANUAL-2016.pdf.

2 Methods

This section describes the field experiments, sampling methods, experimental methods, and data analysis methods used in determining cohesive sediment erosion and settling velocity in the James River, Virginia. The study site is described first, followed by an overview of cohesive sediment transport processes, technical descriptions of the experimental devices, and a description of how these devices were deployed during field experiments to meet the study objectives.

Study site

The federal navigation channel in the James River extends from Richmond, VA, to the Chesapeake Bay, a distance of approximately 145 km (Figure 1). The channel is authorized to a depth of 10.6 m and 91.4 m wide from Hampton Roads to Richmond Deepwater Terminal, approximately 138 km in length. However, the channel is currently maintained to a maximum dredging depth of 7.6 m and 91.4 m wide. Presently, annual dredging volumes within the James River exceed 7.5×10^5 m^3 of material. The study area is tidally influenced, with mixed semi-diurnal tidal ranges on the order of 0.7 to 1 m.

Figure 1. James River study site.

Cohesive sediment transport processes

The sediments of interest within the James River are predominantly cohesive sediment. Non-cohesive sediment (sand and gravel) erosion and settling can be generally estimated as a function of grain size distribution and mineral density. Cohesive sediment transport processes are dominated by other factors such as consolidation, clay mineralogy, biological activity, and organic content. The effects of these parameters are customarily described by site-specific measurements of erosion and settling followed by empirical fitting of these data to defined relationships applied in numerical models. Cohesive sediments are generally a mixture of sand, silt, and clay sized particles.

Erosion

A general definition for cohesive sediment is the following: sediment for which the erosion rate is not well represented by standard sand transport methods. In these cases, cohesive forces are equivalent to or are greater than the gravitational forces that dominate sand transport. Cohesive sediment erosion characteristics are highly dependent upon factors such as particle size distribution, particle coatings, fine sediment mineralogy, organic content, bulk density, gas content, pore-water chemistry, and biological activity. Erosion rate and critical shear stress for erosion can vary significantly with small changes in only one of these inter-dependent parameters. It has been well demonstrated that critical stress and erosion rates for cohesive sediment can vary over several orders of magnitude for sediments with only slightly differing properties. Therefore, the influence of cohesion on sediment processes is significant. Qualitatively, it is understood which properties most significantly influence erosion. However, there are no quantitative methods available to determine erosion rate from cohesive sediment properties. Therefore, due to the sensitivity and wide range of influencing parameters, erosion characteristics of cohesive sediments are determined by site-specific analysis of erosion with erosion flumes.

Several flumes are available to parameterize site-specific cohesive sediment erosion algorithms. Most of these devices operate over a range of low shear stress (<2 Pa) and are consequently capable of measuring surface sediment erosion. Sedflume is an erosion device with capability to impose bed stresses in the range of 0.1 to 12 Pa and measures erosion rates from sediment cores taken from the field (for in situ or stratified bed

conditions) or prepared in the laboratory (for assessing disturbed sediments such as dredged material). Sedflume is designed to quantify erosion rates for surface and sub-surface sediments. These measurements permit description of the vertical variation of erosion rate within the bed. Note that even if sediments are well mixed, cohesive sediment bed erosion will change with depth due to the influence of consolidation (bed density) on erosion rate. Erosion rate can vary by several orders of magnitude between surficial sediments and sediment buried less than 30 cm below the surface. Sedflume was selected to quantify erosion rate and erosion rate variation with depth (density) for this study.

Settling velocity

Settling of cohesive sediments is also governed by processes that are difficult to estimate from fundamental sediment properties. Cohesive sediments are known to aggregate (or stick together) to form flocs, composed of fine-grained sediments and organic matter. Floc size is governed by the balance between aggregation and disaggregation processes. Aggregation is influenced by processes causing particles to collide and the efficiency with which these particles stick together. Particle collisions are influenced by turbulence, differential settling, and Brownian motion whereas aggregation efficiency is largely associated with surface characteristics of the particles (mineralogy, surface coatings, biological polymers, and water chemistry). Disaggregation is influenced by turbulent shear and inter-particle bonding strength of the floc.

Flocs formed in suspension have large porosities, and a large fraction of floc volume is occupied by water. After flocs have settled to the sediment bed, the weight of overlying sediments collapses the floc structure and expels pore water. This process, known as *consolidation*, results in increased bed density and increased inter-particle bond strength. If the consolidated bed is later exposed by erosion, a portion of the eroded sediment may not be completely disaggregated and instead is suspended as small fragments of the previously consolidated bed. These *bed aggregates* are distinctly different from the aggregates formed in the water column (flocs) as they are more tightly packed, have stronger inter-particle bonds, and have larger particle densities.

The understanding of how these various influences impact floc growth and settling velocity is incomplete. As is the case with cohesive sediment erosion, site-specific field experiments are required to determine cohesive

sediment settling velocities. This study employs a digital video settling column to determine cohesive sediment fall velocities.

Bed sampling

Sampling and erosion testing activities were conducted 6–18 November 2017. Sample collection was accomplished by a combination of surface sampling and shallow coring.

Surface sample collection. From 7–9 November 2017, sediment samples were collected from the surface of the sediment bed at 13 locations with the ERDC drag sampler. The sampler is a 15 cm diameter, 55 cm long stainless steel bucket equipped with a drag chain (Figure 2). The drag sampler is designed to collect a *surface grab* sample that is representative of the upper 5–7 cm of the sediment bed. The drag was lowered to the river bed by rope, secured to the vessel, and drug a distance of ~30–60 m. Upon retrieval to the vessel, overlying water was decanted from the drag sampler, and recovered sediment was transferred to a stainless steel basin. A subsample of each drag sample was then collected in a plastic Whirlpack™ bag for grain size analysis. Sampling locations and coordinates for each surface sample are provided in Figures 3–5 and Table 1.

Table 1. Bottom drag grab sample.

Sample ID	Latitude (° north)	Longitude (° west)	Collection Date
Grab 01	37.27158	77.0755	11/8/2017
Grab 02	37.30513	77.0035	11/8/2017
Grab 03	37.24802	76.9752	11/8/2017
Grab 04	37.21703	76.8551	11/9/2017
Grab 05	36.95887	76.4245	11/7/2017
Grab 06	37.3166	77.272	11/9/2017
Grab 07	37.30978	77.1859	11/9/2017
Grab 09	37.12414	76.6408	11/7/2017
Grab 10	37.37907	77.3652	11/9/2017
Grab 11	37.35511	77.2935	11/9/2017
Grab 12	37.42438	77.4034	11/9/2017
Grab 13	37.37816	77.315	11/9/2017
Grab 16	37.2591	76.9782	11/8/2017

Figure 2. Bottom drag sampler.

Figure 3. Map of sampling locations in the James River from Hog Island downstream to Hampton. Yellow dots indicate grab samples; red squares indicate cores.

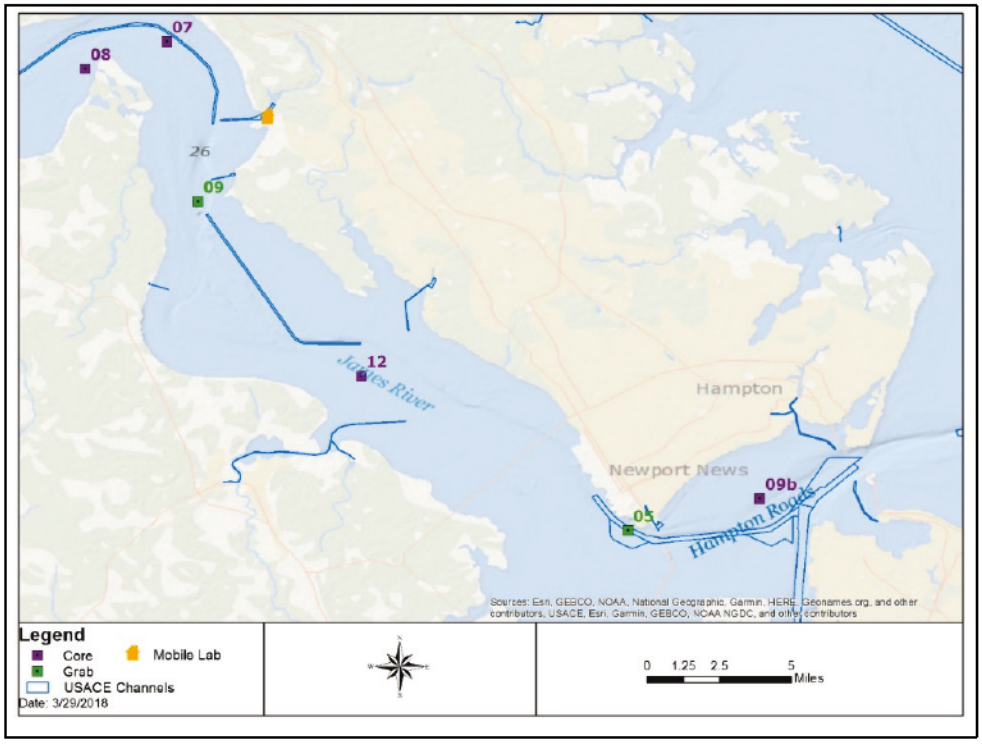

Figure 4. Map of sampling locations in the James River from Weyanoke downstream to Jamestown. Yellow dots indicate grab samples; red squares indicate cores.

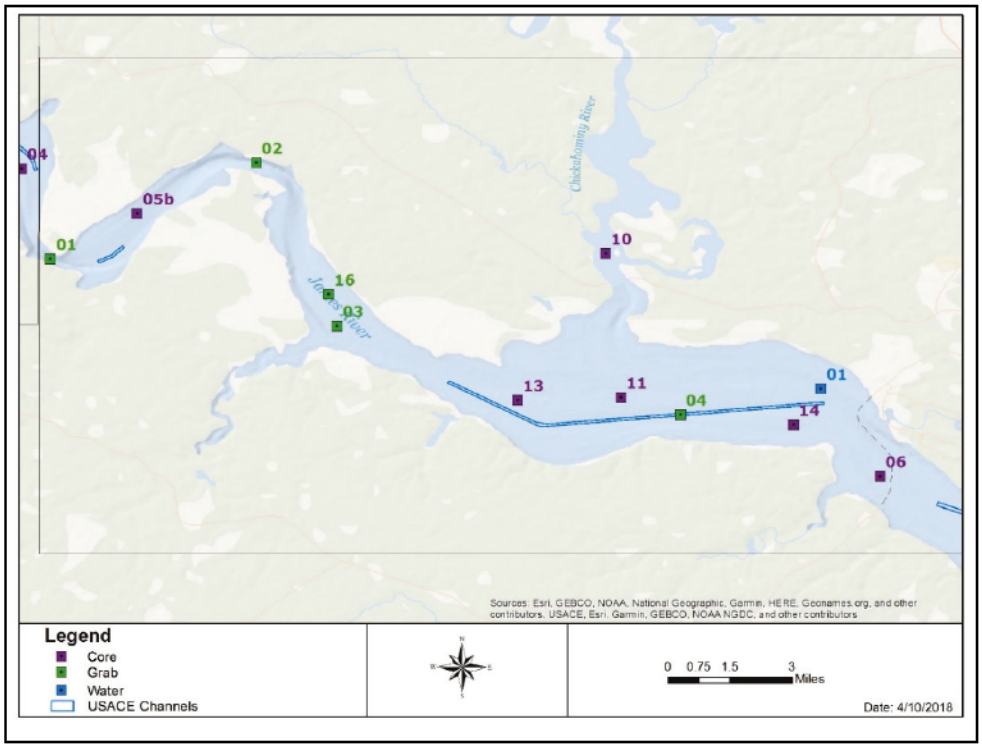

Figure 5. Map of sampling locations in the James River near Hopewell. Yellow dots indicate bottom drag grab samples; red squares indicate cores.

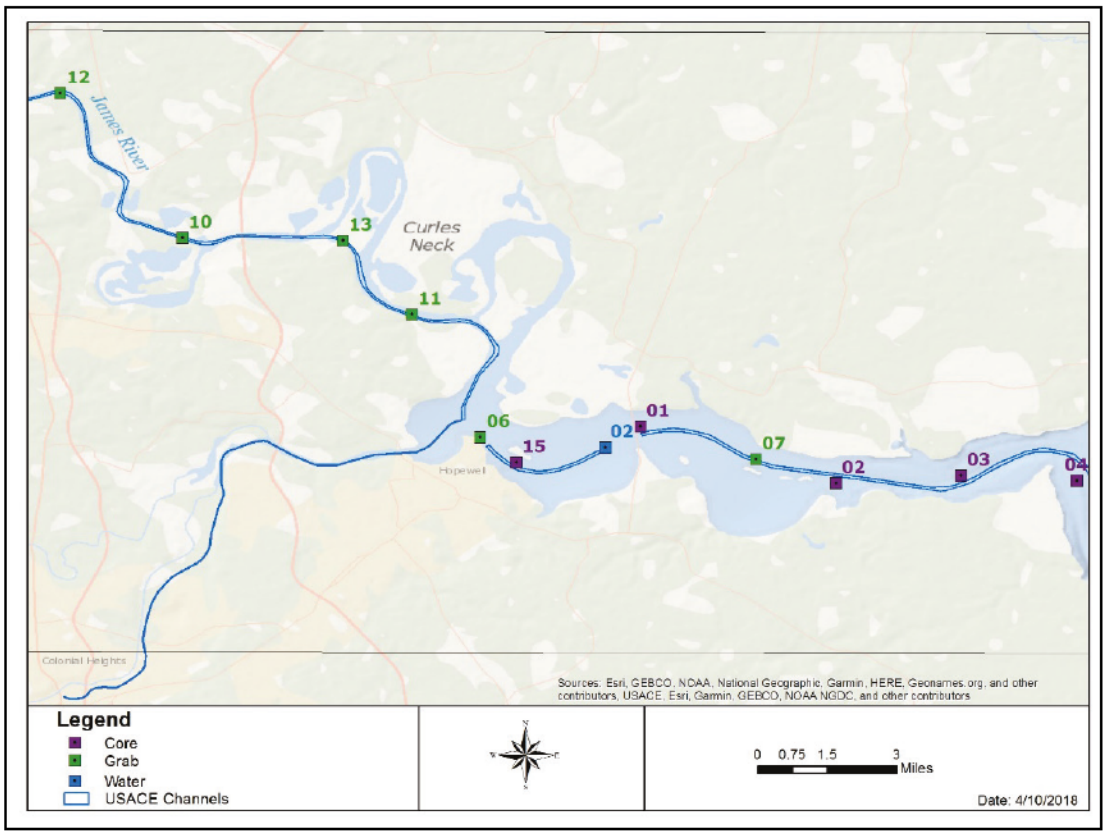

Core collection. On 6–9 November 2017, 10 cm diameter cores were collected from 15 locations within the James River (Figures 3–5) for the purpose of erosion testing. Original sampling coordinates placed Core 09 within a mooring area north of the navigation channel. Initial coring attempts at this location resulted in minimal penetration and sediment recovery. To obtain a core of sufficient length for erosion analysis, the sampling location was relocated outside the mooring area (approximately 850 m northwest of the original location) as indicated by position 09b in Figure 3 and Table 2. The initial core collected at site 09 was discarded and not analyzed in this study. Additionally, a replicate core was collected at station 5 (labeled 05b) due to a pinched o-ring being observed on the inserted plunger in the original core. The initial core was discarded and not analyzed in this study. Table 2 provides core logging information for each of the cores collected.

Table 2. Sediment core summary.

Core ID	Latitude (° north)	Longitude (° west)	Collection Date	Core Type	Core Length (cm)
Core 01	37.31995	77.222	11/9/2017	Box	27-31
Core 02	37.3023	77.1609	11/9/2017	Box	19.5
Core 03	37.3047	77.1218	11/9/2017	Box	13-14
Core 04	37.30306	77.0855	11/8/2017	Box	18
Core 05b	37.28746	77.0452	11/8/2017	Push	18-19
Core 06	37.19545	76.7852	11/7/2017	Push	20
Core 07	37.20454	76.6567	11/7/2017	Box	31-32
Core 08	37.19095	76.6978	11/7/2017	Push	24
Core 09	36.96971	76.3515	11/6/2017	Box	7-9
Core 09b	36.9748	76.3584	11/7/2017	Box	9.5
Core 10	37.27339	76.8812	11/8/2017	Box	16
Core 11	37.22315	76.8759	11/8/2017	Box	33-35
Core 12	37.03652	76.559	11/7/2017	Box	28-31
Core 13	37.22213	76.9121	11/8/2017	Box	37
Core 14	37.21366	76.8156	11/8/2017	Box	34-35
Core 15	37.30873	77.2608	11/9/2017	Box	15.5

Cores from the James River were collected by both push and box coring methods. The ERDC push corer was utilized in water depths ≤ 4.5 m and is composed of a polycarbonate core barrel, a 10 cm diameter polyvinyl chloride (PVC) sleeve, a 5 cm PVC check valve, and aluminum push poles (Figure 7A). The operator lowers the push corer to the sediment bed and pushes the corer into the bed while maintaining a vertical orientation. The check valve serves to create a seal above the core to prevent the captured sediment core from slipping out of the core tube. Once the core is retrieved to the vessel, a plunger with bentonite paste (for sealing and lubrication) is inserted into the bottom of the core and each end of the core is sealed with end caps (Figure 6B and 6C).

Figure 6. Push coring system.

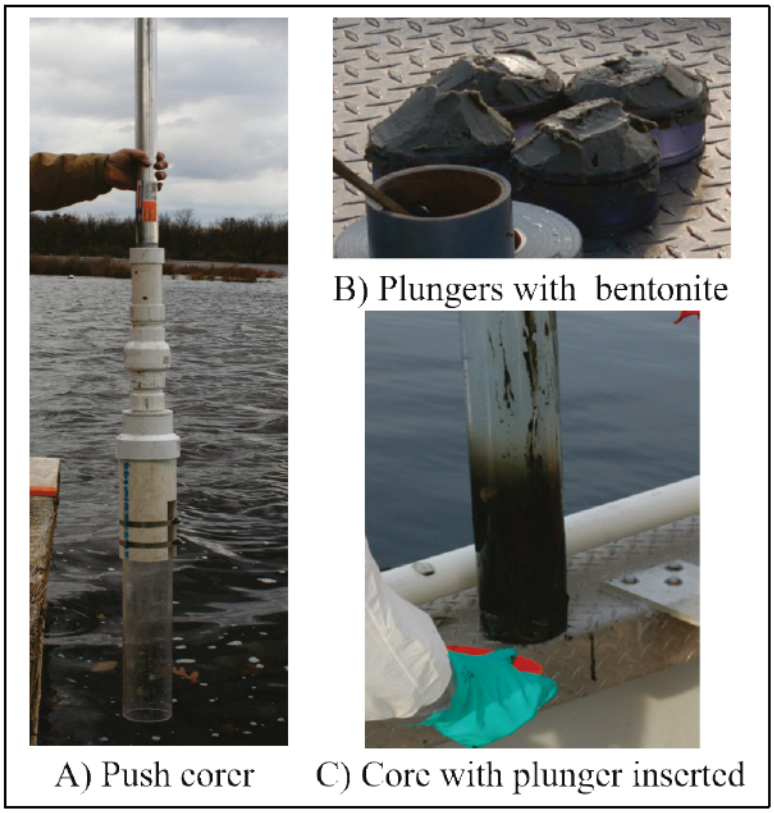

The ERDC box corer (Figure 7A) is constructed of stainless steel, has a maximum sampling depth of 55 cm and weighs approximately 136 kg. The box corer is deployed from the vessel with a hydraulically powered A-frame and winch. Upon reaching the bottom, the core penetrates the bed by its own weight and momentum. The scoop arm of the core closes during retrieval and captures sediment and water within the sample bucket. Once the box core is returned to the deck, the sampling bucket is removed from the frame and subsampled with polycarbonate core tubes. These subcores are gently pushed into the sediment by hand (Figure 7B). Caps are placed on the top of each tube to create a seal to prevent captured sediment from slipping from the bottom of the tube (Figure 7C). The subcores are then excavated from the sampling bucket with a hand covering the bottom of the core tube prior to removal. A plunger with bentonite paste (for sealing and lubrication) is then inserted into the bottom of the core.

Figure 7. Box coring system.

Core transport and storage. Cores collected were transported by vessel to the ERDC-CHL mobile sediment laboratory, which was staged at the port at Ft. Eustis (Figure 3). Erosion tests were conducted from November 8 to 18, 2017. While awaiting testing, the collected cores were stored in shaded barrels, filled with site water.

Sedflume

Sedflume is a field- or laboratory-deployable flume for quantifying cohesive sediment erosion. The USACE-developed Sedflume is a derivative of the flume developed by researchers at the University of California at Santa Barbara (McNeil et al. 1996). The flume includes an 80 cm long inlet section (Figure 2) with cross-sectional area of 2 × 10 cm for uniform, fully developed, smooth-turbulent flow. The inlet section is followed by a test

section with a 10 cm diameter open bottom. Coring tubes, flume test section, inlet section, and exit section are constructed of clear polycarbonate materials to permit observation of sediment-water interactions during erosion testing. The flume includes a port over the test section to provide access to the core surface for physical sampling. The flume accepts sediment cores up to 80 cm in length.

Erosion testing

Prior to erosion testing, descriptions of the core are recorded, including length, condition of the core surface, biological activity, and any visual evidence of layering. Cores are inserted into the testing section of Sedflume, and a screw jack is used to advance the plunger such that the core surface becomes flush with the bottom wall of the flume. Flow is directed over the sample by diverting flow from a 5.5 hp trash-pump, through a 5 cm inner diameter hose, into the flume. The flow through the flume produces shear stress on the surface of the core. (Numerical, experimental, and analytical analyses have been performed to relate flowrate to bottom shear stress.) Erosion of the surface sediment is initiated as the shear stress is increased beyond the critical stress for erosion, τ_c. As sediment erodes from the core surface, the operator advances the screw jack to maintain the sediment surface flush with the bottom wall of the erosion flume. Figure 8 includes a photograph of the flume, a close-up photograph of the test section, and a table of flow rate/shear stress relationships.

Erosion velocity was determined from the displacement of the core surface and elapsed time of the erosion interval. Generally, erosion tests were performed by repeating a sequence of increasing shear stresses. Approximately 1–5 mm of sediment is eroded at each erosion interval at a specified, constant shear stress, and thus the duration of each test was dependent on the rate of erosion. Generally, these erosion tests were between 30 and 600 sec in duration. A diagram depicting this erosion test process along with an example erosion sequence is shown in Figure 9.

Figure 8. Sedflume erosion flume (lower right). Core inserted into test section (upper left). Core surface flush with bottom of flow channel (upper right). Table of shear stress associated with channel flow rates (lower left).

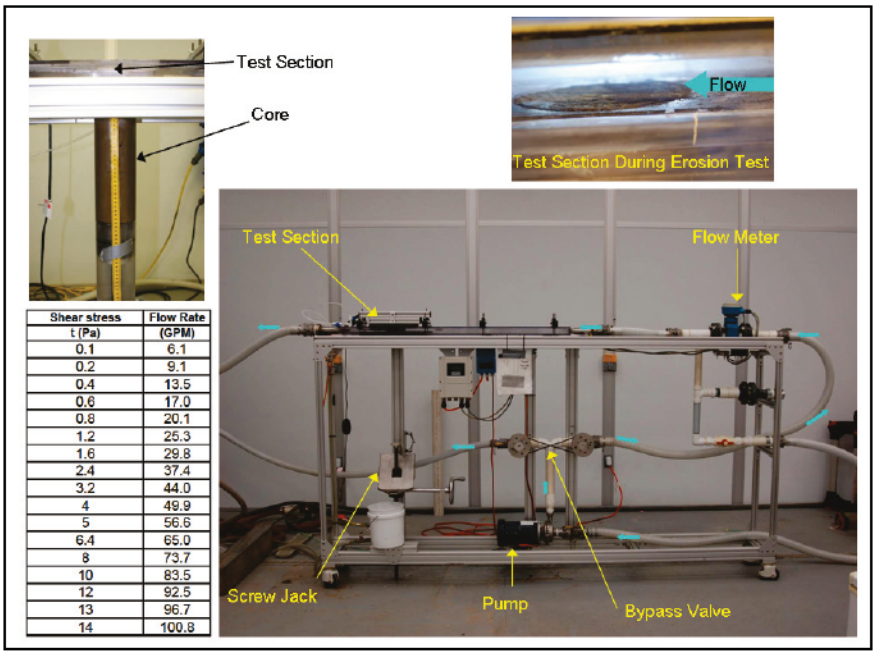

Shear stress τ (Pa)	Flow Rate (GPM)
0.1	6.1
0.2	9.1
0.4	13.5
0.6	17.0
0.8	20.1
1.2	25.3
1.6	29.8
2.4	37.4
3.2	44.0
4	49.9
5	56.6
6.4	65.0
8	73.7
10	83.5
12	92.5
13	96.7
14	100.8

Figure 9. Diagram of sediment core erosion process. The brown arrow indicates direction of motion of the sediment into the flume as the screw jack is advanced. The blue arrow indicates flow direction of water. Operational erosion rate limits (shown in white lettering) set the bounds of shear stress intervals for the erosion sequence. An example erosion sequence is provided in the table to the right of the sediment core. Similar erosion sequences are repeated multiple times throughout the core with physical samples being collected every 3–5 cm.

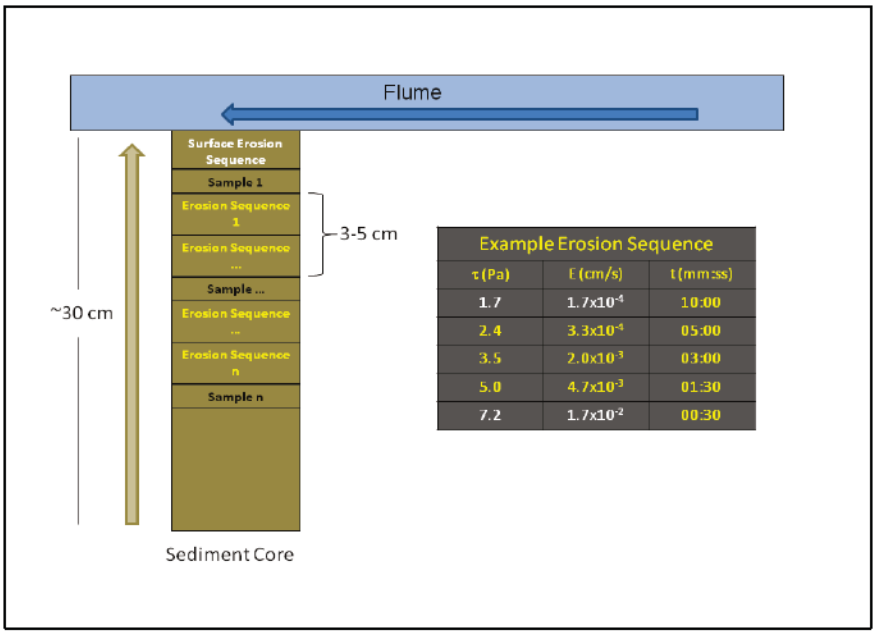

Example Erosion Sequence		
τ (Pa)	E (cm/s)	t (mm:ss)
1.7	1.7×10^{-4}	10:00
2.4	3.3×10^{-4}	05:00
3.5	2.0×10^{-3}	03:00
5.0	4.7×10^{-3}	01:30
7.2	1.7×10^{-2}	00:30

Sediment bulk properties

Physical samples for bulk sediment property measurements were taken at approximately 3–5 cm intervals during erosion tests, generally at the end of a shear stress cycle. Physical samples were collected by draining the flume channel, opening the port over the test section, and extracting a sample from the sediment bed. These samples were then measured for bulk density and grain-size distribution. These properties strongly influence erosion; therefore, documenting any variation with depth is important in interpreting the erosion data.

Bulk density measurements. Bulk sediment density of physical samples is determined by the sediment water content. Physical samples are extracted from the saturated core surface and placed in a pre-weighed aluminum tray. Sample weight is recorded immediately after collection and again after a minimum of 12 hr in a 50°C (122°F) drying oven. Wet weight of the sample was calculated by subtracting tare weight from the weight of the sample. The dry weight of the sample was calculated as the tare weight subtracted from the weight after drying. The water content w is then given:

$$w = \left(\frac{m_w - m_d}{m_d} \right) \tag{1}$$

where m_w and m_d are the wet and dry weights, respectively. A volume of saturated sediment, V, consists of both solid particles and water and can be written as

$$V = V_s + V_w \tag{2}$$

where V_s is the volume of solid particles and V_w is the volume of water. If the sediment particles and water have densities ρ_s and ρ_w, respectively, the water content of the sediment can be expressed as

$$w = \frac{\rho_w V_w}{\rho_s V_s} \tag{3}$$

The mass of this sediment volume is

$$\rho_b V_T = \rho_s V_s + \rho_w V_w \tag{4}$$

where ρ_b is the bulk density of the sediment sample.

Equations 1–4 are used to derive an explicit expression for the bulk density of the sediment sample, ρ_b, as a function of the water content, w, and the densities of the sediment particles and water. This equation is

$$\rho_b = \rho_s + \frac{w\rho_s\left(\rho_w - \rho_s\right)}{\rho_w + w\rho_s} \tag{5}$$

For the purpose of these calculations, ρ_s = 2.65 g·cm^{-3} and ρ_w is calculated for measured pore water at room temperature.

Particle-size distribution. Samples collected during erosion experiments were transported to the Sediment Transport Processes Lab at the ERDC for grain size analysis. A Malvern Mastersizer 2000 laser particle-sizer was used to measure the particle-size distributions in sub-samples collected from the cores. The Malvern measures particle size over the range 0.02 to 2000 µm. Sediments were homogenized, sub-sampled (1–2 g), and deflocculated overnight in a solution of sodium metaphosphate (40 g/L). To remove large organic debris, samples were passed through a #18 mesh (1000 µm) sieve into the instrument's reservoir and sonicated for 60 sec prior to analysis. The sample was then pumped and recirculated through the optical module. The optical module includes a spatial filter assembly containing a laser diode and laser beam collimator. The diffraction detector assembly contains a custom photodetector array that is used for the measurement of light scattering by the suspended particles. The distribution of grain sizes and median grain sizes is derived from this light scattering measurement. Organic material was not oxidized or combusted prior to grain size analysis.

One sample (Grab 13) was composed almost entirely of pebble-sized sediment. This sample was tested with a nine-sieve stack at one-ϕ size intervals between 63 to 32000 µm, following the methods described in ASTM D6913.

Erosion analysis

The goal of erosion data analysis is to determine appropriate parameterization of erosion processes so that they may be incorporated into numerical modeling studies. Analysis of cohesive sediment erosion data obtained from undisturbed field cores is typically complex. Cohesive sediment erosion can be sensitive to slight changes in bed density, deposit

mineralogy, gas content, organic content, biological activity, and a host of other factors. In many cases, these factors change significantly and repeatedly at relatively small vertical scales, a result of depositional bed sequences. Consequently, measured cohesive sediment erosion rates from field cores are much more variable than those measured in the laboratory setting with samples prepared of homogeneous composition. To counter the large variance in measured erosion rates, field erosion tests are conducted in a manner to produce a large sample from which to derive statistically representative relationships to various numerical erosion algorithms. To ensure high quality in the data analysis, data and associated experimental notes are evaluated to identify outliers in the dataset. Outliers are rejected based on comparisons between adjacent data points and experimental log notes.

Erosion data are evaluated for consistency in shear stress-erosion response with depth. Data that exhibit similar shear-erosion responses are grouped together, with additional consideration given to the physical sample data and notes recorded during the testing. Log-linear regressions of erosion rate to applied shear stress are performed to determine coefficients for one or more common cohesive sediment erosion expressions. For the present study, the data were fit to the so-called Sedflume erosion expression, $E=A\tau^N$ where E is erosion rate in cm/s, τ is the applied shear stress in Pa, and A and N are parameters determined from the log-linear regression to the data. Critical shear stress, τ_c, is determined from the regression parameters such that τ_c is the shear stress that corresponds to an erosion rate, E_c of 10^{-4} cm/s (or 3.6 mm/hr). Alternate critical shear stress values can be determined from the fit parameters to determine a minimum erosion rate considered to be relevant to the subject situation. The expression for critical stress is $\tau_c=(E_c/A)^{1/N}$, where E_c is the critical erosion rate. To avoid extrapolation errors, caution should be exercised in determining alternate critical shear stresses such that the critical stress, E_c, is not smaller than a factor of 10 less than the minimum erosion rate in the dataset.

Water column sampling

Physical sampling and measurements of suspended sediment size and settling velocity were conducted on 10 November 2017 at Station PICS01 (37.2262N, 76.8061W) and 11 November 2017 at Station PICS02 (37.3135N, 77.2330W) shown in Figures 4 and 5, respectively. At each station, vertical casts were performed with the instrumentation frame to

measure water temperature and salinity, suspended sediment size and settling velocity, and to collect physical suspended sediment samples. Casts were performed for approximately 7 hr each day at 30 min intervals with nominally 1 m vertical resolution. For each cast, water temperature, salinity, and suspended sediment size and settling velocity were measured. (Additional details of the instrumentation are provided below.)

Physical samples were collected less frequently, at approximately 2 hr intervals and 2 m vertical resolution. Physical samples were collected by pump sampling with a 0.19 L/s pump through a 25 m long, 9.5 mm diameter tube. For each physical sampling position, two 1 L samples were collected: one for grain size analysis and one for suspended sediment concentration (SSC).

Suspended sample analysis

Particle size and concentration analysis was performed at the ERDC-CHL Sediment Transport Laboratory in Vicksburg, MS. After samples were transported to the laboratory, samples for grain size analysis were allowed to settle for at least 5 days followed by a decanting of the supernatant water. The concentrated sample of suspended solids was then treated and analyzed with the Malvern Mastersizer 2000 by the same process described above for bed sediment samples.

Suspended sediment samples designated for concentration analysis were tested according to ASTM D3977, Method B – filtration. Samples were filtered by vacuum filtration through 90 mm diameter glass fiber filters with retention rating of 0.7 µm. The filtered samples were rinsed with laboratory-grade clean water at the end of filtration to clear the filter of dissolved solids.

The Particle Imaging Camera System (PICS)

The PICS is an ERDC-developed system for in situ measurements of cohesive sediment settling velocities. PICS collects digital video of particle settling within a small settling column and can be deployed in the water column or in a laboratory setting. Sample collection, optical and lighting design, and image acquisition were designed to produce high-quality, in situ image sequences. PICS consists of a 1 m long, 5 cm inner diameter settling column with a mega-pixel digital video camera and strobed light-emitting diode (LED) lighting (Figure 10). The settling column is equipped with two

pneumatically controlled ball valves at the column ends, which permit sample capture, and a third pneumatic actuator for rotating the column from horizontal to vertical orientation for image acquisition.

Figure 10. (A) Instrumentation frame indicating positioning of PICS with optional deployment of additional instrumentation such as Laser In-Situ Scattering and Transmissometry (LISST) and Conductivity-Temperature-Depth (CTD); (B) Schematic of settling column indicating horizontal and vertical orientations; (C) Schematic of camera, settling column cross section, and LED lighting.

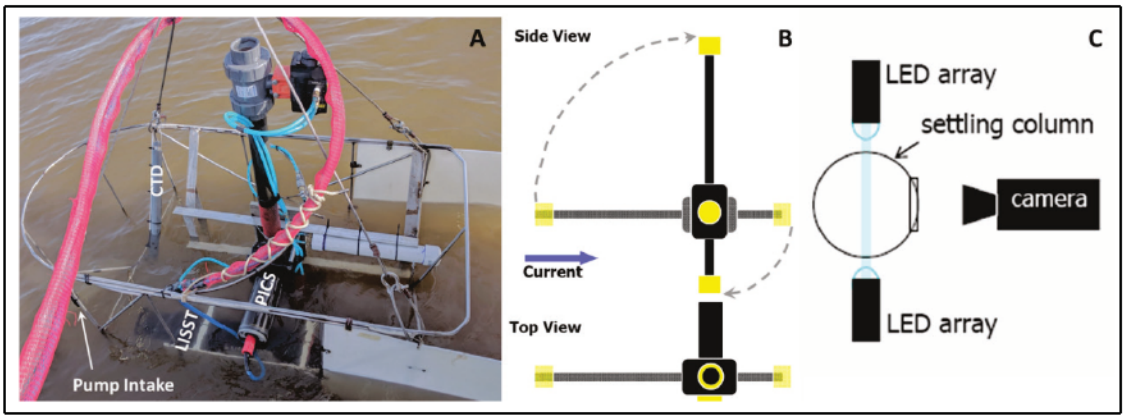

Additional instrumentation was deployed with PICS, including LISST (LISST-100X, type C; 2.5–500 µm range), CTD, and pump sampler. Additional details of PICS, including system configuration and measurement uncertainty, are provided by Smith and Friedrichs (2011).

Image analysis

Image analysis is accomplished with a combination of Particle Tracking Velocimetry (PTV) and Particle Image Velocimetry (PIV) methods. PTV is applied to particles larger than 30 µm and results in estimates of large particle motion relative to the focal plane. PIV is applied to particles smaller than 20 µm, and the motion of these small particles is treated as a surrogate for fluid motions within the column relative to the focal plane. Vector subtraction of the fluid and particle velocities results in individual particle settling velocity (relative to the suspending fluid). Additional details of the image processing and analysis methods are provided in Smith and Friedrichs (2015).

Particle density and aggregation state

Image analysis results in simultaneous measurement of particle size and settling velocity. Using these two measured parameters permits estimation of individual particle densities. This is accomplished by solving the settling

balance for spherical particles with the Schiller-Naumann (1933) (Graf 1971) drag approximation:

$$w_s = \frac{gd^2}{18\mu} \frac{\left(\rho_p - \rho_w\right)}{\left(1 + 0.15 Re_p^{0.687}\right)} \tag{6}$$

for particle density:

$$\rho_p = \rho_w + \frac{18\mu w_s}{gd^2}\left(1 + 0.15 Re_p^{0.687}\right) \tag{7}$$

where w_s is particle settling velocity, d is particle diameter, μ is fluid dynamic viscosity, ρ_p is particle density, ρ_w is fluid density, Re_p is particle Reynolds Number ($Re_p = w_s d/\nu$), and ν is fluid kinematic viscosity. The Schiller-Naumann drag approximation extends Stokes Law (which is limited to $Re_p << 1$) to $Re_p < 800$.

The estimated individual particle densities are used to classify particles by their aggregation state. Aggregation states include primary particles (individual mineral grains), bed aggregates (aggregations with density approximating that of the sediment bed), and flocs (lower-density aggregations formed in the water column). Flocs are associated with density between 1010 to 1200 kg m^{-3} (excess density ($\rho_p - \rho_w$): 0–180 kg m^{-3}), bed aggregates: 1200–1800 kg m^{-3} (excess density: 180–780 kg m^{-3}), primary particles: 1800–3000 kg m^{-3} (excess density: 780–2000 kg m^{-3}). Density range for flocs was determined from published data (Krone 1963; Krank et al. 1993; van Leussen 1994). The density range for bed aggregates extends from the upper limit of flocs to 1800 kg m^{-3} (an upper limit based on saturated bulk density of densely consolidated cohesive and mixed sediment beds and supported by published data: Torfs et al. [2001]; Winterwerp and van Kesteren [2004]). Density range for primary particles was set from the upper limit of bed aggregates to the maximum expected mineral density.

3 Results and Discussion

Cohesive sediment transport process data collected during the field study were analyzed to determine parameterizations for cohesive sediment erosion. The results of the data analysis and parameterization are presented in the following sections. This section will describe general observations and interesting contrasts in the data. The reader is referred to technical appendices for full presentation of the analyzed dataset.

Cohesive sediment erosion

Erosion tests revealed all cores to be notably layered, as seen in Core 12 (Figure 11). Consequently, erosion datasets from the core stations were segmented by bed layers as seen in Figures 11 and 12. The upper 1 cm was the most erodible, and the sediment exhibited increased erosion resistance with depth. Between 1 to 3 cm exists a transitional layer in which the erosion rates at a given shear stress decrease by approximately a factor of 10. The remaining core between 3 to 18 cm becomes progressively more difficult to erode with depth, as is often seen for a consolidating bed. There are no evident *storm* layers (characterized by sharp changes in erosion trends or sediment composition) in this lower layer. The erosion relationships for Core 12 were categorized into four erosion relationships. The first two erosion relationships are for the layers 0–1 cm and 1–3 cm as described above. The zone between 3 to 18 cm was split into two erosion layers to capture the observed trend of increased erosion resistance with depth.

Figure 11. Erosion rate at a given applied stress versus depth down core (left). Class fractions and bulk density of physical samples (right) for Core 12.

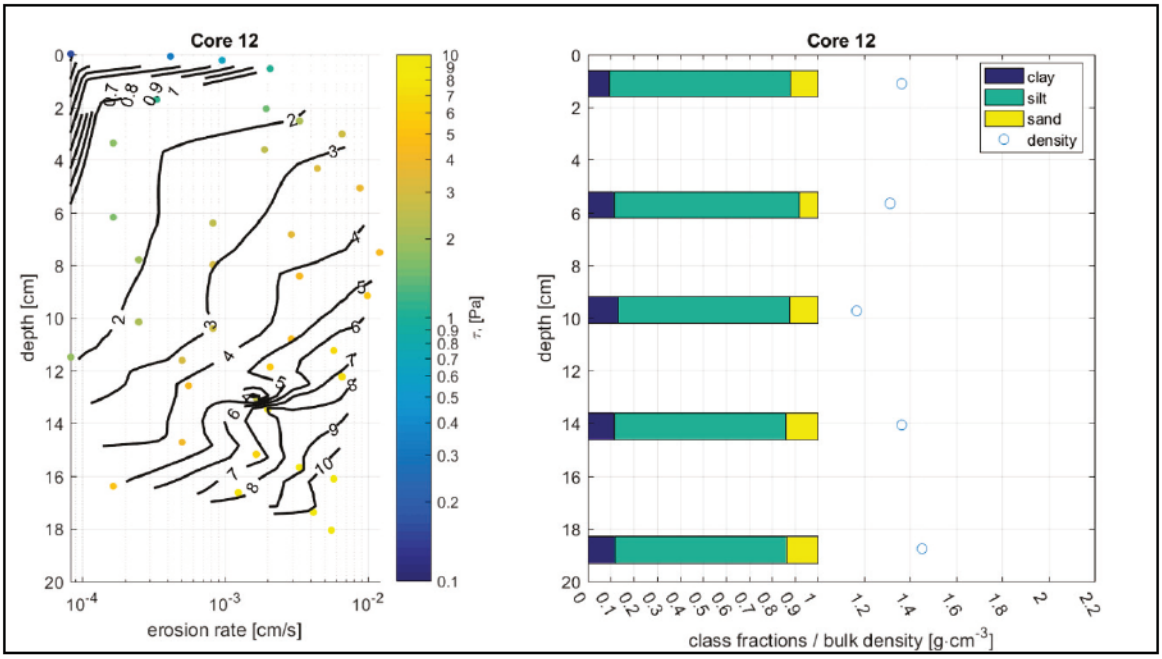

Figure 12. Erosion rate versus applied stress and resulting power law fit (s) for Core 12. Filled symbols indicate data points included in the regressions; hollow symbols indicate data points not belonging to any regression; symbol color corresponds to depth down core. Solid lines indicate the best-fit of the data to $E=A\tau^N$, and dashed lines indicate the 95% confidence interval of the regression.

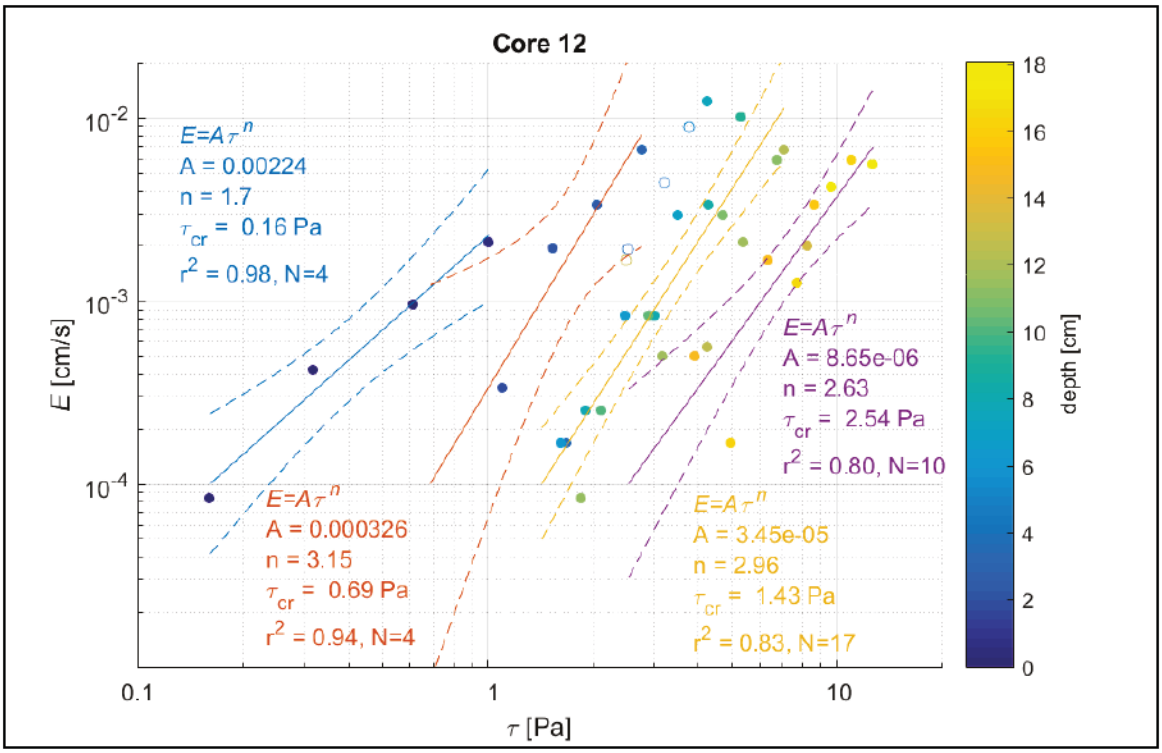

The remaining cores of the erosion testing were analyzed in a similar fashion. Layer segmentation during analysis was based on a combination of visual core descriptions logged in the field, physical sampling, erosion test notes, and erosion rate data. Data for each core including photographs, visual descriptions, results of physical sample analysis, and figures identifying bed layers and corresponding erosion parameters are provided in Appendix A. The resulting parameters for each layer in all cores are provided in Table 3.

Table 3. Summary of erosion parameters.

ID	Depth1 [cm]	Depth2 [cm]	τc (best) [Pa]	τc95 (lower) [Pa]	τc95 (upper) [Pa]	A (best)	A95 (lower)	A95 (upper)	n	r2	p-val
Core 1	1.3	10.8	2.80	1.47	5.35	2.09E-05	7.84E-06	5.59E-05	1.52	0.84	2.63E-05
Core 2	0.0	0.8	0.20	0.16	0.24	6.74E-03	3.76E-03	1.21E-02	2.58	0.99	3.65E-03
Core 2	4.9	12.2	2.84	1.85	4.36	3.56E-06	9.00E-07	1.41E-05	3.20	0.87	5.17E-08
Core3	0.2	0.4	0.61	0.16	2.27	3.86E-04	1.08E-05	1.38E-02	2.72	0.95	1.48E-01
Core3	1.6	2.4	0.36	0.23	0.57	3.09E-03	6.56E-04	1.45E-02	3.39	0.99	4.87E-02
Core3	2.8	3.6	0.83	0.31	2.18	1.51E-04	1.88E-05	1.21E-03	2.15	0.99	4.85E-02
Core3	6.0	7.0	4.44	0.94	20.94	6.67E-09	2.98E-13	1.50E-04	6.45	1.00	4.08E-02
Core 4	0.0	0.4	0.16	0.12	0.22	1.31E-03	8.40E-04	2.06E-03	1.40	0.99	3.49E-03
Core 4	0.7	2.5	0.57	0.47	0.69	5.12E-04	2.98E-04	8.78E-04	2.91	0.97	2.35E-03
Core 4	2.7	13.6	0.96	0.79	1.18	1.11E-04	6.37E-05	1.92E-04	2.70	0.84	5.86E-10
Core 5b	0.0	0.9	0.70	0.57	0.88	2.63E-04	1.44E-04	4.80E-04	2.76	0.99	5.30E-03
Core 5b	1.8	10.3	1.43	0.92	2.22	3.93E-05	1.23E-05	1.26E-04	2.63	0.78	1.22E-05
Core 6	0.1	0.6	0.43	0.13	1.45	7.81E-04	4.00E-05	1.53E-02	2.47	0.96	1.21E-01
Core 6	1.7	8.9	2.61	1.12	6.05	2.52E-06	9.91E-08	6.42E-05	3.84	0.58	3.78E-03
Core 7	0.0	1.3	0.24	0.14	0.41	2.56E-03	7.75E-04	8.46E-03	2.27	0.88	1.85E-02
Core 7	2.0	4.3	0.71	0.23	2.18	2.09E-04	1.94E-05	2.24E-03	2.11	0.41	8.49E-02
Core 7	6.3	17.0	3.19	2.11	4.84	2.32E-06	6.04E-07	8.95E-06	3.24	0.77	4.88E-10
Core 8	1.2	2.9	0.20	0.12	0.32	4.18E-03	1.40E-03	1.25E-02	2.28	0.85	8.98E-03
Core 8	4.4	14.6	0.51	0.41	0.62	7.44E-04	4.11E-04	1.35E-03	2.94	0.73	8.15E-04
Core 9B	1.5	7.7	0.63	0.57	0.70	7.58E-04	4.93E-04	1.16E-03	4.40	0.92	1.13E-05
Core 10	0.0	0.4	0.27	0.14	0.50	1.58E-03	4.27E-04	5.85E-03	2.08	0.96	2.23E-02
Core 10	1.5	9.4	0.37	0.34	0.40	8.66E-03	5.95E-03	1.26E-02	4.52	0.93	6.82E-09
Core 11	0.0	1.2	0.17	0.15	0.19	3.27E-03	2.56E-03	4.17E-03	1.94	1.00	1.34E-03
Core 11	2.5	3.5	0.56	0.42	0.74	6.19E-04	2.59E-04	1.48E-03	3.10	0.96	1.83E-02

ID	Depth1 [cm]	Depth2 [cm]	τc (best) [Pa]	τc95 (lower) [Pa]	τc95 (upper) [Pa]	A (best)	A95 (lower)	A95 (upper)	n	r2	p-val
Core 11	4.0	7.4	0.95	0.87	1.03	1.20E-04	8.97E-05	1.60E-04	3.41	1.00	5.39E-04
Core 11	3.8	13.8	1.42	1.26	1.61	3.01E-05	1.99E-05	4.55E-05	3.40	0.98	6.87E-11
Core 12	0.0	0.6	0.16	0.10	0.26	2.24E-03	9.78E-04	5.11E-03	1.70	0.98	1.02E-02
Core 12	1.7	3.0	0.69	0.41	1.16	3.26E-04	6.27E-05	1.70E-03	3.15	0.94	3.22E-02
Core 12	3.4	12.2	1.43	1.04	1.97	3.45E-05	1.34E-05	8.88E-05	2.96	0.83	3.98E-07
Core 12	12.6	18.1	2.54	1.12	5.75	8.65E-06	1.01E-06	7.40E-05	2.63	0.80	4.63E-04
Core 13	0.0	0.4	0.17	0.08	0.38	7.10E-03	1.04E-03	4.86E-02	2.40	1.00	3.66E-02
Core 13	3.6	10.2	1.07	0.84	1.38	7.91E-05	3.48E-05	1.80E-04	3.26	0.86	4.35E-06
Core 13	10.8	17.8	1.55	1.00	2.41	2.43E-05	5.84E-06	1.01E-04	3.22	0.79	1.99E-05
Core 14	0.0	2.8	0.30	0.24	0.38	1.97E-03	1.11E-03	3.50E-03	2.49	0.85	1.05E-03
Core 14	3.1	10.7	0.74	0.61	0.89	2.59E-04	1.43E-04	4.67E-04	3.13	0.81	5.24E-06
Core 14	12.0	18.4	1.58	0.73	3.42	3.50E-05	5.85E-06	2.09E-04	2.31	0.66	7.09E-04
Core15	0.0	0.6	0.15	0.00	40.16	1.46E-02	6.41E-09	3.33E+04	2.61	0.87	2.31E-01
Core15	1.6	9.2	0.29	0.27	0.31	5.61E-03	4.55E-03	6.93E-03	3.25	0.97	1.03E-11

A primary challenge in describing the sediment bed is describing the complex composition and erosion behavior of the sediment bed of an estuary with a limited number (in this case 15) samples. The sediment composition, bed density, and hydrodynamic setting were evaluated for consistencies in the data. Grouping of samples with similar erosion characteristics was performed to simplify the assignment of erosion characteristics to the sediment bed in the numerical model. As part of this exercise, the geographical distribution of surface sediments was evaluated (Figure 13). In general, the upper reaches of the river were sandier than the lower reaches, but sandy and muddy samples were found in each geographic region and hydrographic setting (navigation channel, shoal, flat). The muddy samples were found to have some consistency in composition. These samples were silt dominated with lesser quantities of sand (7%–15%) and clay (7%–11%).

Figure 13. Surface sediment distribution of samples collected from James River grab and core samples. Colored wedges indicate the relative composition of sediment size classes by the Wentworth system: clay (1–4 µm), silt (4–63 µm), sand (63–2000 µm), pebble (2000–64000 µm) (figure is continued to next page).

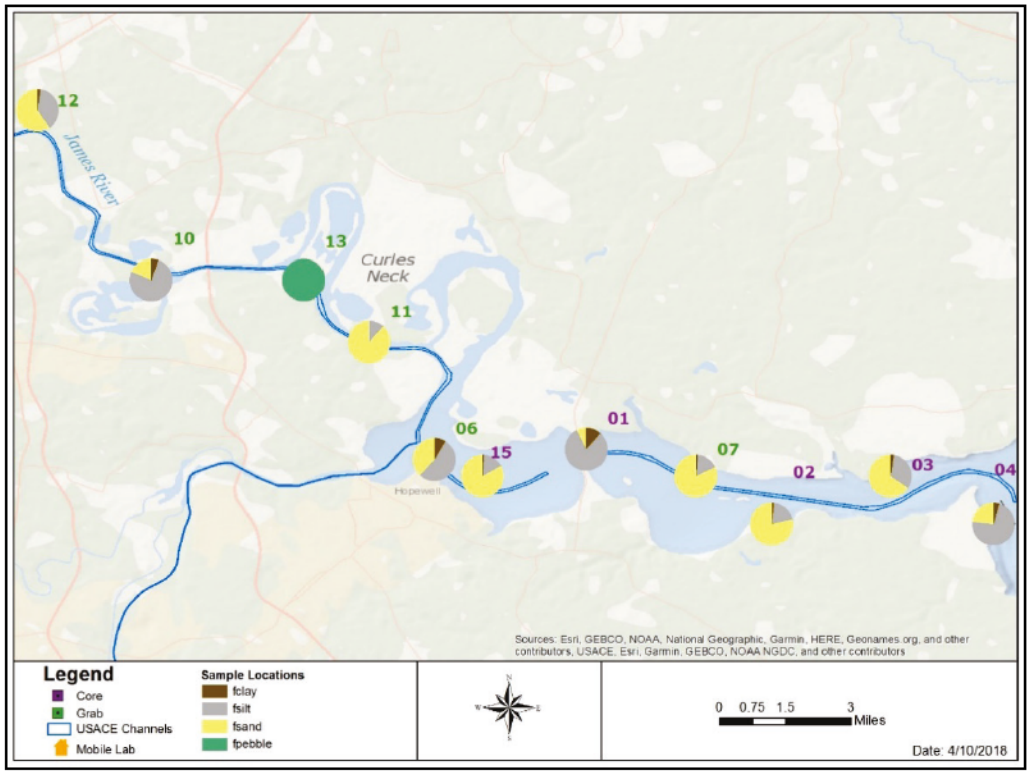

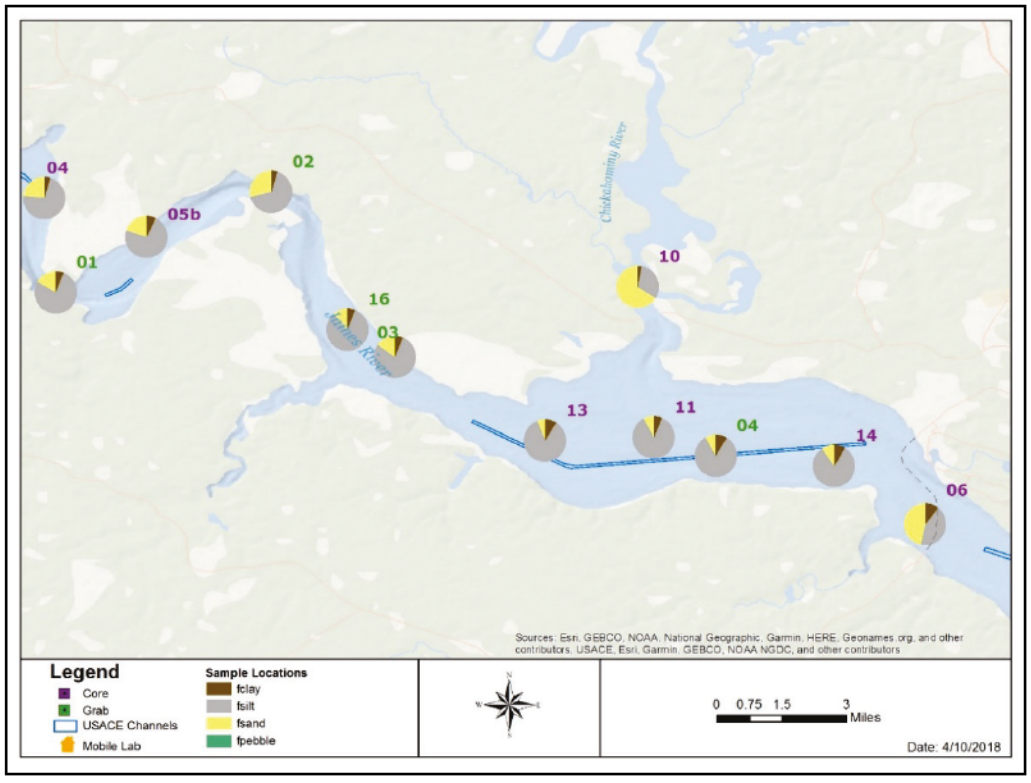

Figure 13. Continued.

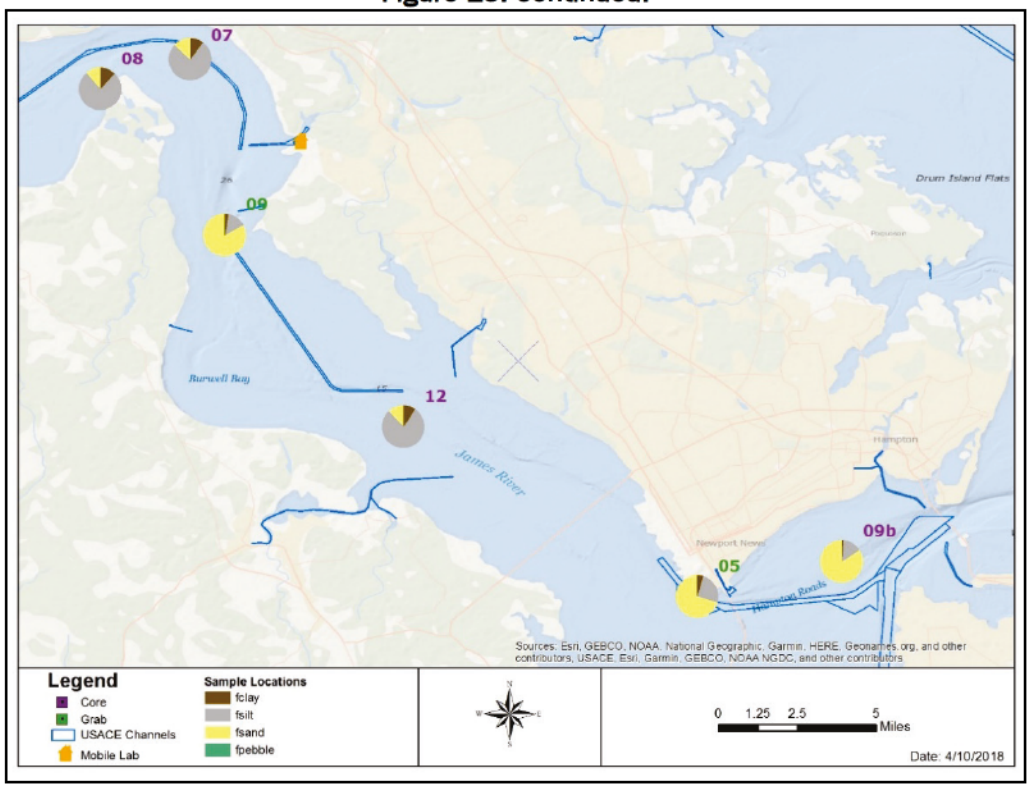

Upon examining the erosion characteristics of sediments by composition, some similarities emerged. Based on trends in the sediment composition and erosion behavior of the sampled sediments, cores or layers within cores were grouped into one of three sediment types: sandy, normally consolidated mud, over-consolidated mud. The rationale for these selections and the descriptions of these groups are provided below.

Sediment layers with sand fractions equal or greater than 0.5 were observed in Cores 2, 3, 6, 9, 10, and 15. The dependence of erosion versus shear stress for these sediments is provided in Figure 14. The modal sand sizes of these sandy layers ranged from 150 to 300 μm, which have an estimated critical shear stress of 0.15–0.20 Pa according to the Shields relationship for non-cohesive sediments. The critical shear stresses estimated from the Sedflume data ranged from 0.15 to 0.61 Pa, one to four times larger than the estimated non-cohesive critical shear stress. This suggests that there is a weak but measurable influence of the fine sediment content on these sandy sediments.

Figure 14. Sediment erosion versus depth for sandy layers of cores. Line and text color indicate individual layers.

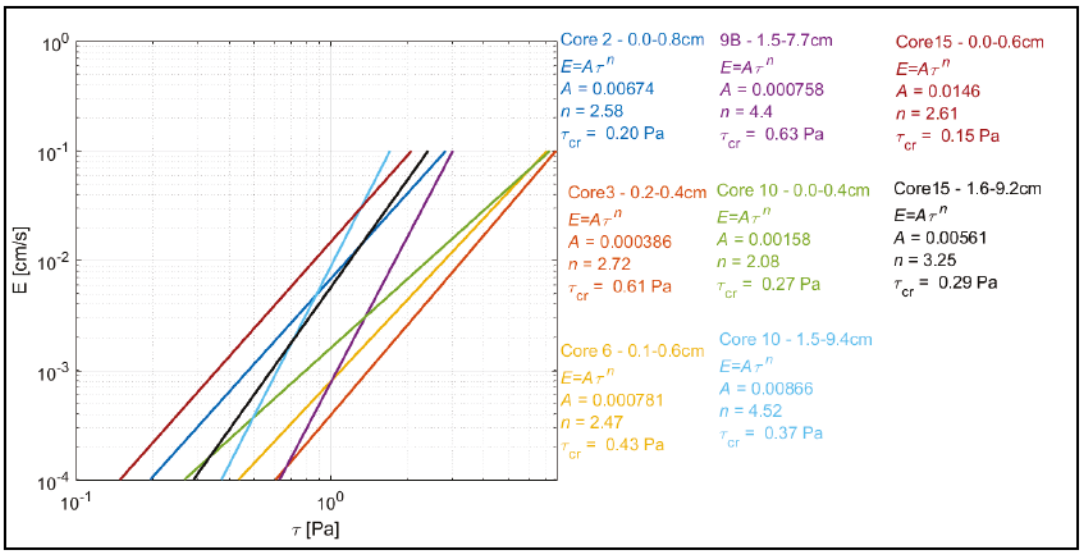

Normally consolidated mud is characterized increasing bulk density and erosion resistance with depth due to the effects of self-weight consolidation. Deeper in the sediment bed, the consolidation process slows due to the combined effect of increasing load bearing capacity of the sediment and the deceasing hydraulic conductivity of the denser sediment. The net effect is that both bed density and erosion resistance gradients decrease with depth into the sediment bed. As a normally consolidated sediment bed erodes, higher bed density and erosion resistance are expressed at the sediment-water interface. This is an effect of the consolidation history of the bed, which for the cores collected in this study is unknown. The situation for which sediment exists at a higher density than can be explained by self-weight consolidation is referred to as over-consolidated sediment. The present study has not undertaken sediment consolidation testing. The labeling of sediments in this chapter is based on relative comparisons of bed density and erosion resistance with depth for muddy sediments with similar sediment composition.

Normally consolidated muds were evident in Cores 4, 7, and 11–14. The erosion relationships to shear stress for these sediment positions and layers are provided in Figure 15. Although every core is not identical in the depths and thicknesses of layers and progression of erosion characteristics, general trends do hold. The first layer is consistently easier to erode, ranging in critical shear stress from 0.16 to 0.30 Pa. Thicknesses are generally 0.5 to 1.0 cm with a maximum of 2.8 cm. The second layer (Figure 15A) is more erosion resistant, ranging in critical shear stress from

0.6 to 1.0 Pa and depths of generally 2–10 cm (with considerable variation). The third and fourth layers (Figure 15B) continue the trends with increasing density and erosion resistance with depth. The layers in the normally consolidated group become generally thicker with depth, consistent with the reduced density gradients with depth typically observed for self-weight consolidation.

Figure 15. Sediment erosion versus depth for normally consolidated cores. (A) Upper two layers; (B) Lower two layers. Line and text color indicate individual layers.

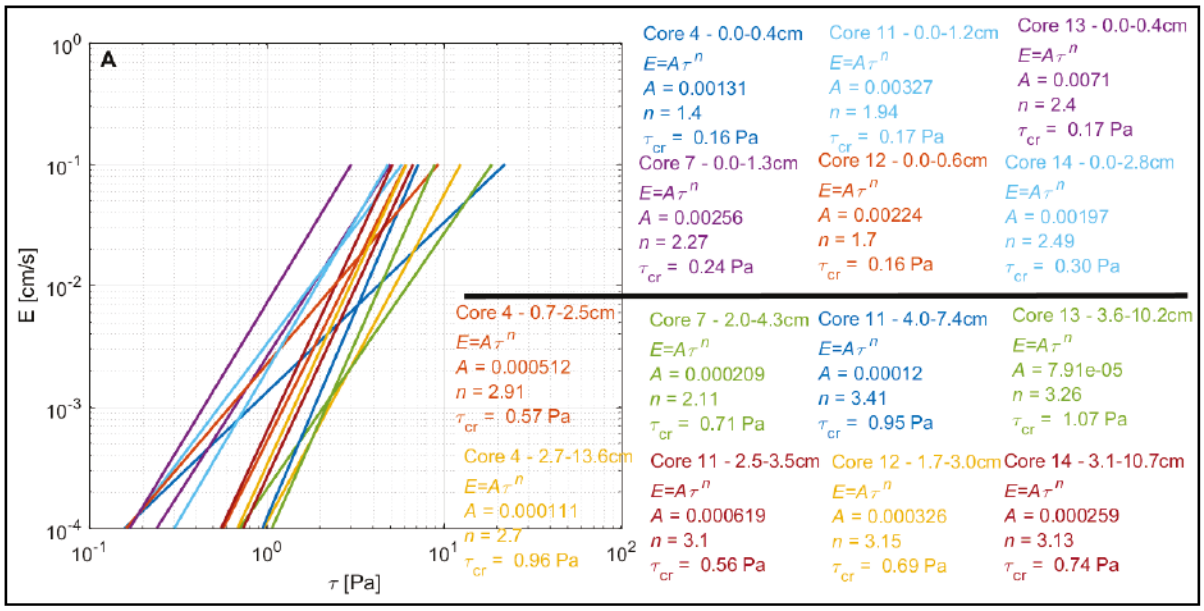

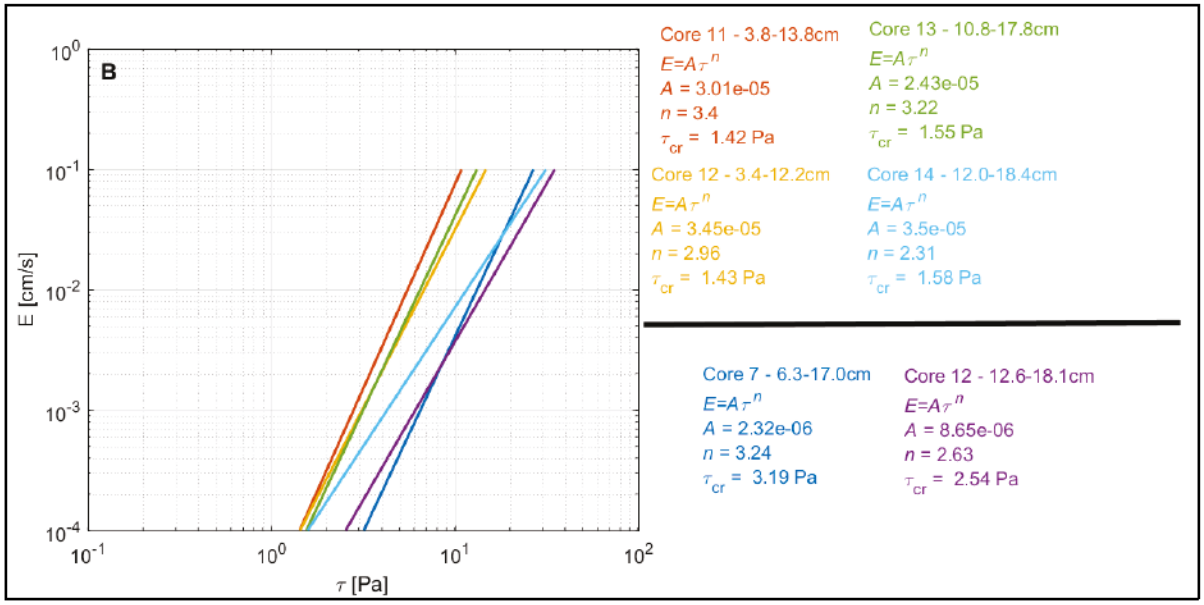

Over-consolidated muds were evident in Cores 2, 3, 6, 9, and 15. The erosion relationships to shear stress for these sediment positions and layers are provided in Figure 16. These layers exhibit greater bed density and erosion resistance at depth than those of the normally consolidated group. Cores 2, 3, 6, 9, and 15 had layers of sand over mud. In these cases, the greater bed density and permeability of the overlying sand contributes to greater consolidation of the underlying mud. Mud beneath the overlying sand was found in densities ranging from 1.33 to 1.57 g/cm3. The erosion data for Core 5b had critical shear stress of 0.70 Pa at the surface and 1.43 Pa in the layer between 2 to 10 cm. In both instances, the critical shear stresses were more reflective of deeper layers in the normally consolidated group. This observation suggests that Core 5b could have experienced a heavier overburden in the past.

Figure 16. Sediment erosion versus depth for over-consolidated cores. Line and text color indicate individual layers.

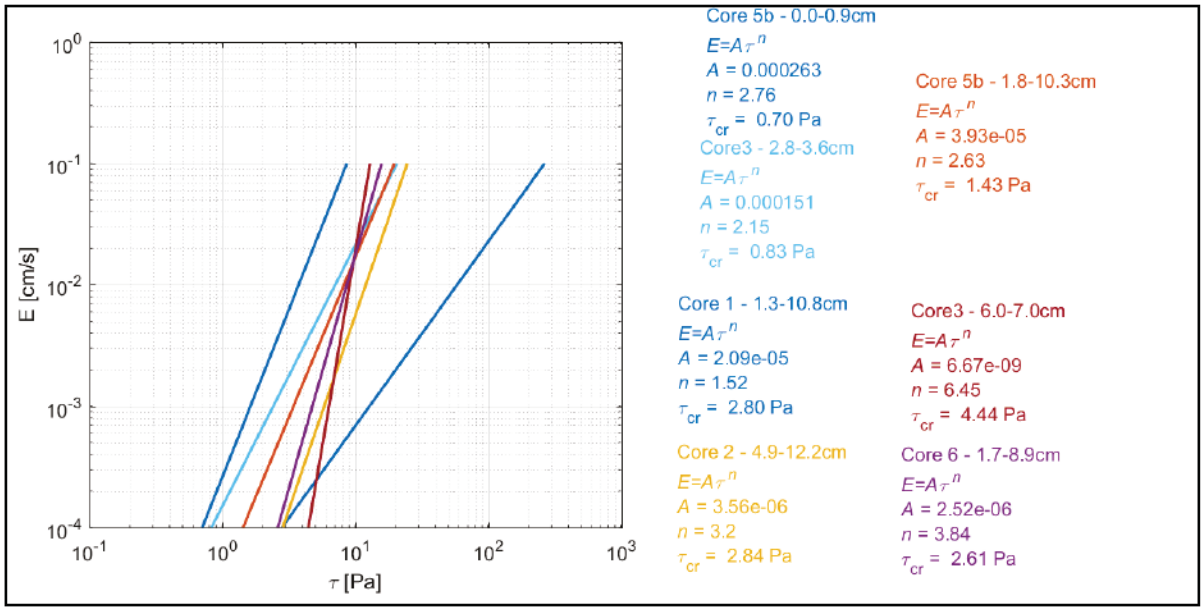

Water column sampling

Water column sampling efforts included sampling of water parameters (temperature and salinity), sampling of suspended sediment concentration, sampling of suspended sediment size, and measurement of suspended particle size and settling velocity. The sampling occurred on 10 and 11 November 2017 at sites PICS01 and PICS02, respectively. The measured (PICS01) and predicted (PICS02) water surfaces near these two locations during the sampling period are provided in Figure 17 along with the times of physical sampling and instrumentation casts.

Figure 17. Water levels near the two water column sampling stations. (A) Measured water levels at Jamestown Ferry Pier, VA (USGS 02042770), near station PICS01; (B) Predicted tides at Hopewell, VA (NOAA 8638481), near station PICS02. Physical sampling times are indicated in black, and sampling times with instrumentation are indicated in red.

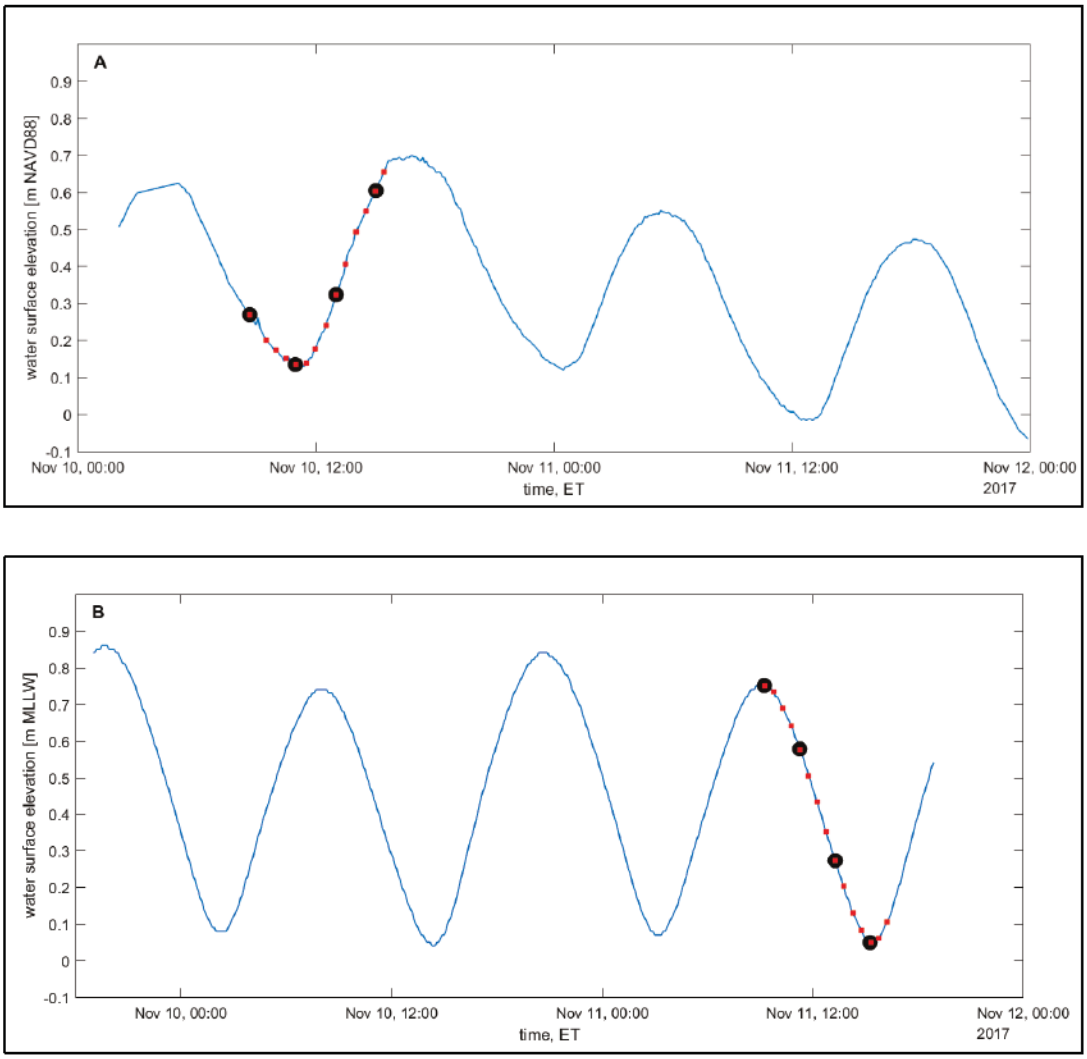

Temperature and salinity

Vertical profiles of temperature and salinity for sites PICS01 and PICS02 are provided in Figures 18 and 19, respectively. Temperature varied with the tides at each site by approximately 1°C. Vertical variation in temperature was slight, typically less than 0.5°C. Salinity varied with the tides at PICS01, with variation on the order of 2 psu. During ebbing tide (08:41–12:00), the surface-to-bottom salinity differences at PICS01 were as much as 1 psu, but during flood tide (13:00–15:25), the vertical salinity gradient was approximately well mixed. The vertical salinity profile was well mixed and essentially fresh at PICS02.

Figure 18. Vertical profiles of temperature and salinity from site PICS01 (10 Nov 2017). Vertical positions (z) are given in meters above bed (mab).

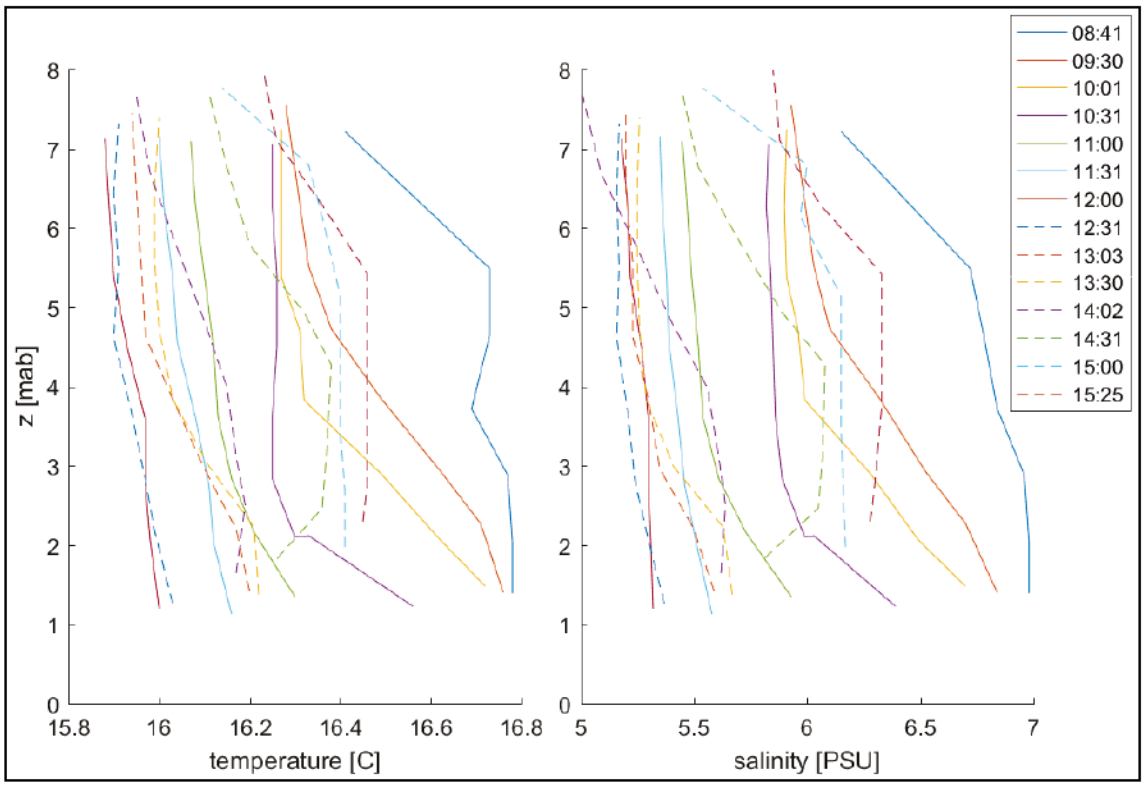

Figure 19. Vertical profiles of temperature and salinity from site PICS02 (11 Nov 2017). Vertical positions (z) are given in mab.

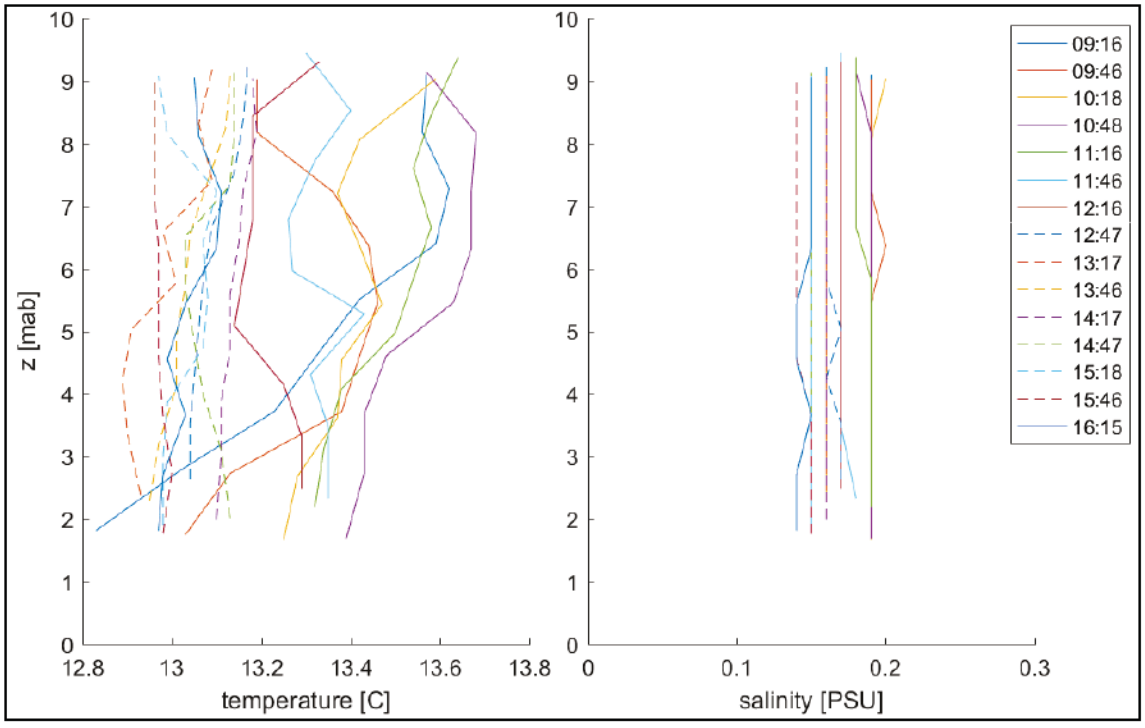

Suspended sediment concentration

Vertical profiles of SSC determined by vacuum filtration of physical samples collected at stations PICS01 and PICS02 are provided in Figure 20. Suspended sediment concentrations were similar at the two sites, ranging from 10 to 66 mg/L at PICS01 and 16 to 69 mg/L at PICS02. Concentrations generally decreased with distance above the bed, but each location had profiles that showed very little difference between near-bed and near-surface sediment concentrations. No measurements of currents or waves were undertaken during the period of sampling, thus limiting the discussion of the hydrodynamic forcing responsible for the time variation in the vertical sediment concentration profiles.

Figure 20. SSC profiles collected at (A) PICS01 (10 Nov 2017) and (B) PICS02 (11 November 2017).

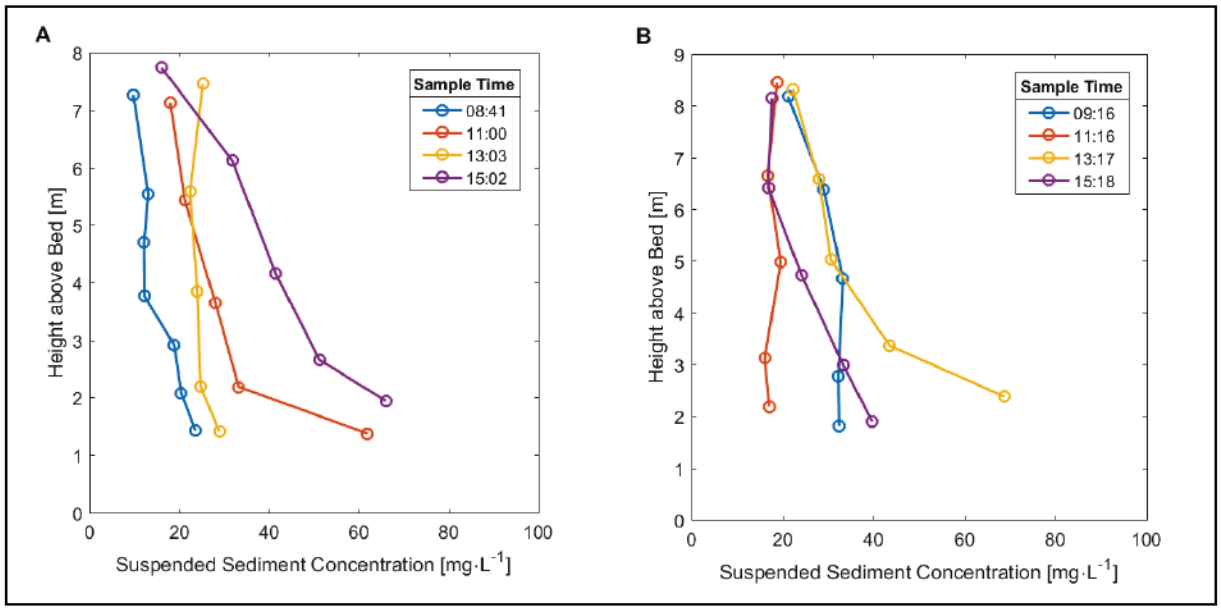

Suspended sediment size and settling velocity

Suspended sediment at stations PICS01 and PICS02 were aggregated, predominantly in the form of low-density flocs. Suspended sediment sizes at these two locations were compared in the aggregated (measured by the LISST-100x in situ) and disaggregated (measured by the laser diffraction method in the laboratory) states (Figure 21). The size distributions presented in Figure 21 are representative of all observations at the two sites. Appendix B provides data from all casts with physical samples. The disaggregated size distributions indicate that the material in suspension is predominantly silt and clay with small fractions of fine sand. The aggregated size distributions suggest that most of the suspended fine

sediment is packaged in aggregates larger than 40 μm. The modal sizes of the disaggregated size distributions are between 10 to 20 μm, and the modal sizes of the aggregated size distributions range from 100 to 200 μm. The truncated peaks at approximately 500 μm (the upper size limit of the LISST-100x) suggest that even larger aggregates exist in suspension.

Figure 21. Suspended sediment size distributions for aggregated (dashed lines) and disaggregated (solid lines) at (A) PICS01, Cast 09 (10 Nov 2017) and (B) PICS02, Cast 09 (11 November 2017).

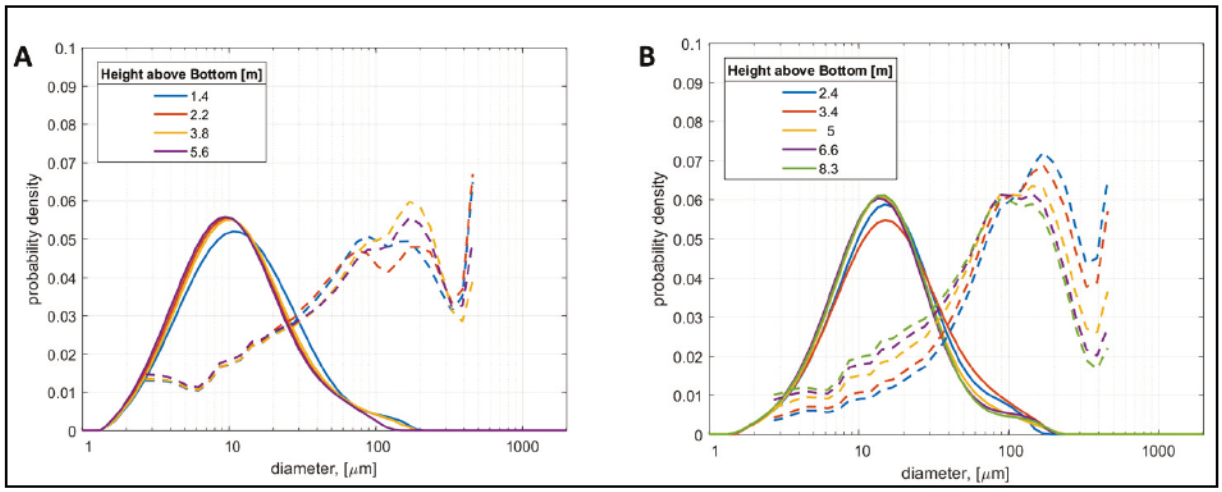

PICS observations quantify the relationship between suspended sediment size and settling velocity. PICS observations at stations PICS01 and PICS02 are compiled in Figure 22 to provide a population view (more than 700,000 particle observations in each set) of the suspended sediment particles. The individual observations span a wide range of particle sizes (30–700 μm), settling velocities (10^{-4} - 6 mm·s^{-1}), and inferred particle densities (1000–2700 kg·m^{-3}). The kernel density estimate (the sediment-mass-weighted density of observations in the plot space) indicates a view of the data similar to those from the LISST-100x in Figure 21. The abundance of suspended aggregates are between 40 to 300 μm, with modal sizes between 100 to 200 μm. Settling velocity of the aggregated particles increases with size and at a rate that is consistent with a near constant or slightly decreasing particle density between 1020 to 1030 kg·m^{-3}. These densities are characteristic of low-density flocs formed in the water column. Very little sediment mass is associated with higher-density particles, such as bed aggregates, which would have densities between 1150 and 1800 kg·m^{-3}. At PICS02, there is a small population of denser particles evident with sizes between 90 to 130 μm and densities of 1100 to 1200 kg·m^{-3} that are distinctly separated from the flocs that are evident at both PICS01 and PICS02. These particles are

characteristic of either eroded bed material or biogenic aggregates, but the mass fraction of these denser aggregates is small, amounting to less than 10% of the suspended mass.

PICS casts were conducted continuously through the tide cycle at each of the stations, allowing examination of the change in suspended particle characteristics with both time and depth. Figure 23 and Figure 24 show the depth-averaged distributions of floc size, settling velocity, and density versus time for stations PICS01 and PICS02, respectively. Both locations show little variance in floc size, settling velocity, or density with time (or tidal conditions).

Figure 22. Compiled size and settling velocity data from (A) PICS01 and (B) PICS02. Each dot indicates an individual particle observation. Contours indicate the sediment-mass-weighted kernel density estimate (density of observations in the plotted space).

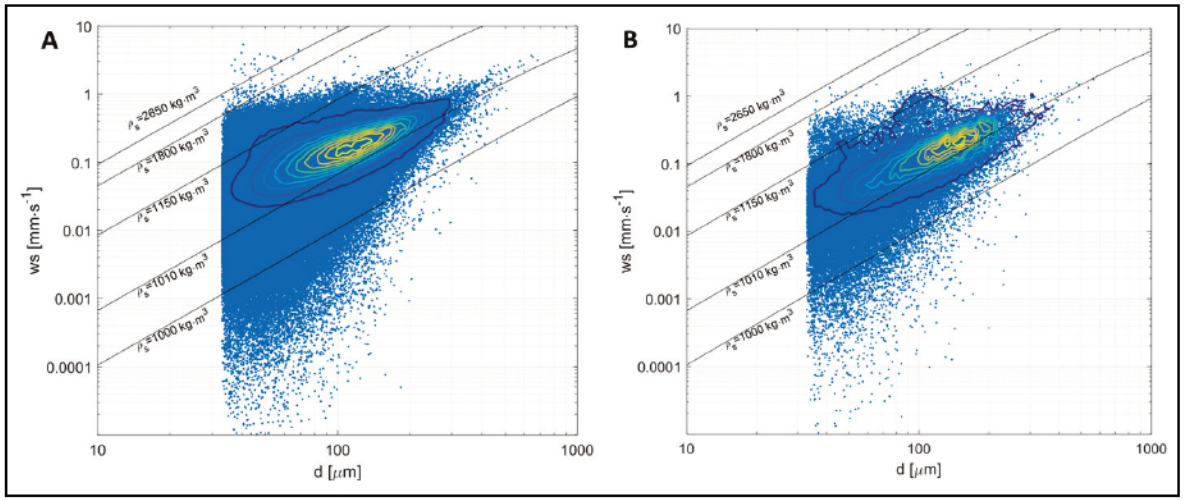

Figure 23. Depth-averaged floc characteristics (size, settling velocity, and density) at PICS01. Symbols (dots) indicate the median value and dashed lines indicate the 16th and 84th percentile values from the distributions.

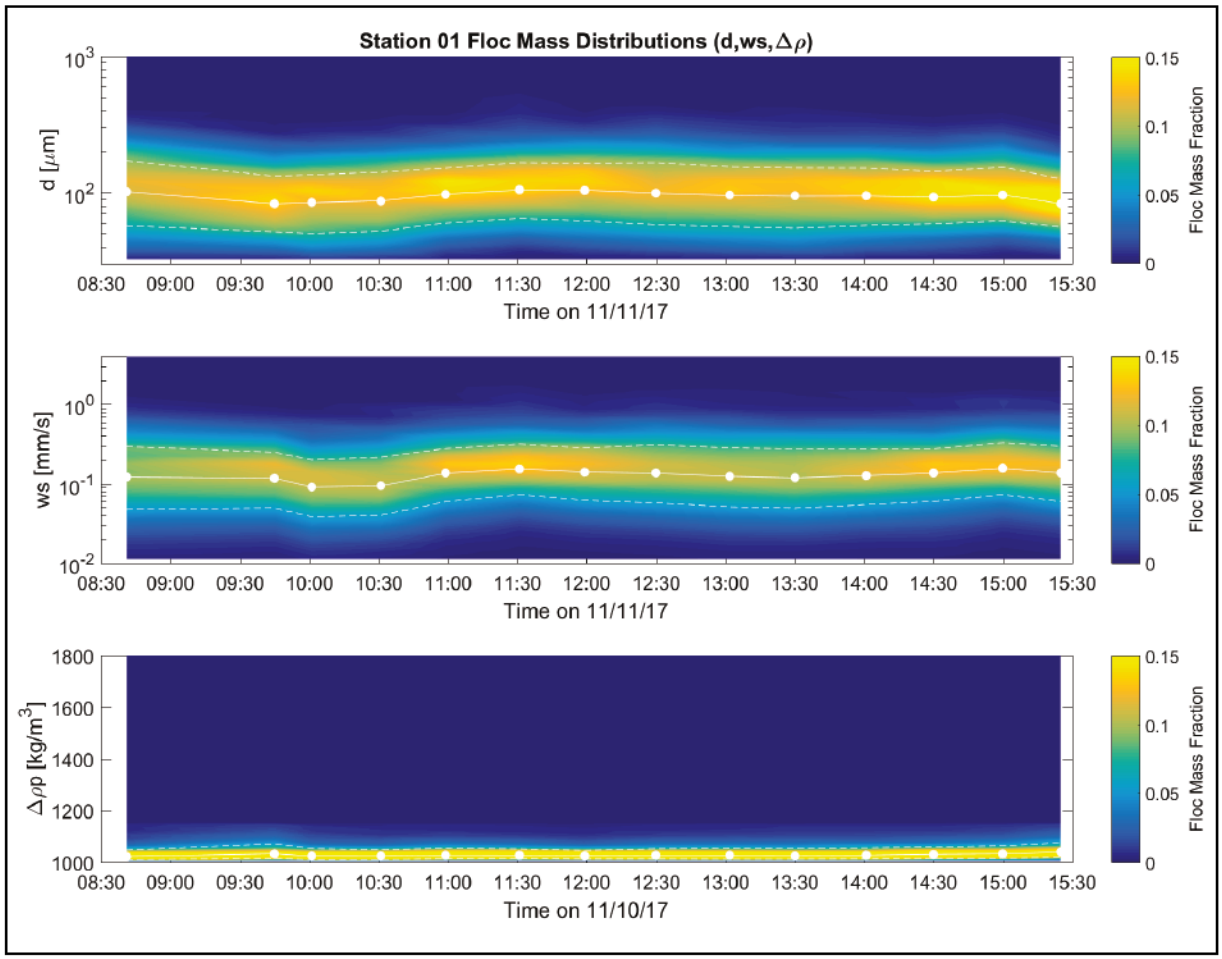

Figure 24. Depth-averaged floc characteristics (size, settling velocity, and density) at PICS02. Symbols (dots) indicate the median value and dashed lines indicate the 16th and 84th percentile values from the distributions.

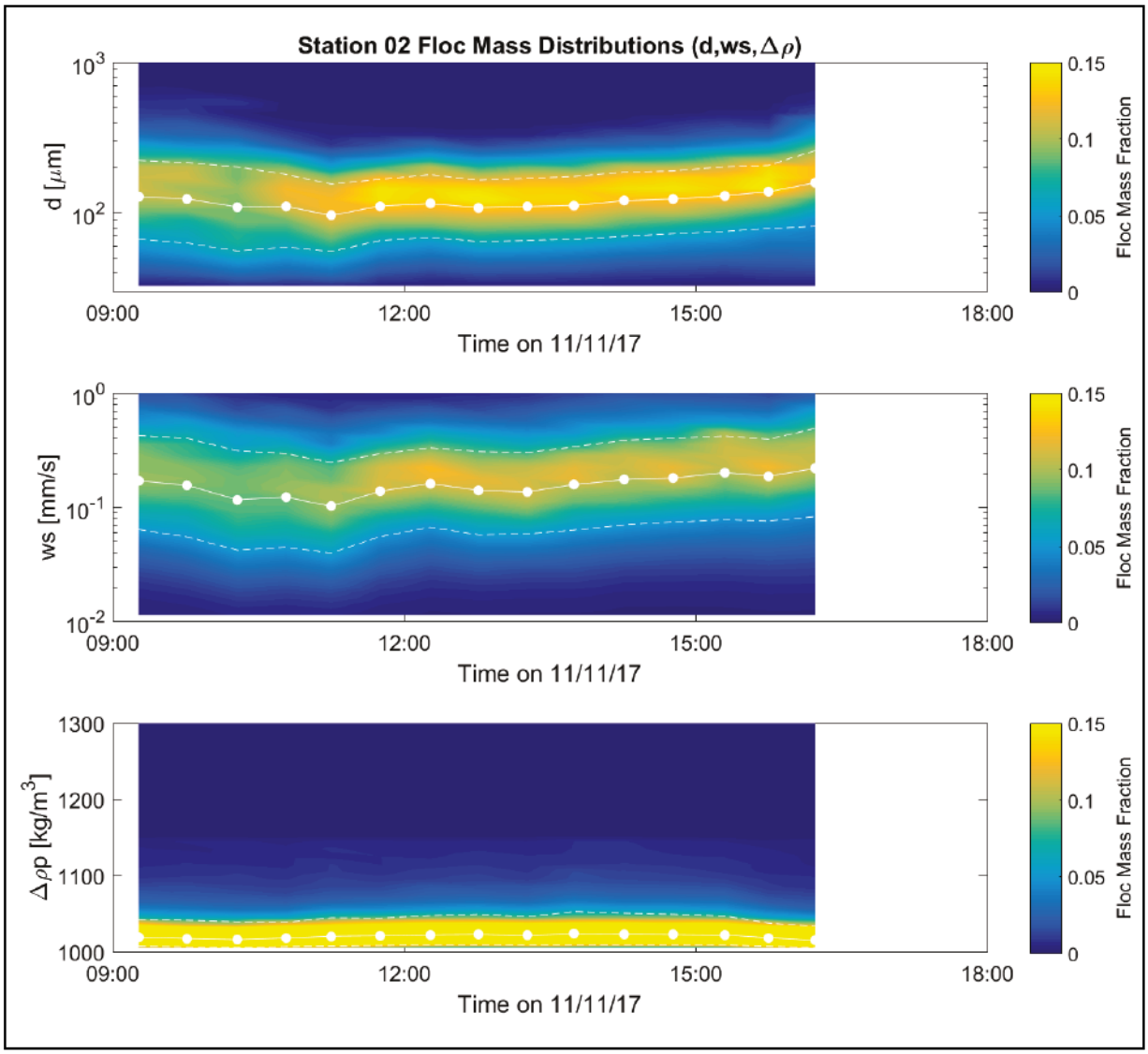

The time-invariant observations of floc characteristics support modeling of suspended flocs with static size classes. Figure 25 provides the time- and depth-averaged size and settling velocity distributions for floc and bed aggregate classes. The floc sizes and settling velocities at PICS01 and PICS02 are very similar, being only slightly larger and faster settling at PICS02 than at PICS01. The bed aggregate class is unimodal at PICS01 with modal size of 50 μm and modal settling velocity of 0.35 mm·s^{-1}. The bed aggregate distributions at PICS02 are bimodal. The smaller and slower settling mode closely matches the bed aggregates at PICS01, and the coarser mode has size of 100 μm and settling velocity of 1 mm·s^{-1}. This

coarser mode is the population with distinctly different particle density evident in Figure 22B. Further examination of the vertical profiles of suspended particles for PICS02 (Figure 26) indicates that the larger, faster settling bed aggregates are more abundant in the upper water column than in the lower water column. The field notes associated with these casts and further examination of the PICS images indicate an abundance of zooplankton within a few meters of the water surface at PICS02. The larger, denser, faster settling particles observed there are likely settling fecal pellets from this population of grazing zooplankton. (The zooplankton themselves are excluded from the data by the automated image processing software.)

Figure 25. Depth- and time-averaged floc size and settling velocity distributions at PICS01(S1) and PICS02(S2).

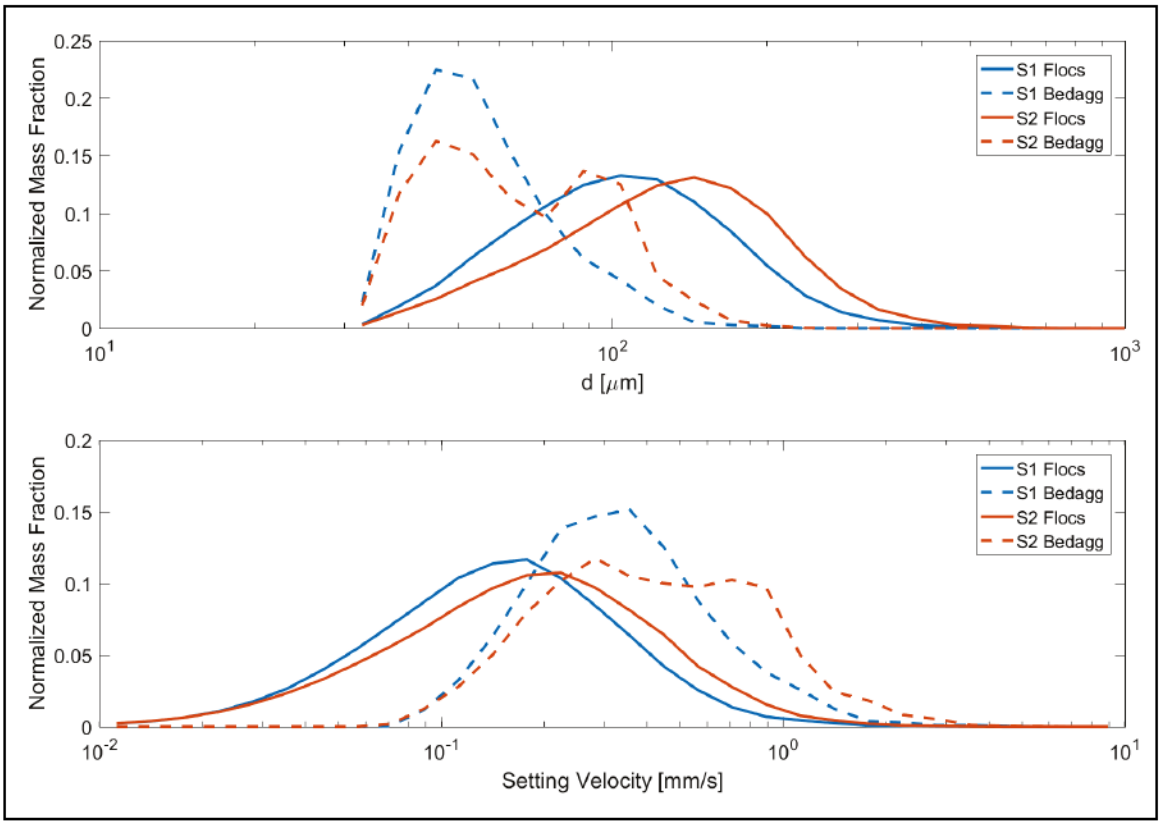

Figure 26. Depth-averaged floc characteristics (size, settling velocity, and density) at PICS02. Symbols (dots) indicate the median value and dashed lines indicate the 16th and 84th percentile values from the distributions.

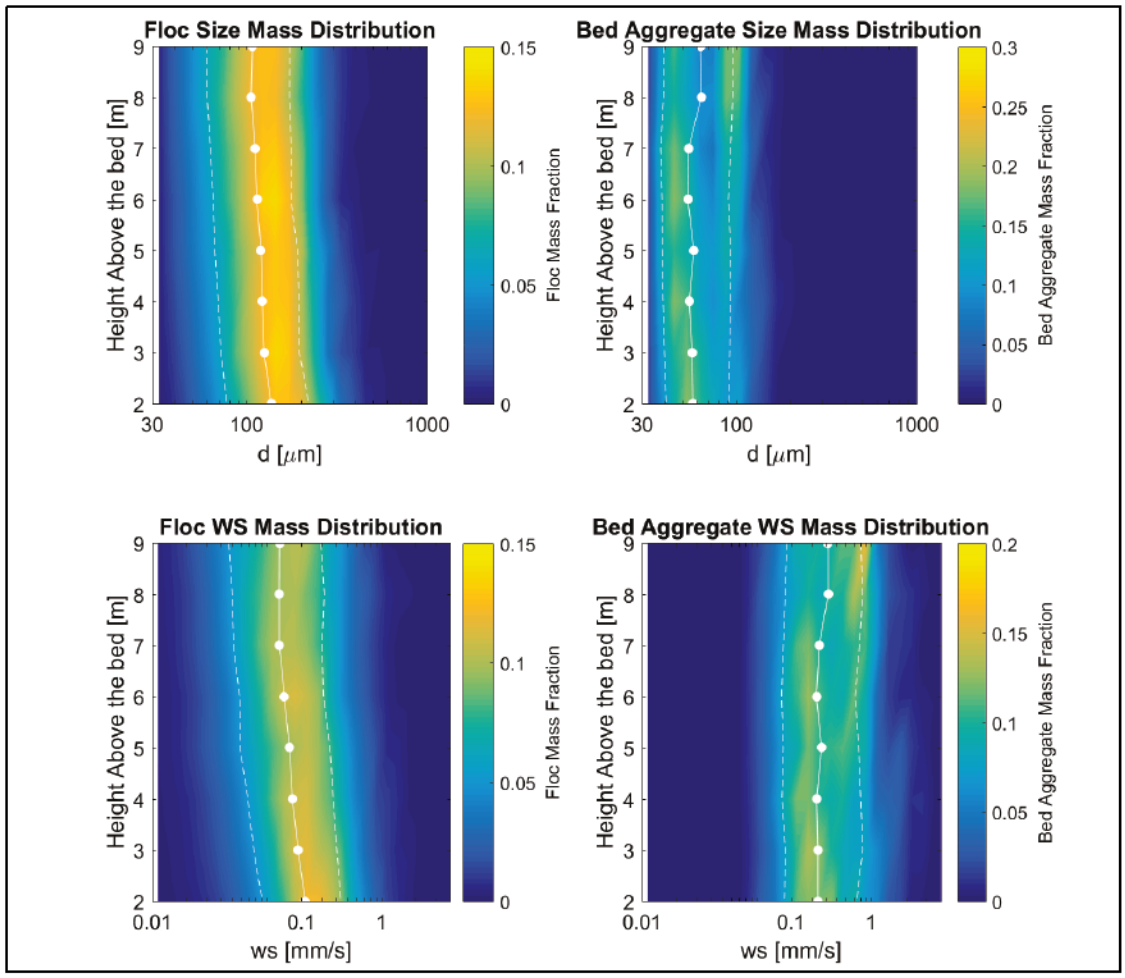

The field observations of suspended sediment lead to modeling recommendations for these particles. The time- and space-invariant nature of the suspended sediment supports a simplified approach of representing the fine sediment as static particle classes composed of flocs formed in the water column and bed aggregates mobilized from the sediment bed. The hydrodynamic conditions during water column sampling were mild and tide dominated. Consequently, the suspended sediment was dominated by low-density flocs formed in the water column or reworked from the recently deposited surface layer of the sediment bed. During this mild period of observation, flocs composed approximately 95% of the suspended sediment mass, and the remaining 5% of suspended sediment mass was in the form of the denser bed aggregates. During more energetic conditions, the fraction of bed aggregates would be expected to increase.

The discretization of the fine sediment classes can be developed from the distributions of fine sediment size and settling velocity presented in Figure 25. The fine-sediment settling velocities are broadly distributed, covering more than an order of magnitude of variation in settling velocity. Consequently, more than one sediment class is recommended to represent the settling velocity distribution. Depending upon the number of fine-sediment classes selected to be modeled, the associated settling velocities can be selected from the settling velocity percentiles provided in Table 4. For instance, three floc classes could be represented by the 16th, 50th, and 84th percentiles of floc settling velocity, with each of the classes receiving one-third of the floc sediment mass.

Table 4. Percentile settling velocities (mm/s) from distributions in Figure 26.

	Flocs					Bed Aggregates				
Station	ws5	ws16	ws50	ws84	ws95	ws5	ws16	ws50	ws84	ws95
PICS01	0.03	0.06	0.13	0.28	0.47	0.11	0.16	0.29	0.54	0.88
PICS02	0.03	0.06	0.16	0.36	0.61	0.12	0.17	0.36	0.79	1.21

4 Summary, Conclusions, and Recommendations

A field study of cohesive sediment processes was conducted in the tidal James River estuary in Virginia. The study objective was to characterize the processes of erosion and settling for a planned numerical modeling study.

Fifteen cores distributed across the estuary and representing varying sediment bed conditions were collected and tested to characterize bed erosion with depth. The results of the erosion testing were analyzed to develop representative erosion parameters for differing bed conditions. To enable extension of the erosion data across the entire estuary, the bed erosion data were grouped based upon bed structure and erosion behavior. Five groups of bed erosion characteristics were developed for sandy beds, three classes of normally consolidated sediments, and one class of over-consolidated sediment.

Suspended sediment concentration and settling velocity were determined from two stations in the mid and upper James River estuary. At each of the stations, suspended sediment concentration, temperature, salinity, and suspended sediment size, settling velocity, and density were determined over a 7 hr period. Salinity stratification and suspended sediment concentration were found to vary with tidal conditions, but the suspended sediment size and settling velocity were found to be relatively constant over tidal conditions during the observation period. The suspended fine sediments were found to be aggregated primarily in the form of low-density flocs with a small fraction, approximately 5% of suspended mass, of denser sediment aggregates (bed aggregates and fecal pellets). The floc size and settling velocity distribution is broad, ranging from 40 to 300 μm and 0.05 to 0.5 $mm \cdot s^{-1}$, respectively. Consequently, multiple fine-sediment size classes were recommended for numerical modeling.

Although the fraction of suspended bed aggregates was low during the period of the water column sampling (a calm period dominated by tidal forcing), the transport of dense bed aggregates could be much more important during stormy conditions. Associated research by Perkey and Smith (2019) and Perkey et al. (2020) highlight the relevance of eroded mud aggregate transport in the James River including field research on James River eroded mud aggregates. This aggregate transport research

suggests that the fraction of suspended bed aggregates would increase during energetic conditions such as increased James River freshwater input or storm conditions over the estuary.

The benefit of these physical cohesive sediment process measurements is the constraint of physical processes in the numerical model. Without constraint, the processes of erosion and settling of fine sediment vary by many orders of magnitude, contributing a high level of uncertainty in the model results. Constraint of the physical processes allows simulation of the processes within a smaller range of measured process values, resulting in a correspondingly reduced level of model uncertainty.

References

Graf, W. H. 1971. *Hydraulics of Sediment Transport*. Chapter 4. New York: McGraw Hill.

Krank, K., E. Petticrew, T. G. Milligan, and I. G. Droppo. 1993. "In Situ Particle Size Distributions Resulting from Flocculation of Suspended Sediment." *Nearshore and Estuarine Cohesive Sediment Transport*. Edited by A. J. Mehta. American Geophysical Union.

Krone, R. B. 1963. *A Study of Rheological Properties of Estuarial Sediments*. Technical Bulletin No. 7. Committee on Tidal Hydraulics. Vicksburg, M: US Army Engineer Waterways Experiment Station.

McNeil, J., C. Taylor, and W. Lick. 1996. "Measurements of Erosion of Undisturbed Bottom Sediments with Depth." *Journal of Hydraulic Engineering* 122(6): 316–324.

Perkey, D. W., and S. J. Smith. 2019. *Impact of Mud Aggregate Processes in Sediment Transport Studies*. ERDC/CHL CHETN-VIII-12. Vicksburg, MS: US Army Engineer Research and Development Center
http://dx.doi.org/10.21079/11681/32005

Perkey, D. W., S. J. Smith, K. A. Fall, G. M. Massey, C. T. Friedrichs, and E.M. Hicks. 2020. "Impacts of Muddy Bed Aggregates on Sediment Transport and Management in the Tidal James River, Virginia." *ASCE Journal of Waterway, Port, Coastal, and Ocean Engineering* 146(5).
https://ascelibrary.org/doi/full/10.1061/%28ASCE%29WW.1943-5460.0000578

Schiller, L., and A. Naumann. 1933. *Über die grundlegenden Berechnungen bei der Schwerkraftaufbereitung*. *VDI* 77: 318.

Smith, S. J., and C. T. Friedrichs. 2011. "Size and Settling Velocities of Cohesive Flocs and Suspended Sediment Aggregates in a Trailing Suction Hopper Dredge Plume." *Continental Shelf Research* 31: S50–S63. doi:10.1016/j.csr.2010.04.002

Smith, S. J., and C. T. Friedrichs. 2015. "Image Processing Methods for In-Situ Estimation of Cohesive Sediment Floc Size, Settling Velocity, and Density." *Limnology and Oceanography: Methods* 13(5): 250–264.
https://doi.org/10.1002/lom3.10022

Torfs, H., J. Jiang, and A. J. Mehta. 2001. "Assessment of the Erodibility of Fine/Coarse Sediment Mixtures." *Coastal and Estuarine Fine Sediment Processes*. Edited by W. H. McAnally and A. J. Mehta. Amsterdam: Elsevier.

van Leussen, W. 1994. *Estuarine Macroflocs and Their Role in Fine-Grained Sediment Transport*. Ministry of Transport, Public Works and Water Management, National Institute for Coastal and Marine Management (RIKZ).

Winterwerp, J. C., and W. G. M. van Kesteren. 2004. *Introduction to the Physics of Cohesive Sediment in the Marine Environment*. *Developments in Sedimentology* series, volume 56. Amsterdam: Elsevier.

Appendix A: Core Descriptions

Appendix A includes core photographs, core descriptions, locations, and analysis of physical samples (Table A-1a through Table A-15c) (Figure A-1a through Figure A-15d).

Table A-1a. Core description, Core 1.

Photograph	Description
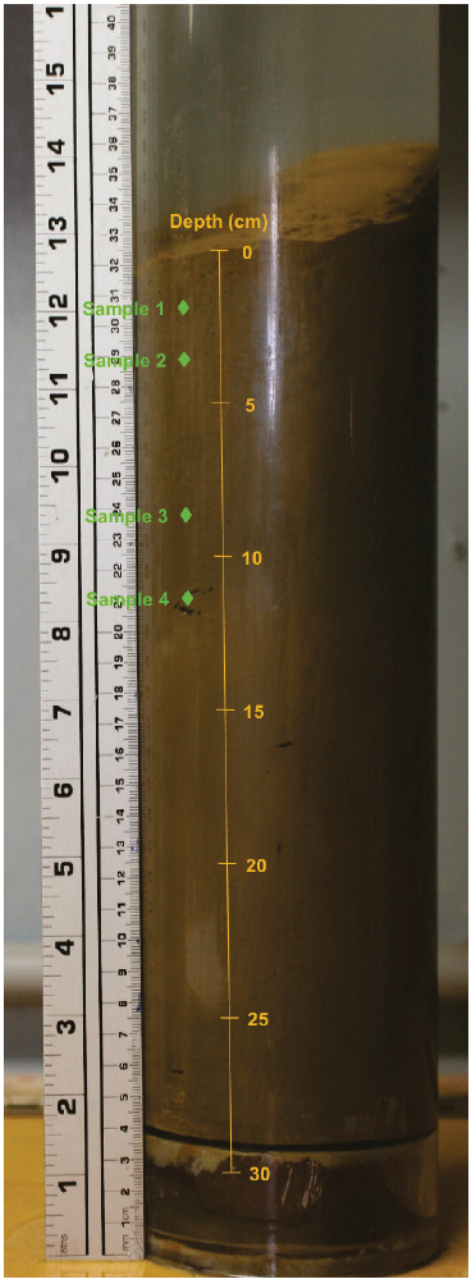	Overlying water. Severely sloped surface composed of fine, brown sediment. Below the surface layer, sediment is brownish-grey colored throughout the remainder of the core. Horizontal linear fissures, ~ 1 cm long, present 10–15 cm below the surface.

Table A-1b. Core surface photographs, Core 1.

Sample 1

Sample 2

Sample 3

Sample 4

Table A-1c. Descriptions of the grain size distributions of physical samples, Core 1.

Sample	Depth [cm]	d10 [µm]	d50 [µm]	d90 [µm]	Fraction Clay	Fraction Silt	Fraction Sand
Core1_1	0.9	3.65	13.96	52.73	0.12	0.81	0.07
Core1_2	3.6	3.72	16.25	64.74	0.11	0.78	0.10
Core1_3	8.7	4.01	16.82	65.10	0.10	0.79	0.11
Core1_4	11.4	3.42	13.08	51.24	0.13	0.80	0.07

Figure A-1a. Cumulative grain size distributions for Core 1 physical samples.

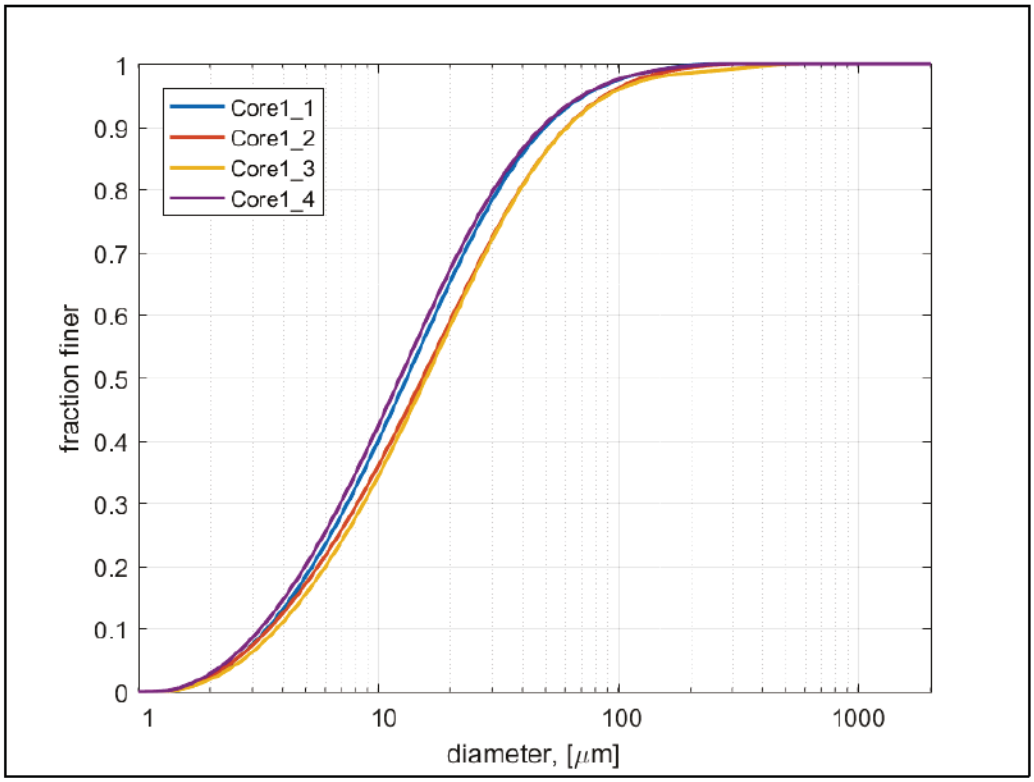

Figure A-1b. Grain size distributions for Core 1 physical samples.

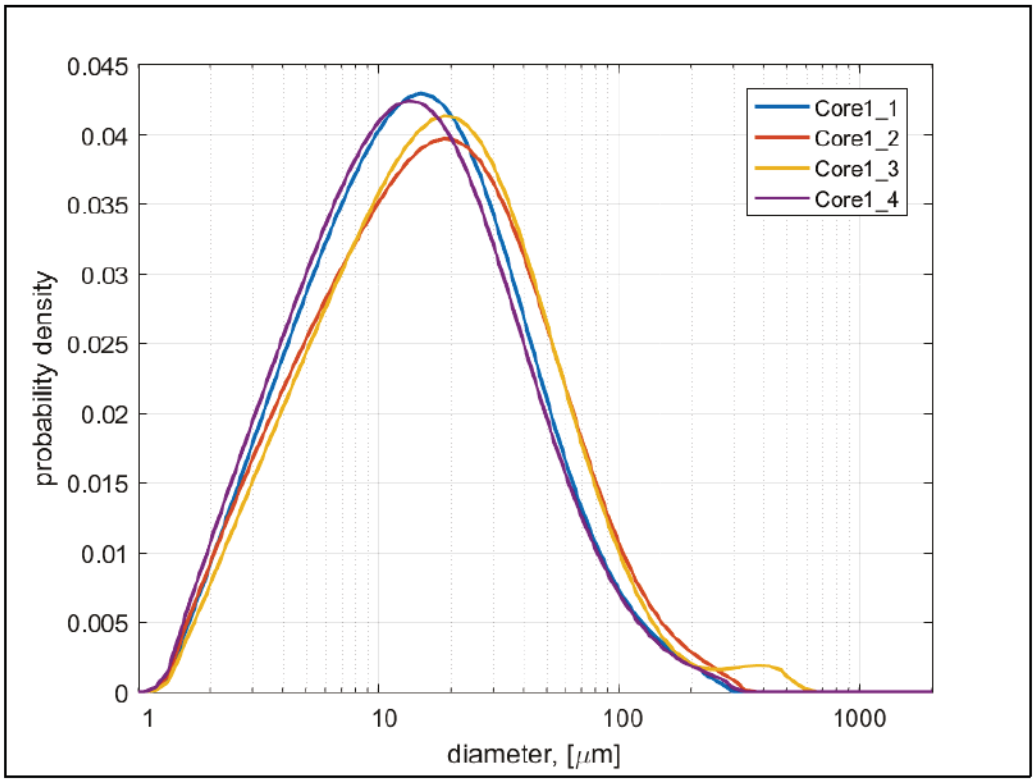

Figure A-1c. Erosion rate at a given applied stress versus depth down core (left). Class fractions and bulk density of physical samples (right) for Core 1.

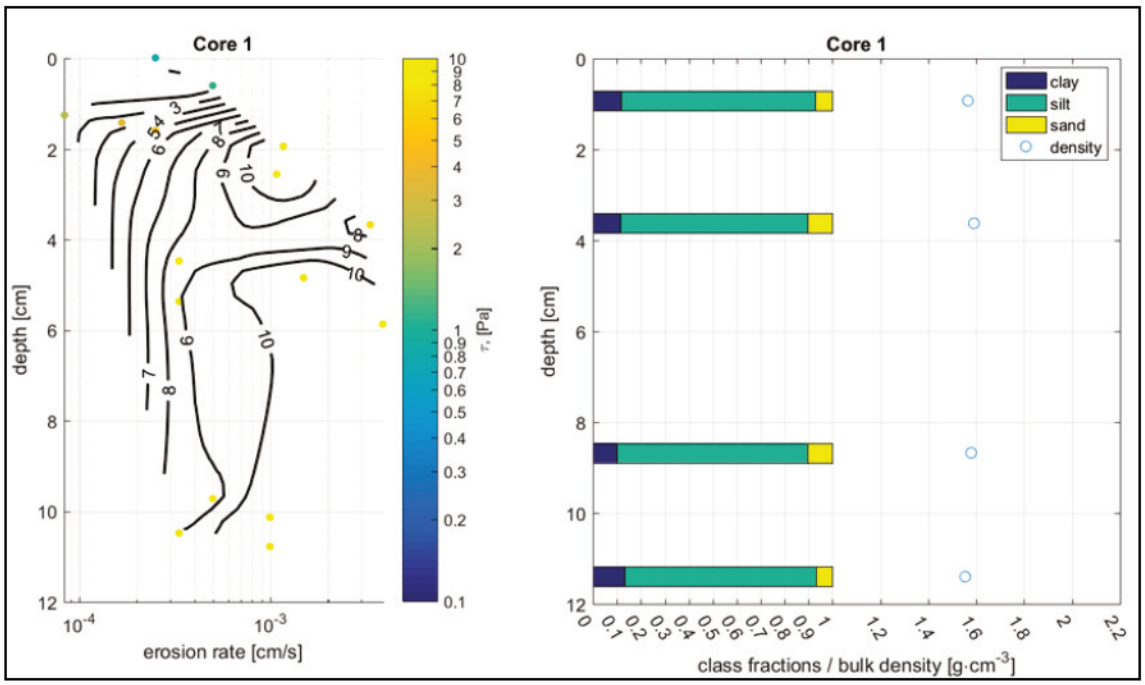

Figure A-1d. Erosion rate versus applied stress and resulting power law fit (s) for Core 1. Symbol color corresponds to depth down core.

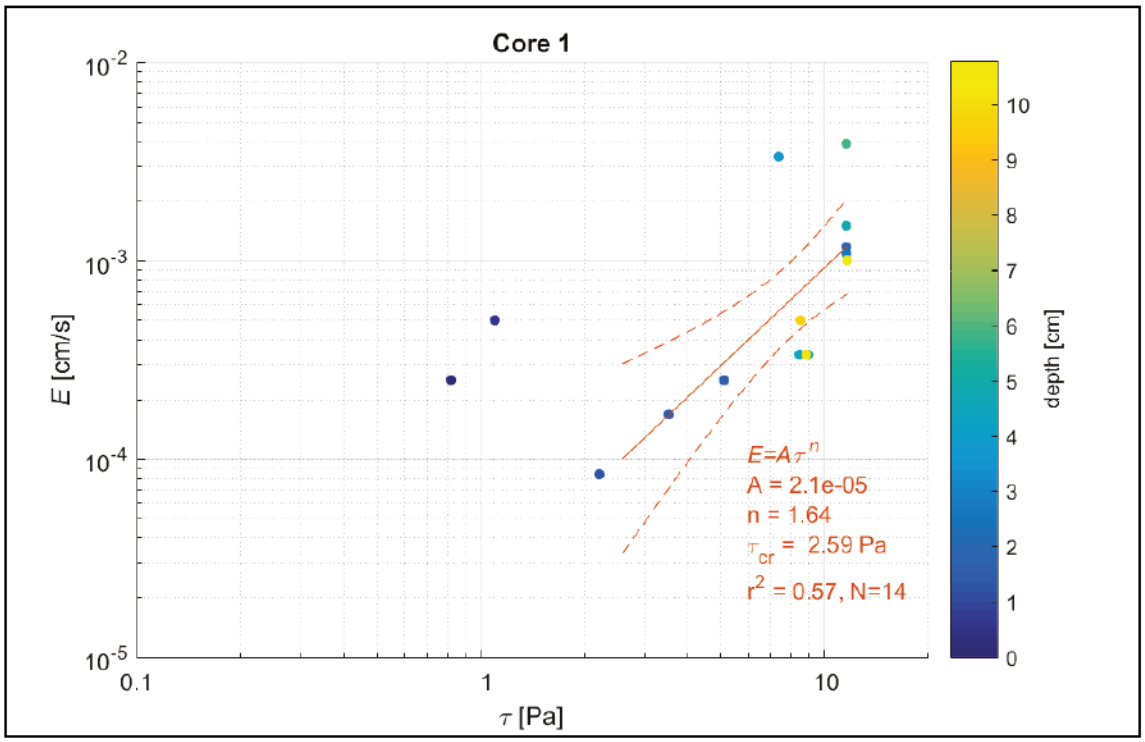

Table A-2a. Core description, Core 2.

Photograph	Description
No photographs taken of core for description.	Smooth, flat core surface composed of fine, light brown sediment and organic material. Evidence of worm tubes and bioturbation in the upper 10 cm of the core. Sediment color brownish-gray throughout the entire core. No visible voids or fractures.

Table A-2b. Core surface photographs Core 2.

Sample 1

Sample 2

Sample 3

Sample 4

Table A-2c. Descriptions of the grain size distributions of physical samples, Core 2.

Sample	Depth [cm]	d10 [µm]	d50 [µm]	d90 [µm]	Fraction Clay	Fraction Silt	Fraction Sand
Core2_1	1.2	16.58	172.48	563.02	0.01	0.20	0.78
Core2_2	4.5	5.60	25.08	116.61	0.06	0.74	0.21
Core2_3	10.6	5.60	27.49	106.19	0.06	0.72	0.22
Core2_4	12.6	5.48	25.03	94.20	0.06	0.75	0.19

Figure A-2a. Cumulative grain size distributions for Core 2 physical samples.

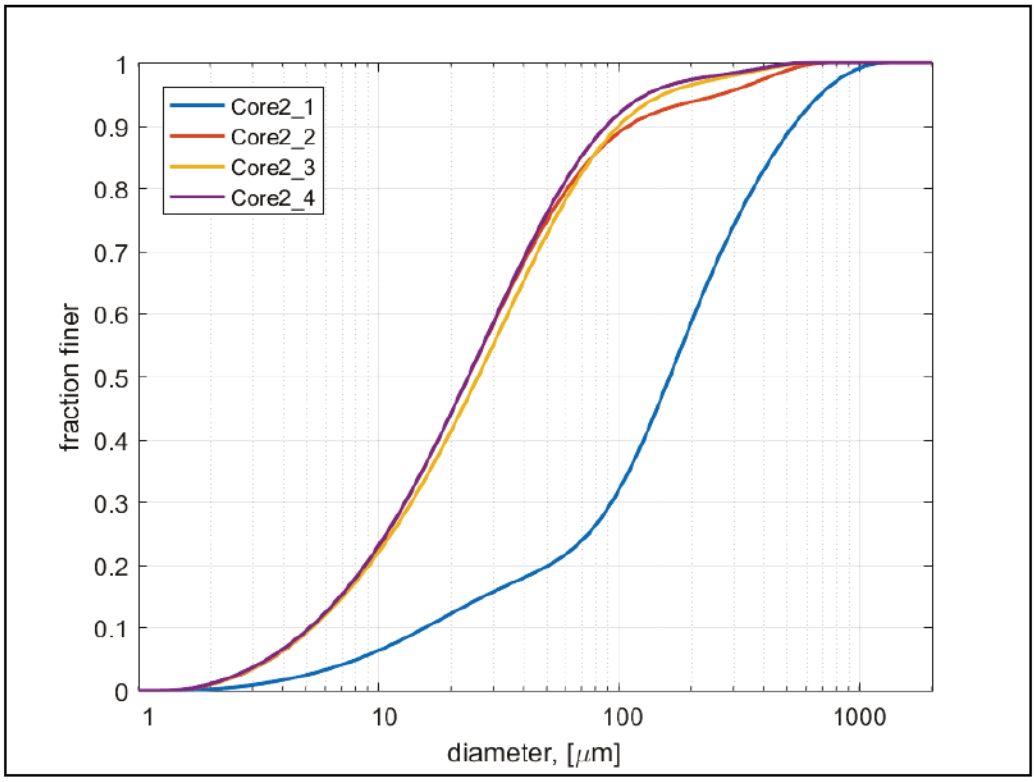

Figure A-2b. Grain size distributions for Core 2 physical sample.

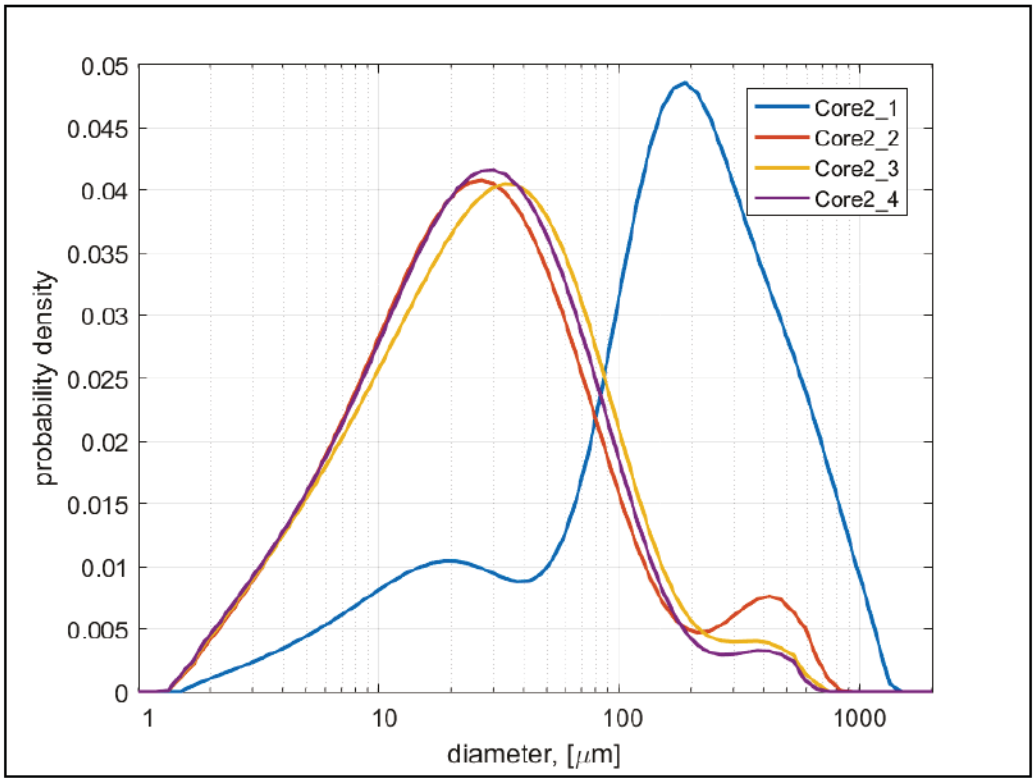

Figure A-2c. Erosion rate at a given applied stress versus depth down core (left). Class fractions and bulk density of physical samples (right) for Core 2.

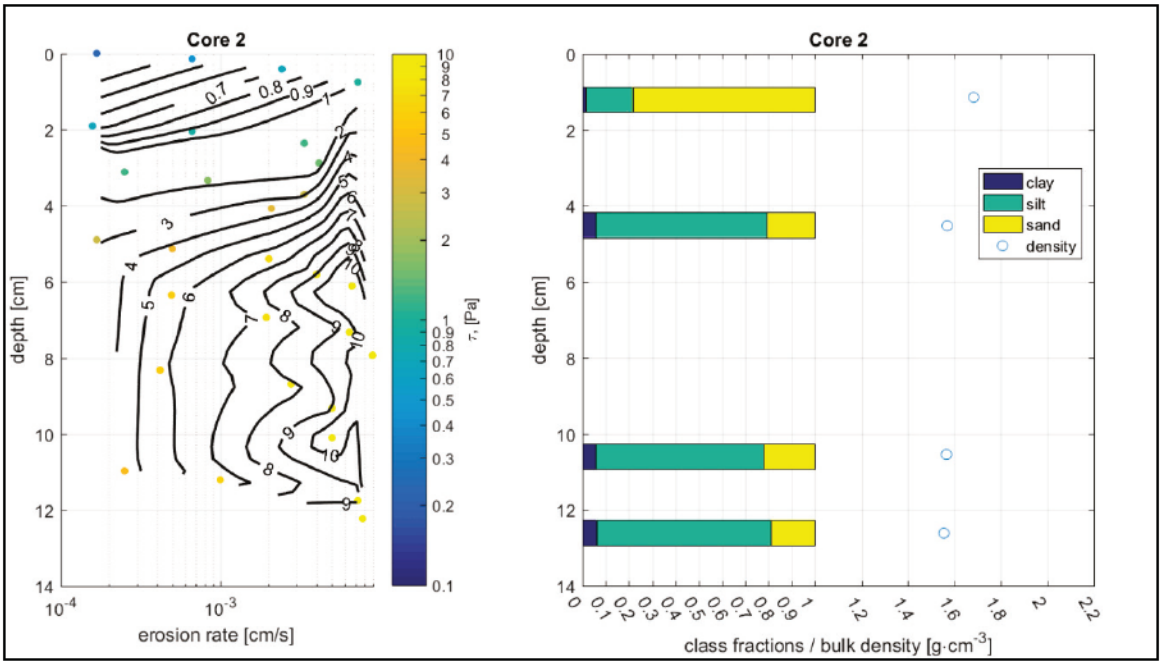

Figure A-2d. Erosion rate versus applied stress and resulting power law fit (s) for Core 2. Symbol color corresponds to depth down core.

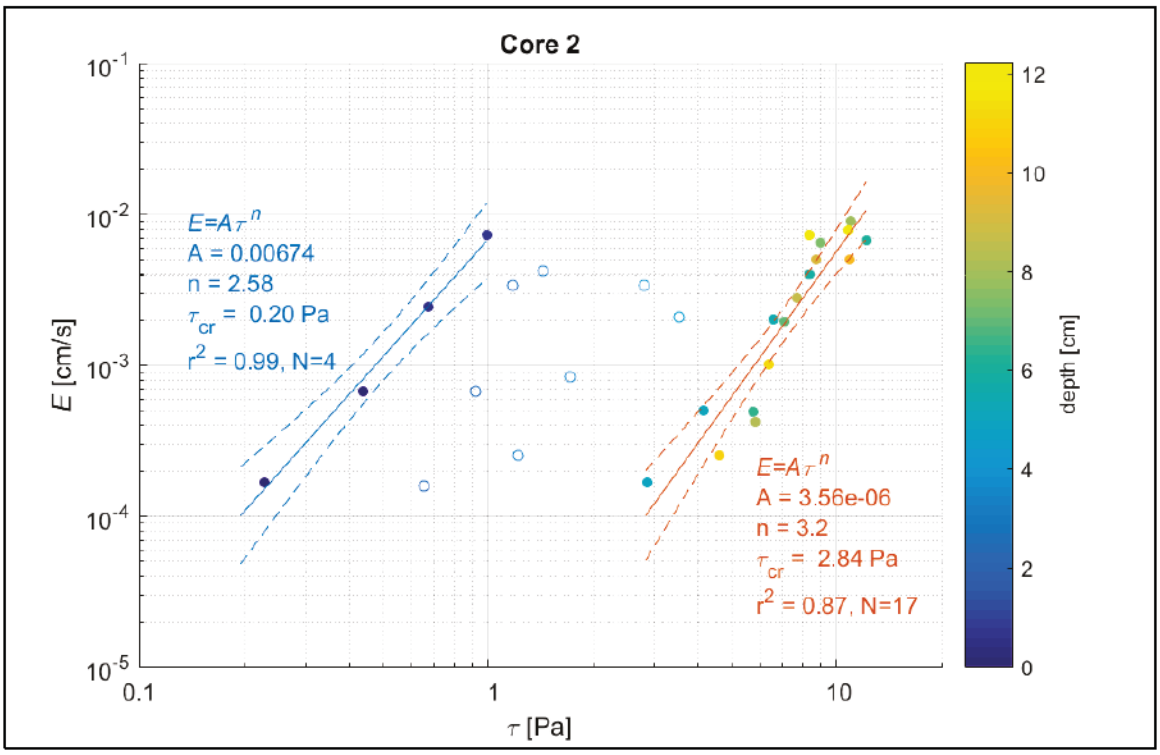

Table A-3a. Core description, Core 3.

Photograph	Description
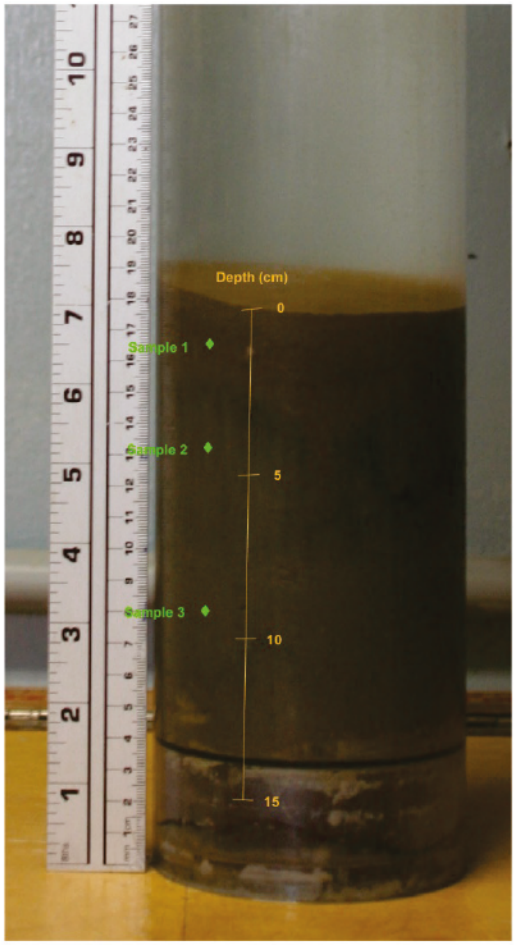	Overlying water. Smooth, but sloped core surface composed of light brown fine sediment. Sediment transitions to light grey color material ~ 0.5–2 cm down core. Visible linear void ~2 cm in diameter at a depth of ~ 8 cm down core. Smaller ~0.2–0.5 cm diameter voids visible 6–10 cm down core.

Table A-3b. Core surface photographs, Core 3.

Sample 1

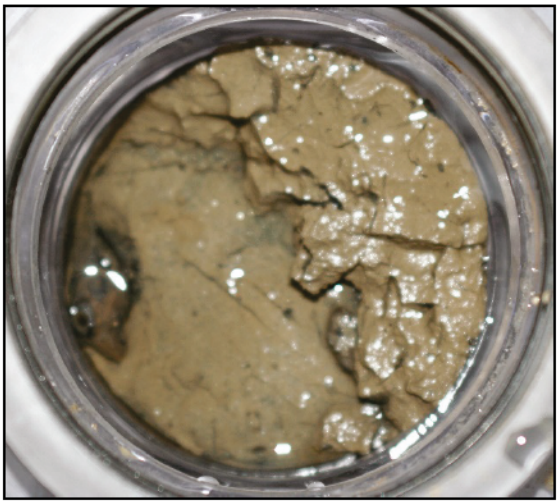

Sample 2

Sample 3

Table A-3c. Descriptions of the grain size distributions of physical samples, Core 3.

Sample	Depth [cm]	d10 [µm]	d50 [µm]	d90 [µm]	Fraction Clay	Fraction Silt	Fraction Sand
Core3_1	0.9	10.49	104.54	254.73	0.03	0.32	0.65
Core3_2	4.1	4.44	17.42	80.84	0.08	0.77	0.14
Core3_3	9.1	4.94	19.82	79.30	0.07	0.79	0.15

Figure A-3a. Cumulative grain size distributions for Core 3 physical samples.

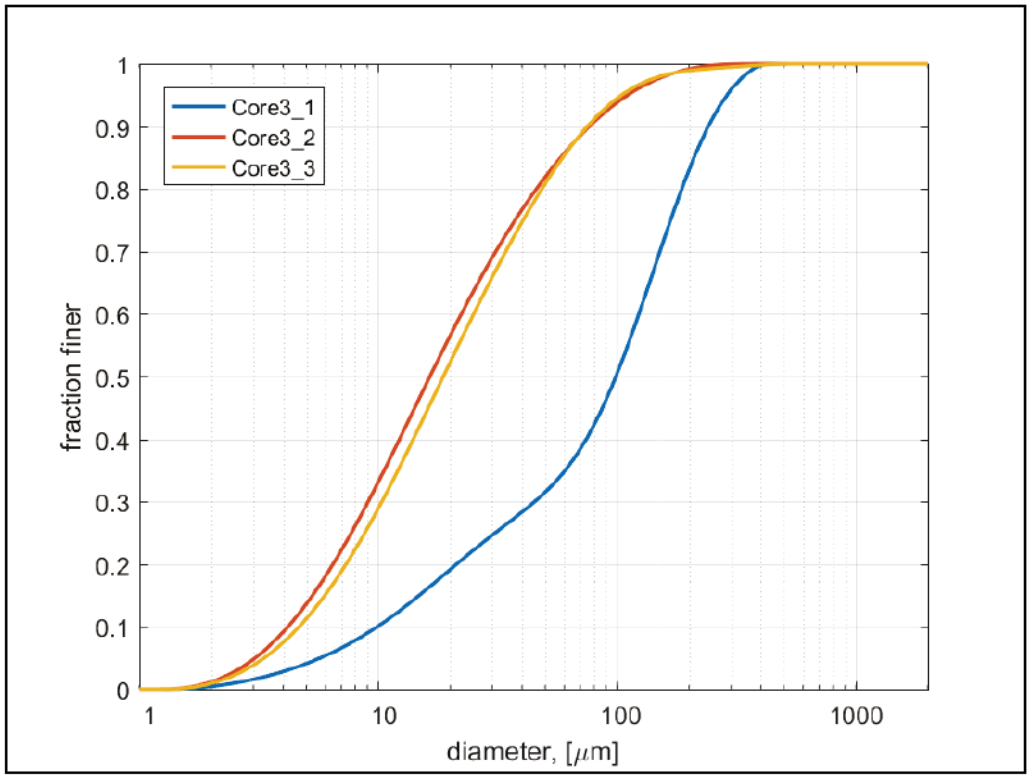

Figure A-3b. Grain size distributions for Core 3 physical samples.

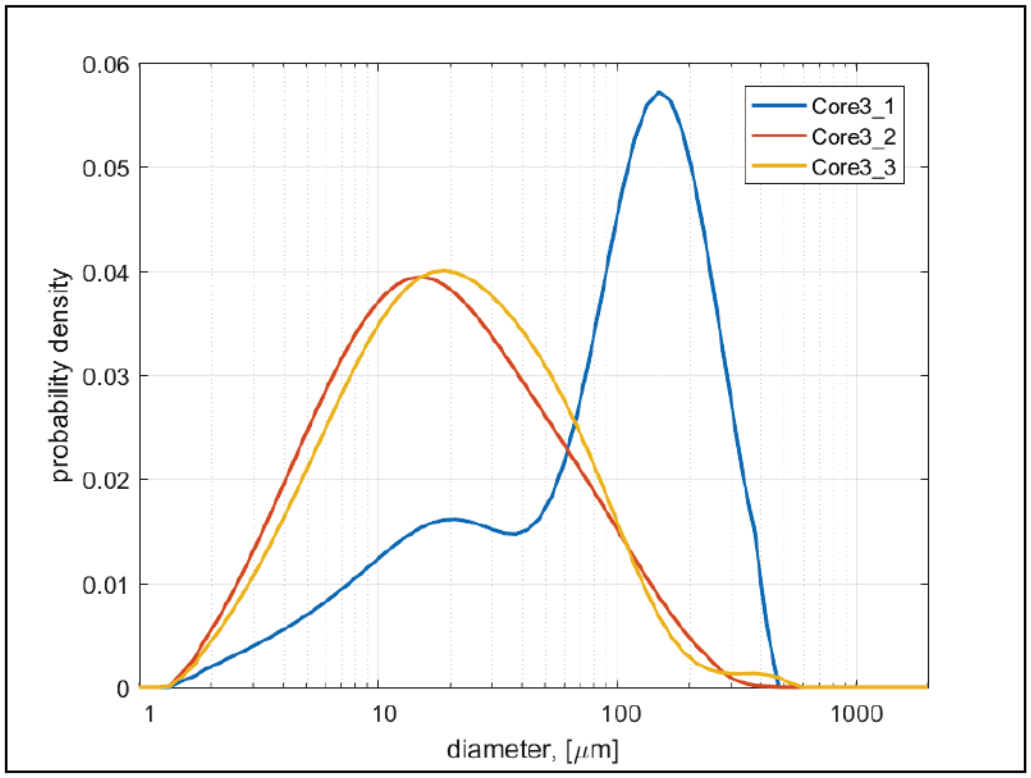

Figure A-3c. Erosion rate at a given applied stress versus depth down core (left). Class fractions and bulk density of physical samples (right) for Core 3.

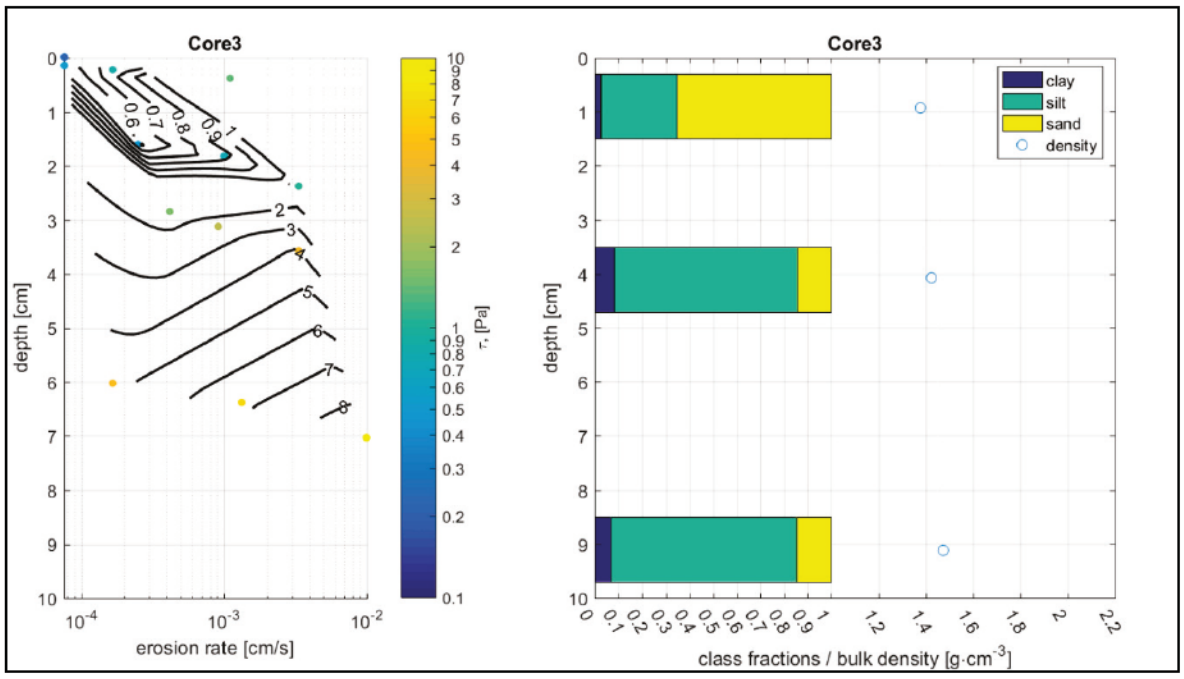

Figure A-3d. Erosion rate versus applied stress and resulting power law fit (s) for Core 3. Symbol color corresponds to depth down core.

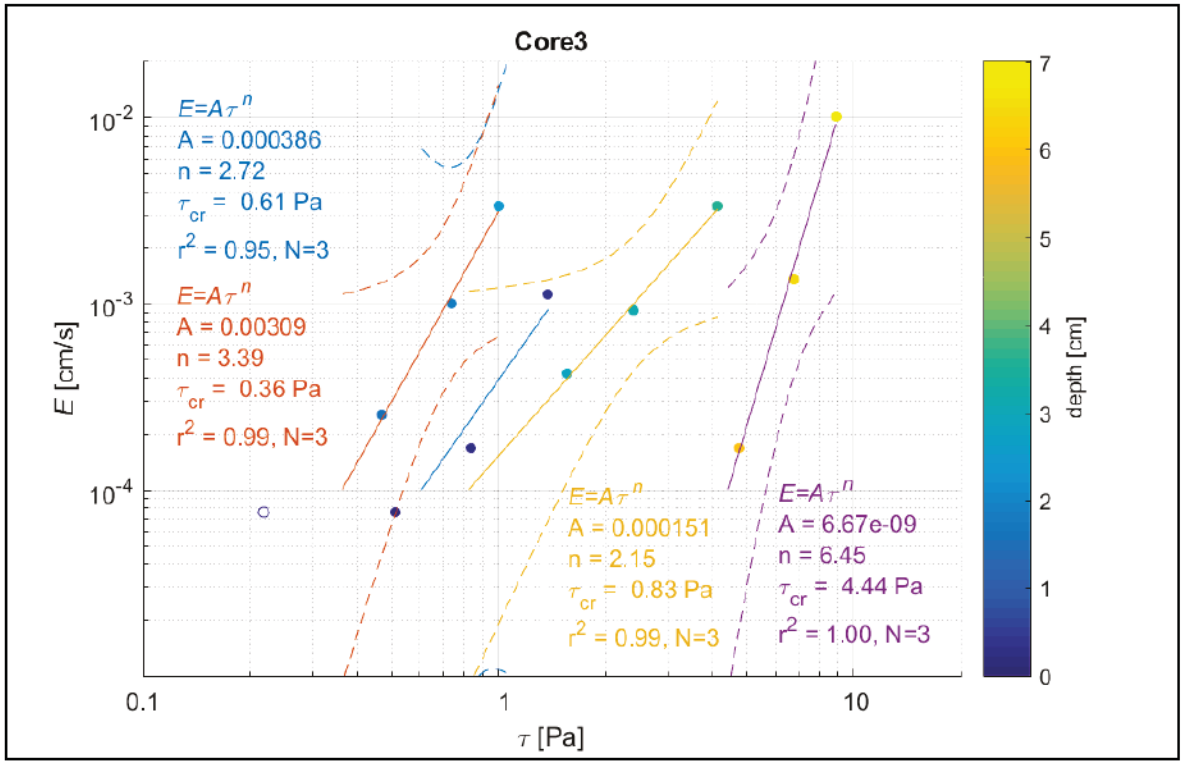

Table A-4a. Core description, Core 4.

Photograph	Description
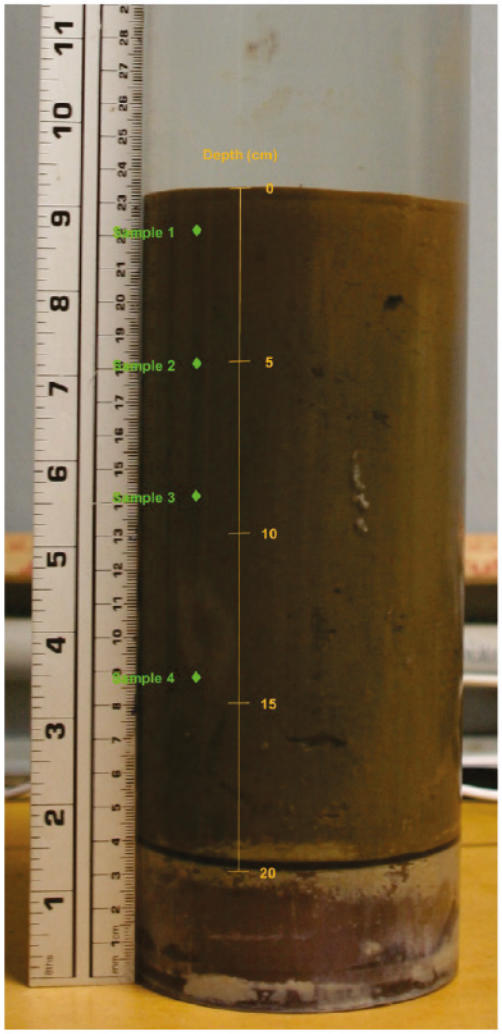	Overlying water.
	Level surface composed of fine light brown sediment.
	Below ~0.3 cm, color transitions to brownish-gray that is consistent throughout the remainder of the core. Visual evidence of bioturbation and presence of worm tubes down to a depth of 5–8 cm. Multiple voids visible throughout much of the core ranging in size from 0.3–0.6 cm in diameter.

Table A-4b. Core surface photographs, Core 4.

Sample 1

Sample 2

Sample 3

Sample 4

Table A-4c. Descriptions of the grain size distributions of physical samples, Core 4.

Sample	Depth [cm]	d10 [µm]	d50 [µm]	d90 [µm]	Fraction Clay	Fraction Silt	Fraction Sand
Core4_1	1.2	5.84	24.62	102.63	0.04	0.72	0.23
Core4_2	5	6.06	32.03	102.34	0.04	0.69	0.26
Core4_3	8.9	5.87	35.72	125.55	0.05	0.62	0.33
Core4_4	14.2	4.43	16.34	88.67	0.08	0.76	0.16

Figure A-4a. Cumulative grain size distributions for Core 4 physical samples.

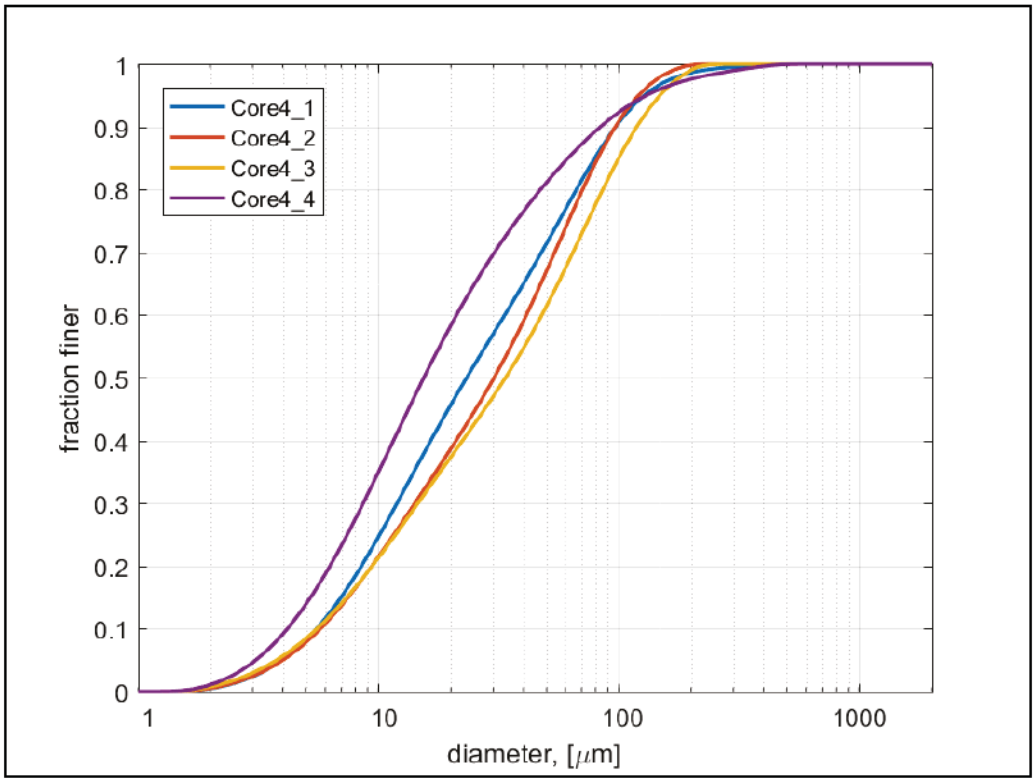

Figure A-4b. Grain size distributions for Core 4 physical samples.

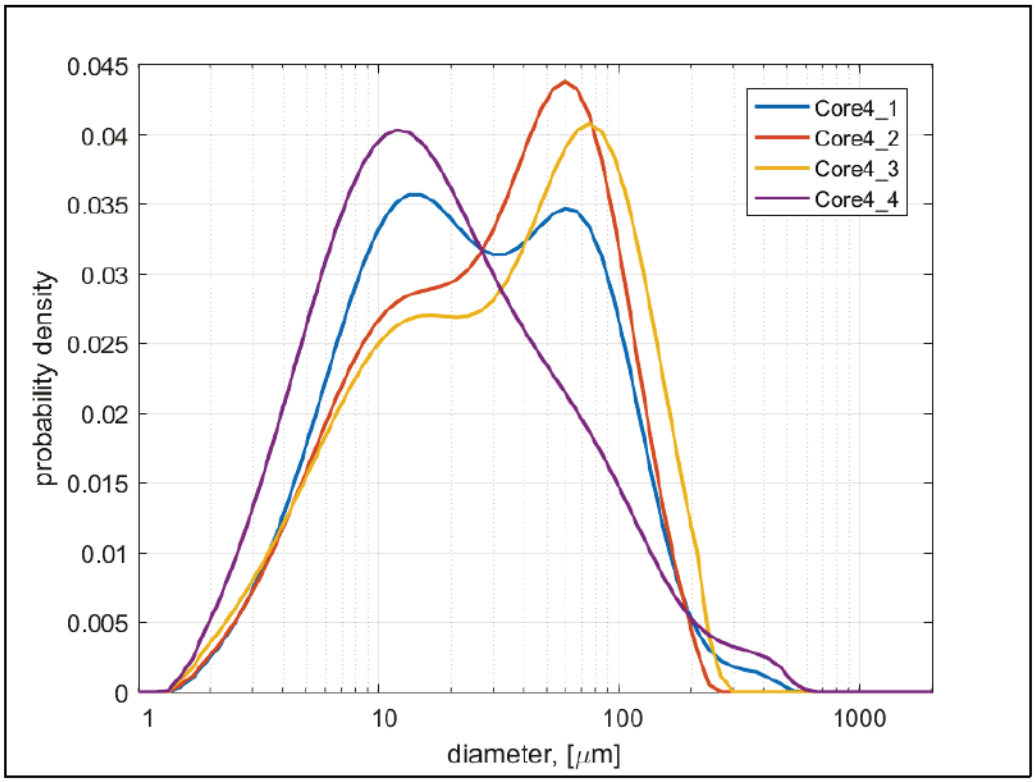

Figure A-4c. Erosion rate at a given applied stress versus depth down core (left). Class fractions and bulk density of physical samples (right) for Core 4.

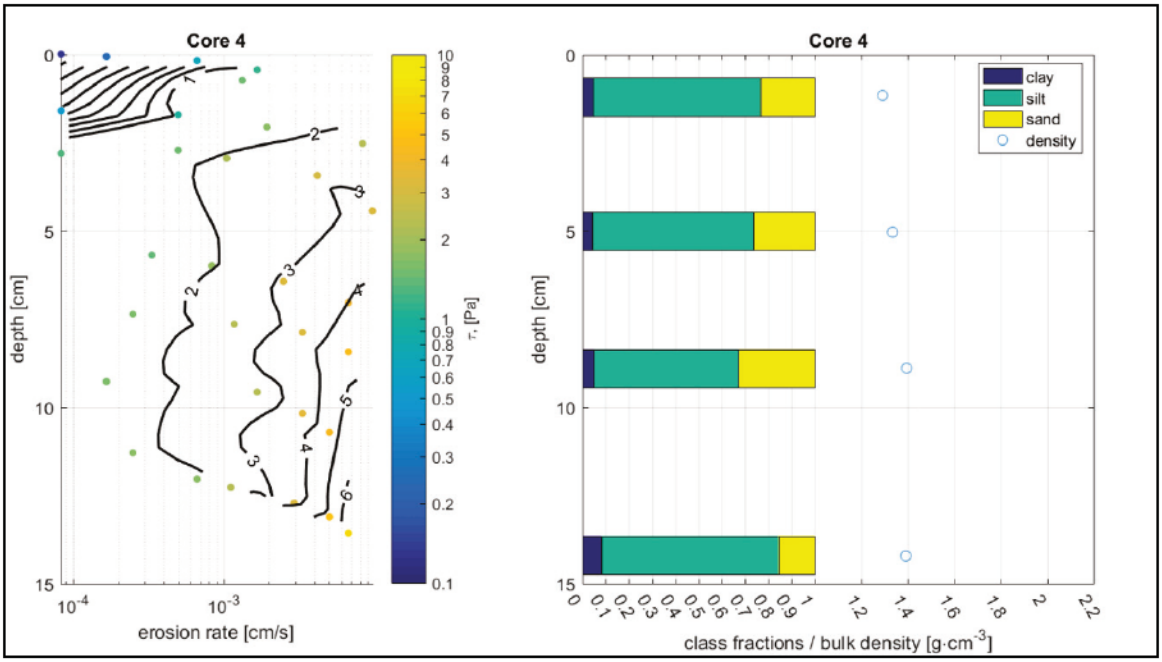

Figure A-4d. Erosion rate versus applied stress and resulting power law fit (s) for Core 4. Symbol color corresponds to depth down core.

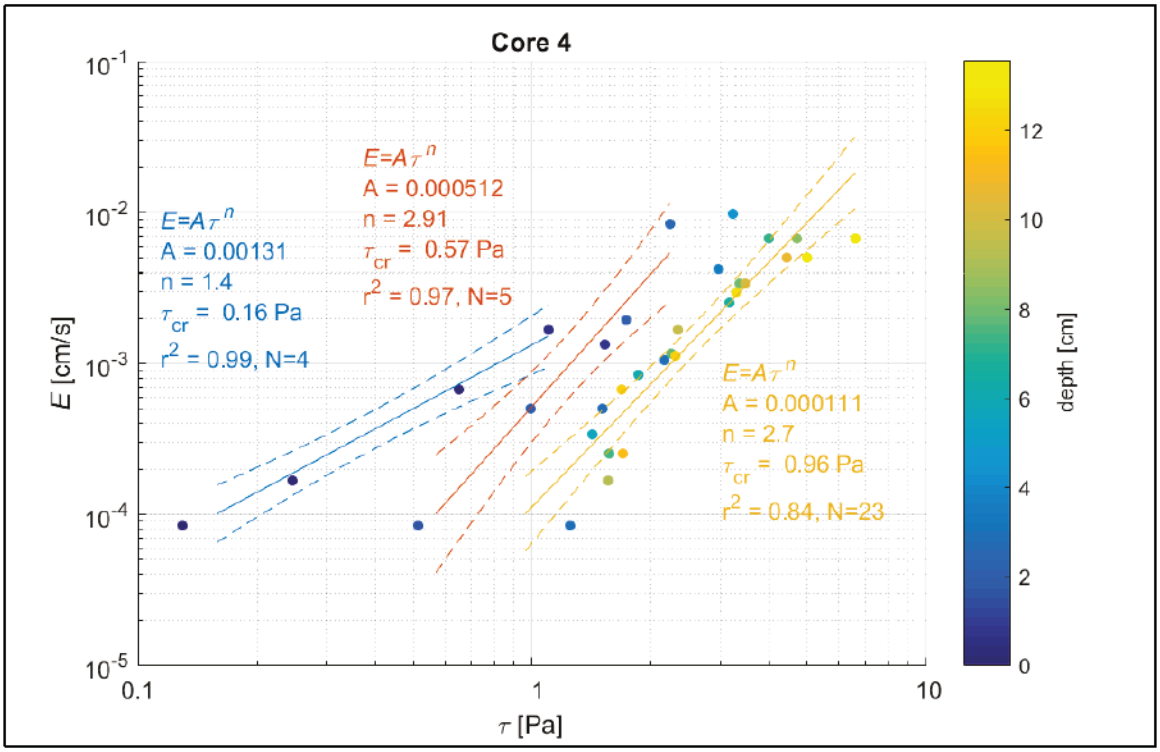

Table A-5a. Core description, Core 5b.

Photograph	Description
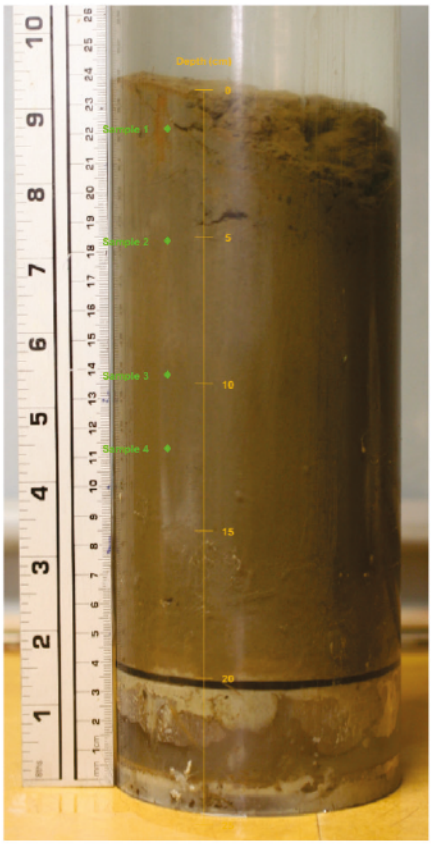	Overlying water.
	Sloped surface composed of light brown, fine sediment. Downslope surface appears to have been fractured and disturbed from collection. Sediment transitions to brownish-grey color material within the upper 1 cm of the core.
	A linear void/worm tube ~4 cm in length is visible ~ 5 cm below the surface.

Table A-5b. Core surface photographs, Core 5b.

Sample 1

Sample 2

Sample 3

Sample 4

Table A-5c. Descriptions of the grain size distributions of physical samples, Core 5b.

Sample	Depth [cm]	d10 [µm]	d50 [µm]	d90 [µm]	Fraction Clay	Fraction Silt	Fraction Sand
Core5_1	1.3	4.78	21.87	101.72	0.07	0.73	0.20
Core5_2	5.2	4.82	23.48	99.04	0.07	0.73	0.20
Core5_3	9.7	5.22	25.01	98.86	0.06	0.73	0.21
Core5_4	12.2	5.27	24.43	97.59	0.06	0.74	0.21

Figure A-5a. Cumulative grain size distributions for Core 5b physical samples.

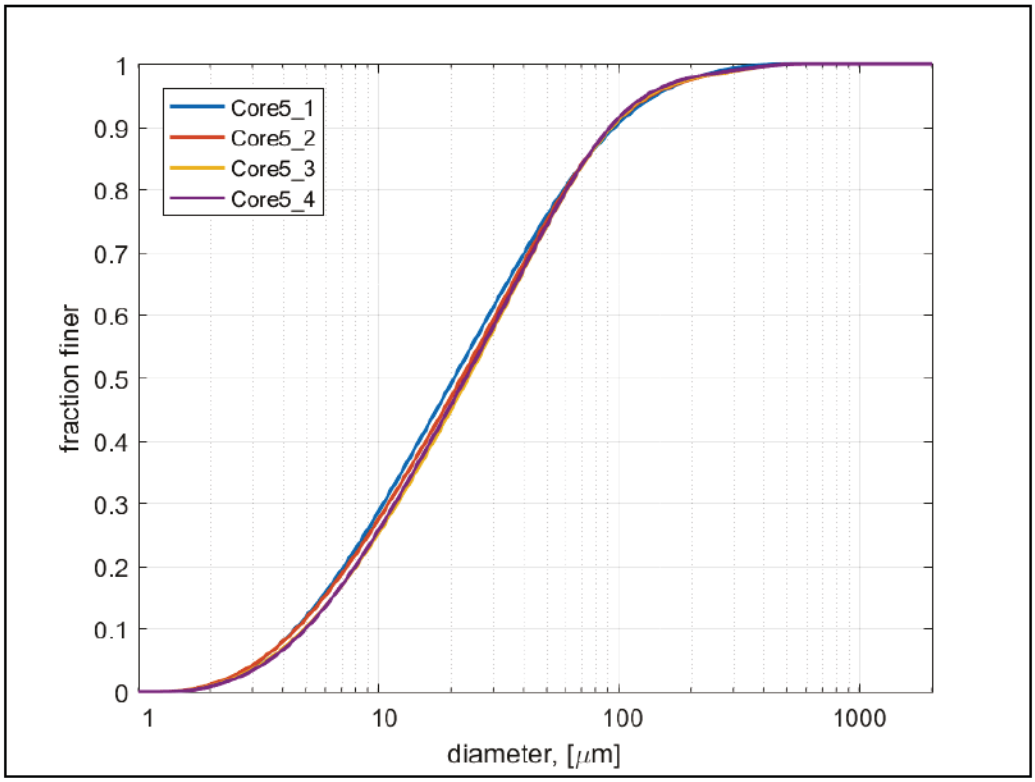

Figure A-5b. Grain size distributions for Core 5b physical samples.

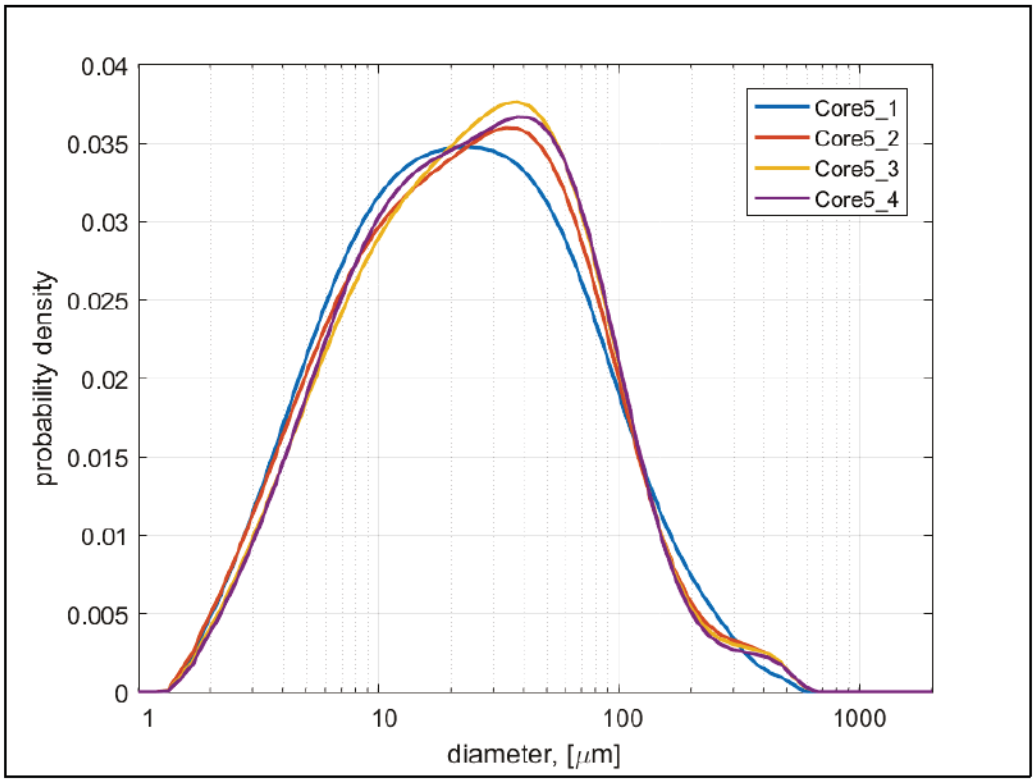

Figure A-5c. Erosion rate at a given applied stress versus depth down core (left). Class fractions and bulk density of physical samples (right) for Core 5b.

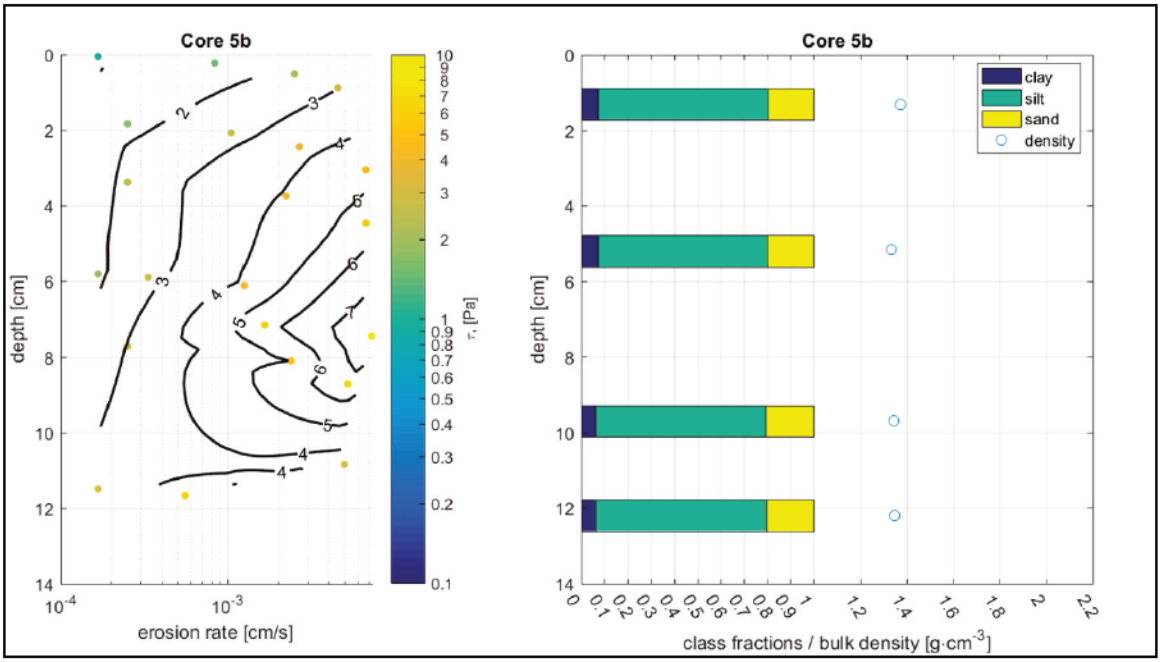

Figure A-5d. Erosion rate versus applied stress and resulting power law fit (s) for Core 5b. Symbol color corresponds to depth down core.

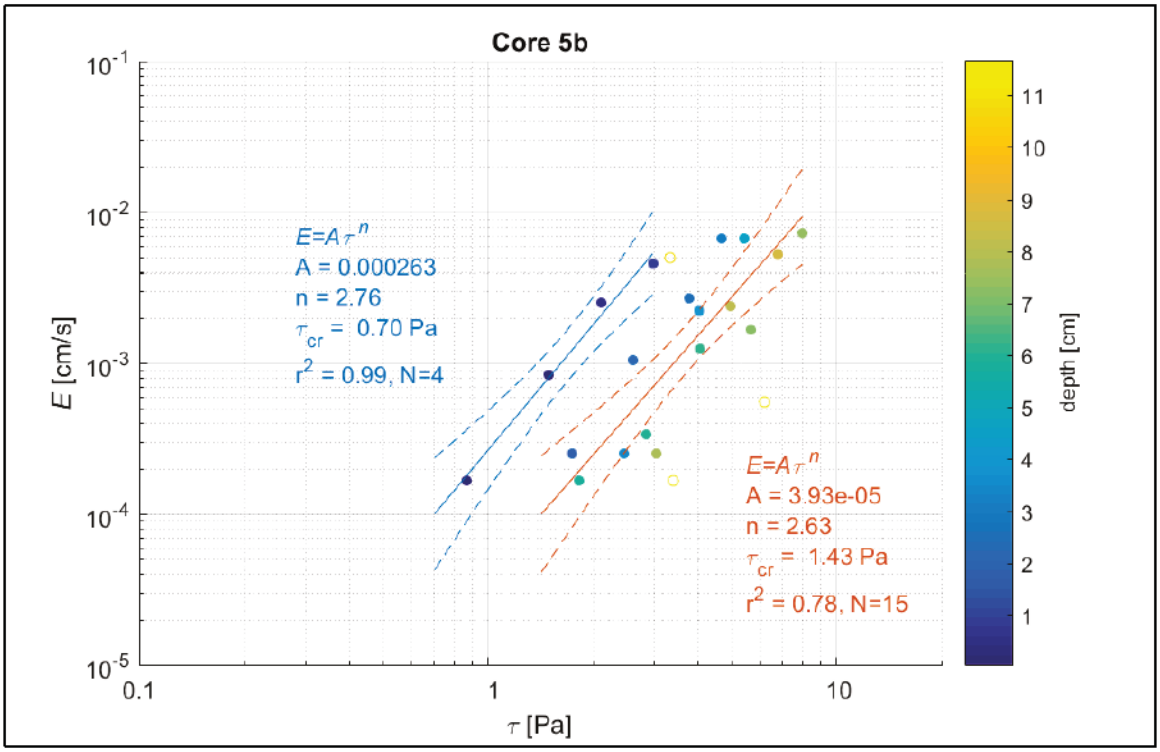

Table A-6a. Core description, Core 6.

Photograph	Description
	Overlying water. Sediment is brown in color within the upper 0.5 cm. Sediment color transitions to dark gray. Large gas pocket/void visible at ~ 13 cm below the surface, measuring 1 × 5 cm. A few laminae are visible. One prominent at approximately 15 cm below the surface.

Table A-6b. Core surface photographs, station Core 6.

Sample 1

Sample 2

Sample 3

Sample 4

Table A-6c. Descriptions of the grain size distributions of physical samples, Core 6.

Sample	Depth [cm]	d10 [µm]	d50 [µm]	d90 [µm]	Fraction Clay	Fraction Silt	Fraction Sand
Core6_1	0.9	3.89	40.67	425.33	0.10	0.43	0.46
Core6_2	2.1	2.50	7.64	53.82	0.25	0.66	0.09
Core6_3	6.4	2.59	8.75	51.98	0.23	0.70	0.08
Core6_4	12.7	2.57	7.78	42.29	0.24	0.70	0.06

Figure A-6a. Cumulative grain size distributions for Core 6 physical samples.

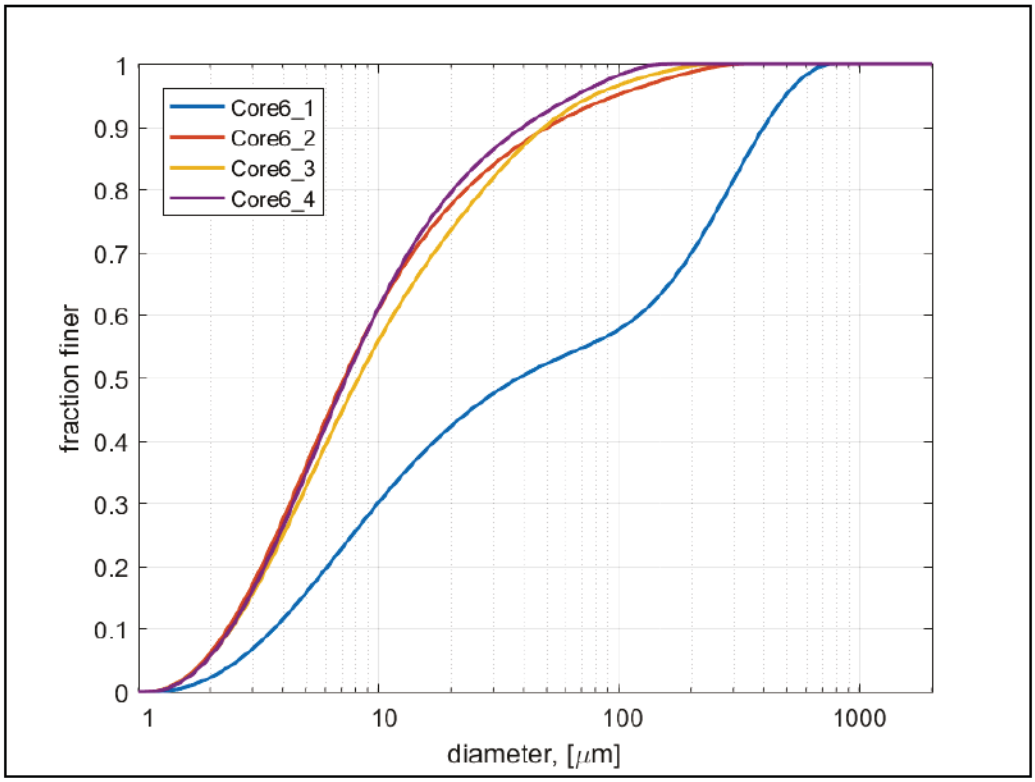

Figure A-6b. Grain size distributions for Core 6 physical samples.

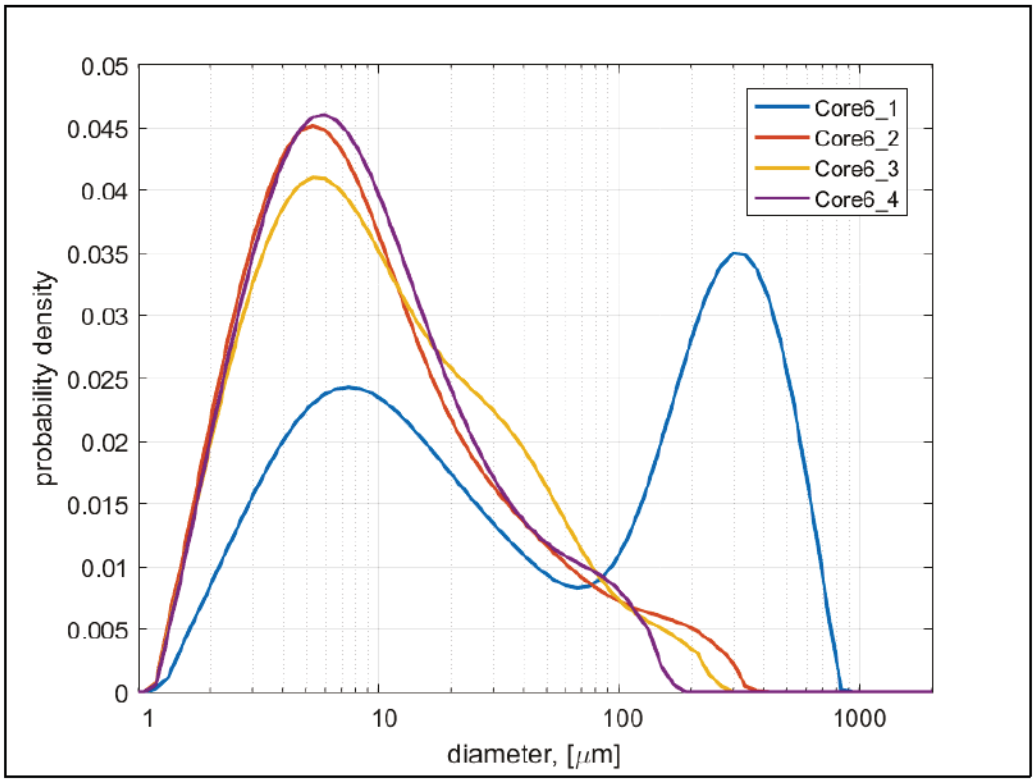

Figure A-6c. Erosion rate at a given applied stress versus depth down core (left). Class fractions and bulk density of physical samples (right) for Core 6.

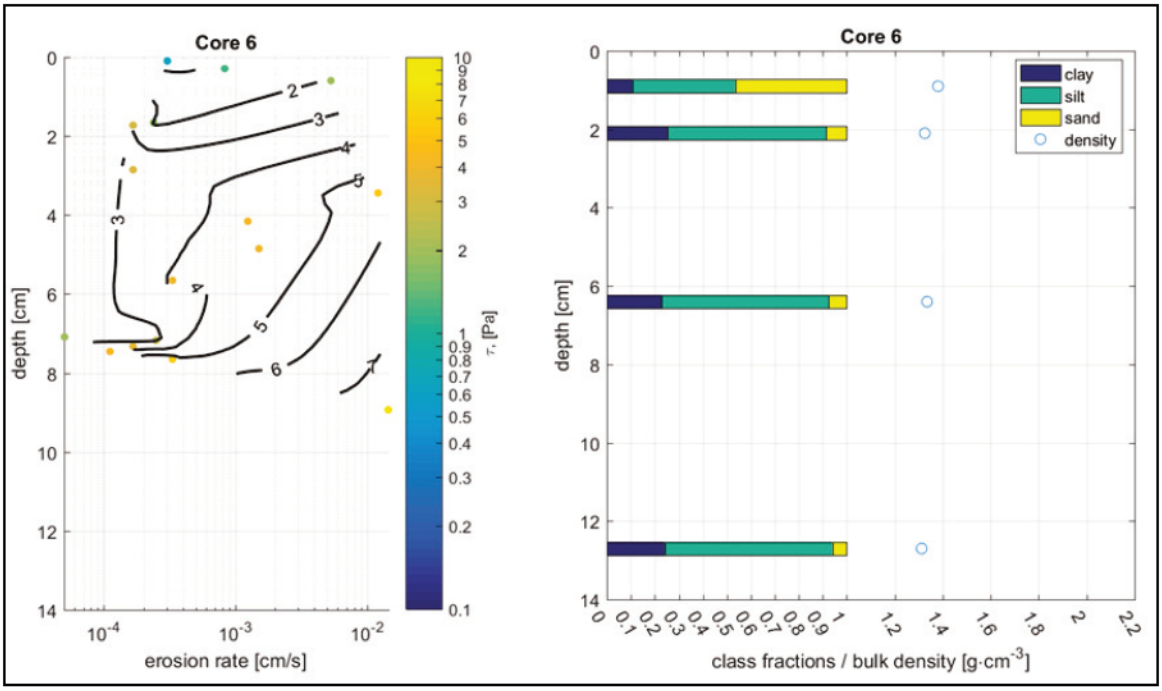

Figure A-6d. Erosion rate versus applied stress and resulting power law fit (s) for Core 6. Symbol color corresponds to depth down core.

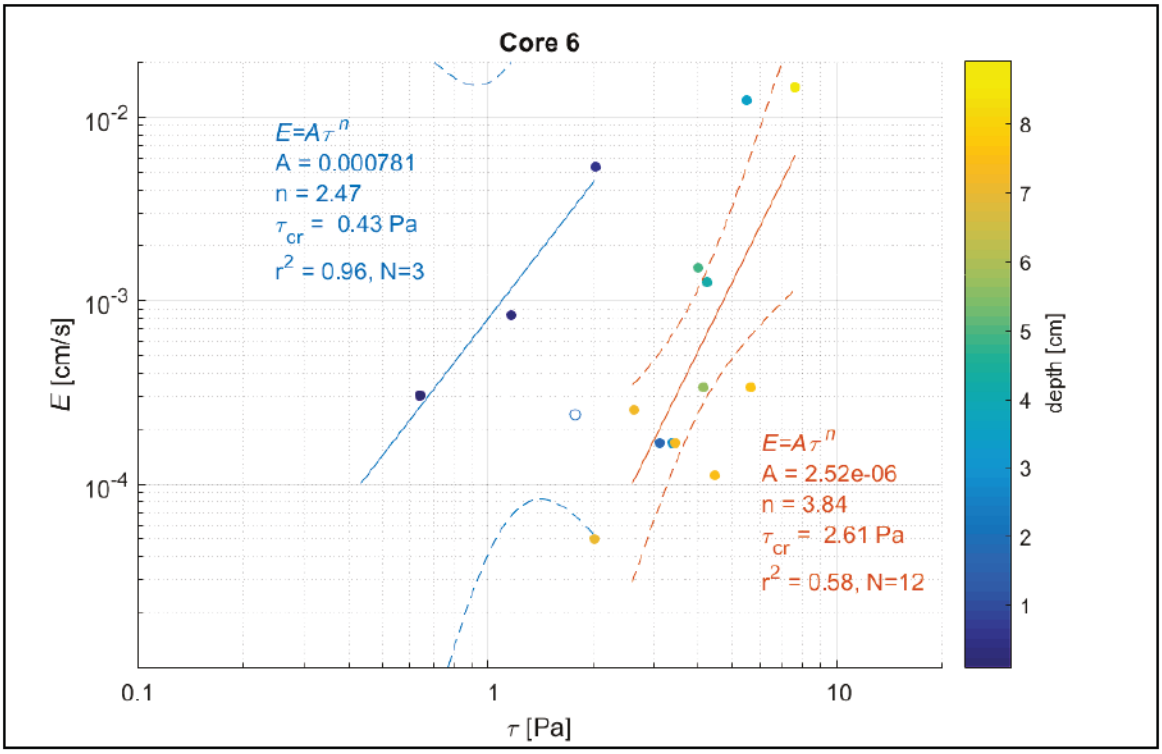

Table A-7a. Core description, Core 7.

Photograph	Description
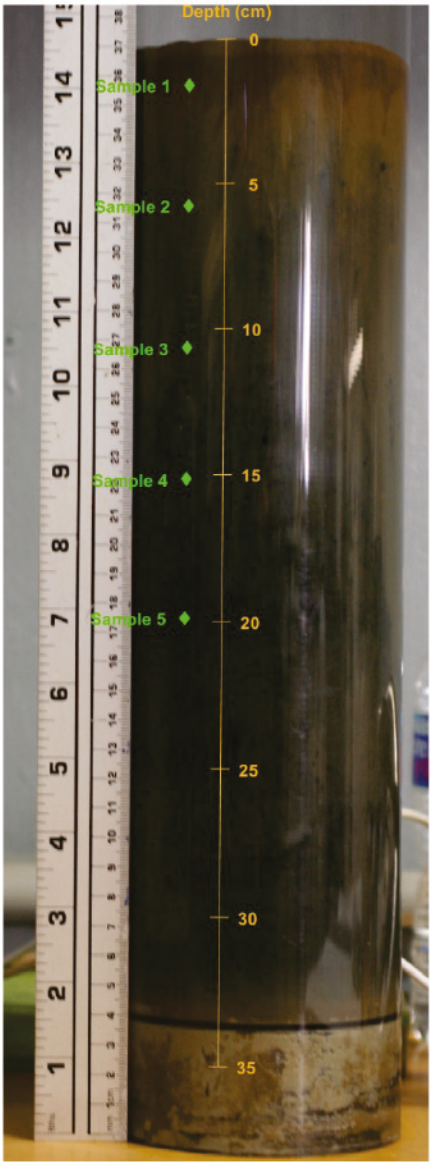	Overlying water. Level core surface composed of fine, light brown sediment. Sediment color transitions to darker grey within 1–2 cm of core surface. Visual evidence of bioturbation to ~10 cm depth. No other visible voids or fractures.

Table A-7b. Core surface photographs, Core 7.

Sample 1 	Sample 2 
Sample 3 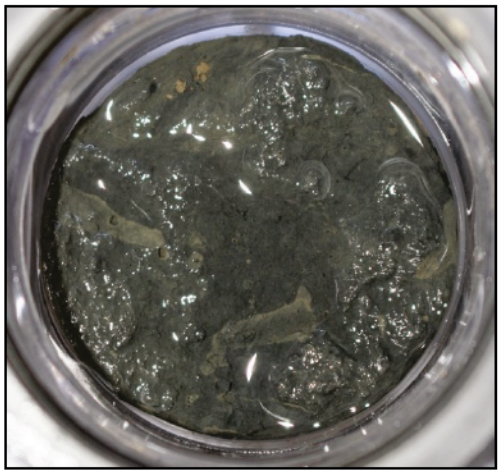	Sample 4 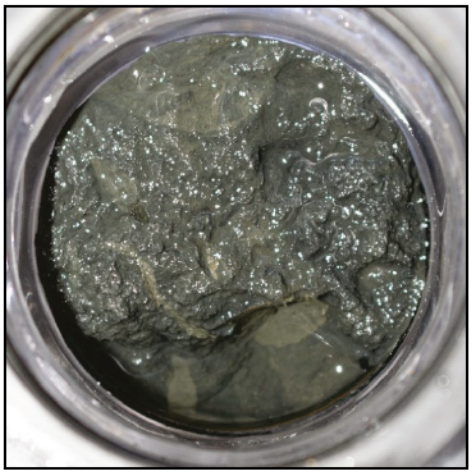
Sample 5 	

Table A-7c. Descriptions of the grain size distributions of physical samples, Core 7.

Sample	Depth [cm]	d10 [µm]	d50 [µm]	d90 [µm]	Fraction Clay	Fraction Silt	Fraction Sand
Core7_1	1.6	3.93	14.35	76.46	0.10	0.76	0.13
Core7_2	5.8	3.73	12.17	55.28	0.12	0.80	0.08
Core7_3	10.7	3.58	12.55	56.00	0.13	0.79	0.08
Core7_4	15.2	3.64	12.19	54.26	0.12	0.80	0.08
Core7_5	19.9	3.88	12.38	50.39	0.11	0.82	0.07

Figure A-7a. Cumulative grain size distributions for Core 7 physical samples.

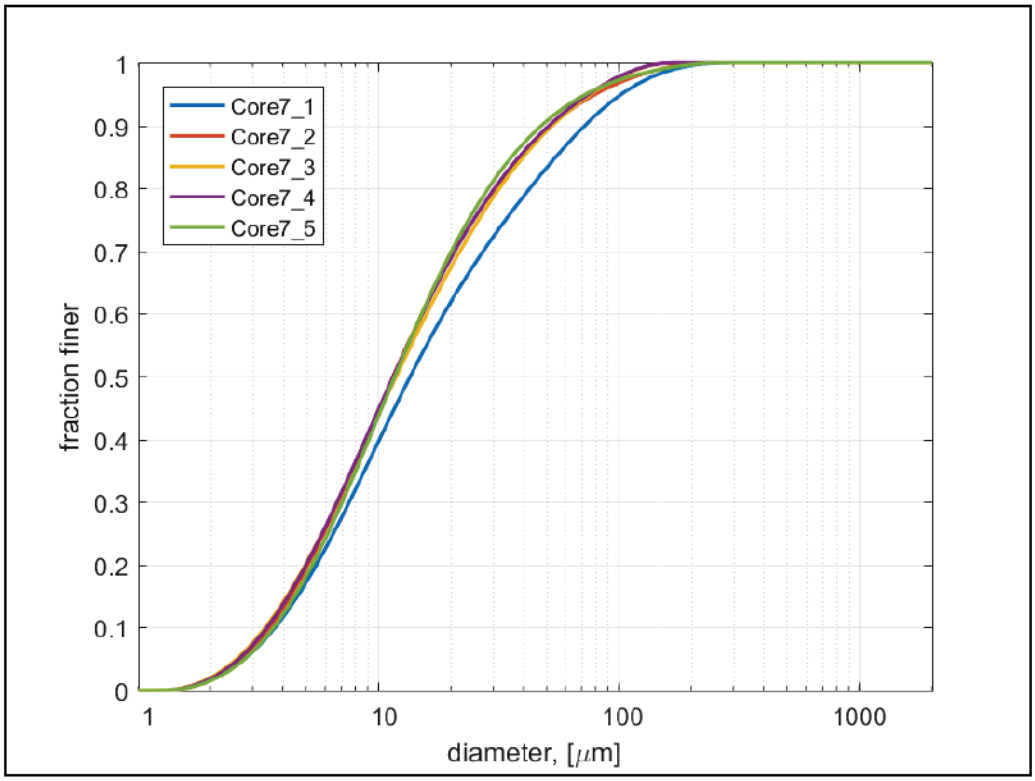

Figure A-7b. Grain size distributions for Core 7 physical samples.

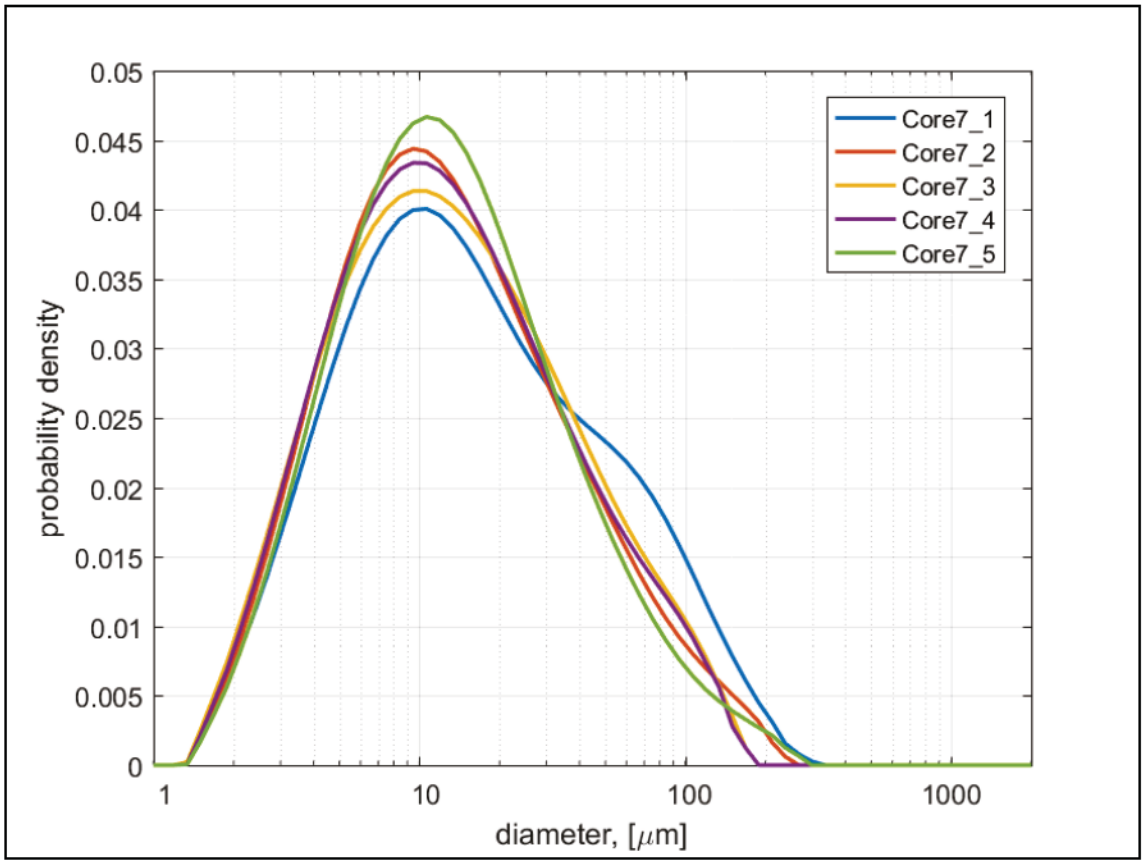

Figure A-7c. Erosion rate at a given applied stress versus depth down core (left). Class fractions and bulk density of physical samples (right) for Core 7.

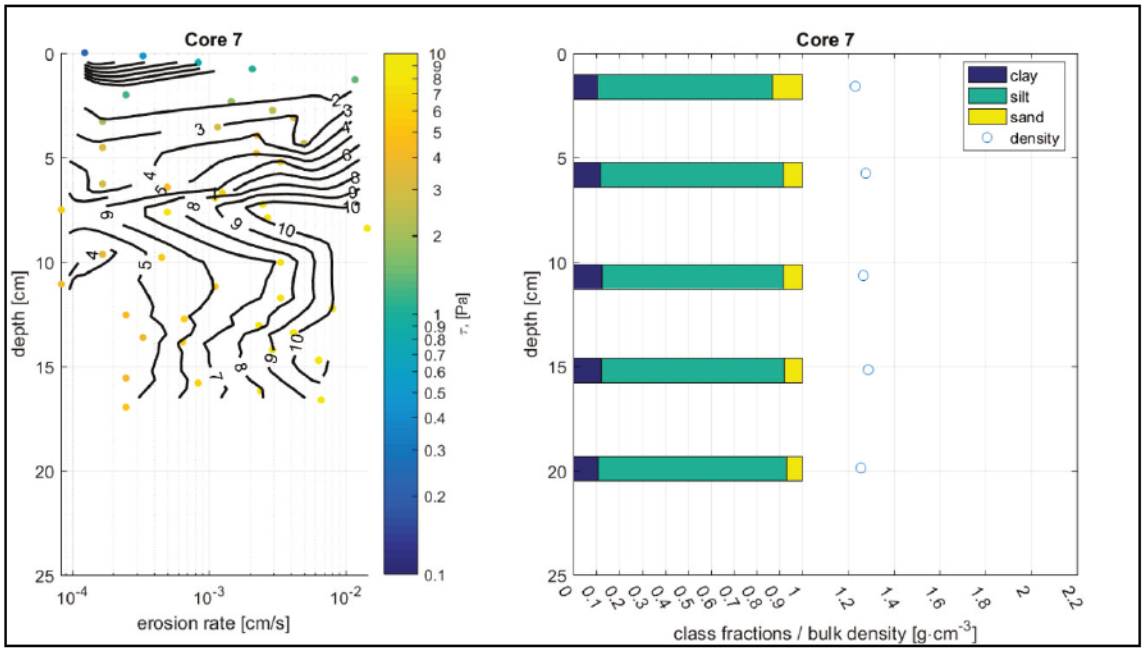

Figure A-7d. Erosion rate versus applied stress and resulting power law fit (s) for Core 7. Symbol color corresponds to depth down core.

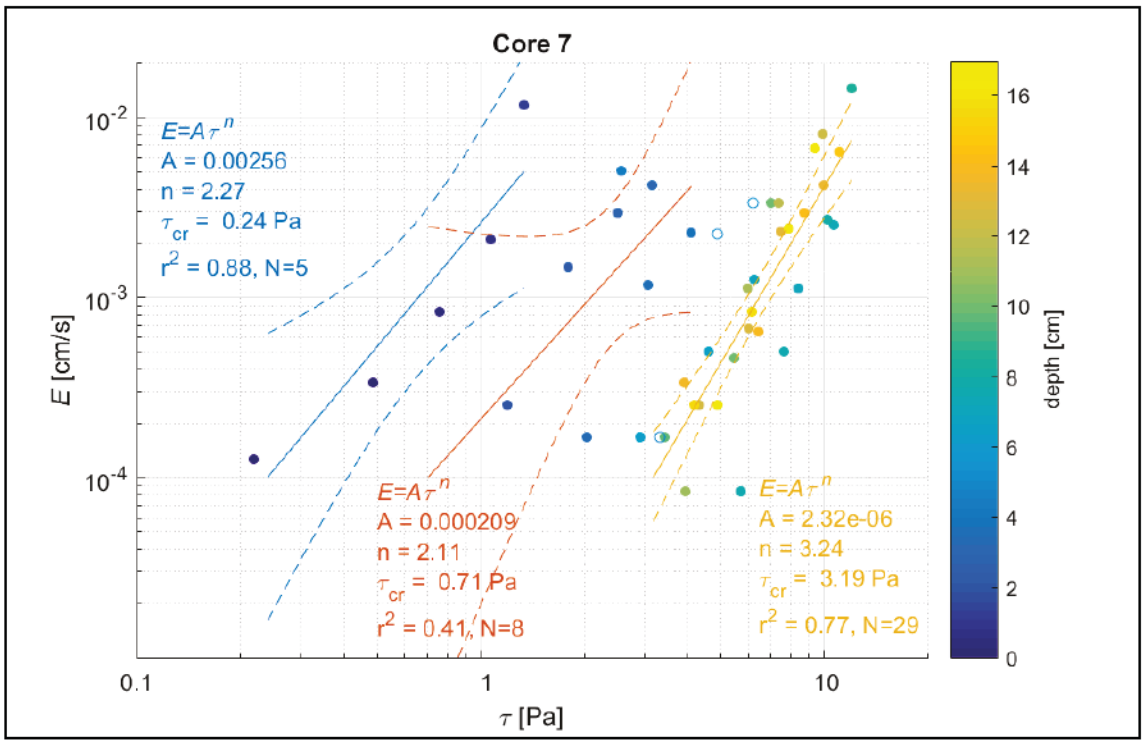

Table A-8a. Core description, Core 8.

Photograph	Description
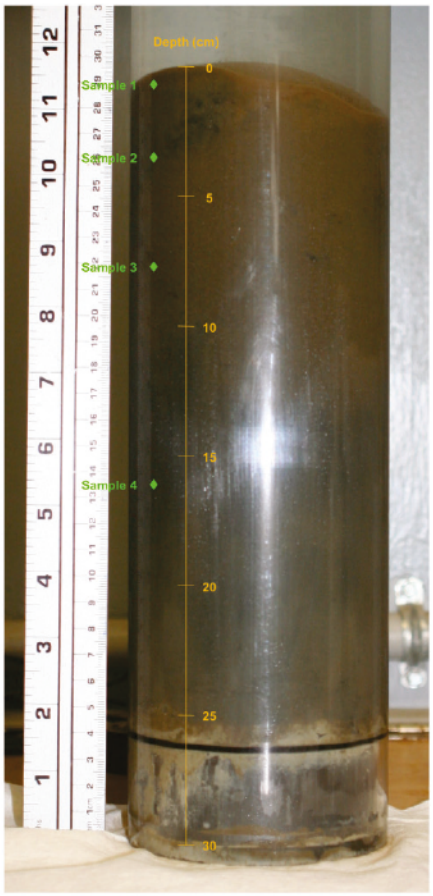	Overlying water. Fairly level core surface, only ~ 1 cm of variation, composed of what appears to be fine flocs. Upper 2 mm of sediment is chestnut brown in color, which then transitions to a darker brown color. Sediment transitions to a darker gray color below ~15 cm.

Table A-8b. Core surface photographs, Core 8.

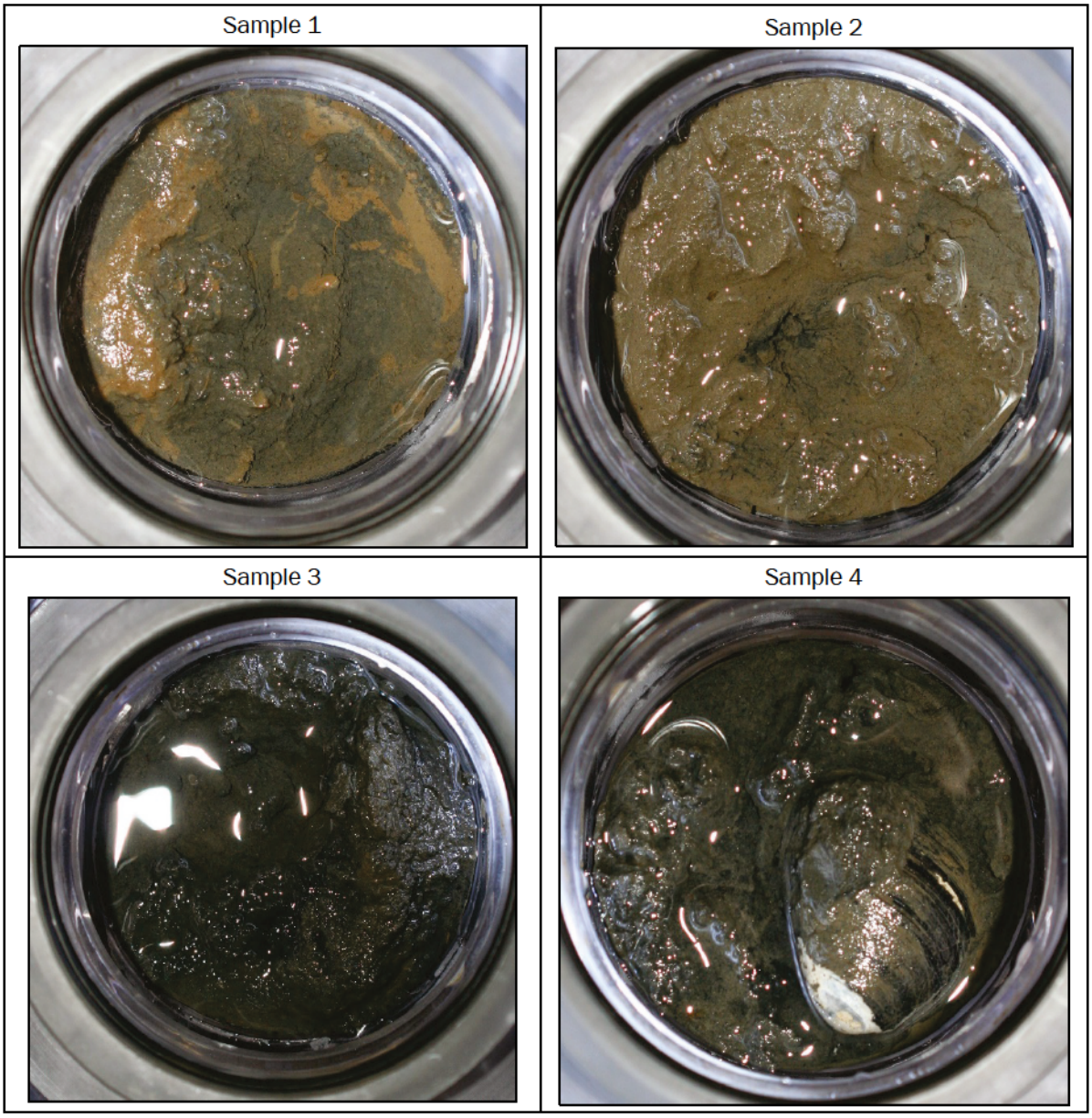

Table A-8c. Descriptions of the grain size distributions of physical samples, Core 8.

Sample	Depth [cm]	d10 [µm]	d50 [µm]	d90 [µm]	Fraction Clay	Fraction Silt	Fraction Sand
Core8_1	0.7	3.70	13.48	69.17	0.12	0.77	0.11
Core8_2	3.5	3.91	14.87	107.34	0.10	0.73	0.17
Core8_3	7.7	4.42	17.44	118.71	0.08	0.69	0.23
Core8_4	16.1	5.97	129.87	342.36	0.05	0.32	0.62

Figure A-8a. Cumulative grain size distributions for Core 8 physical samples.

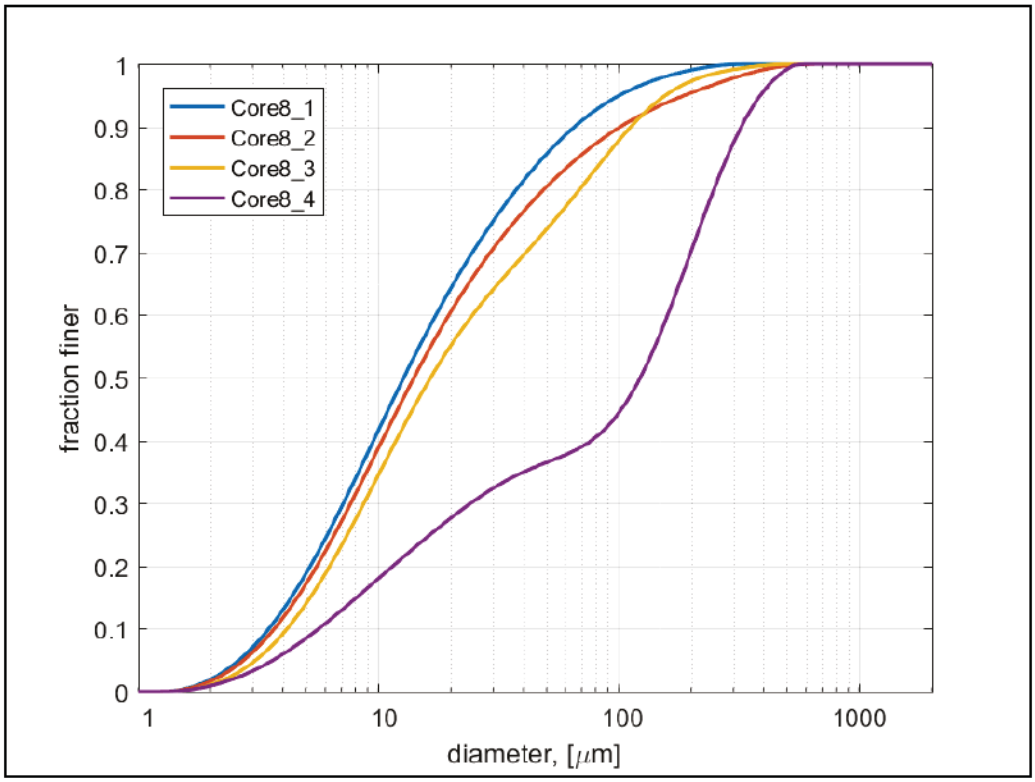

Figure A-8b. Grain size distributions for Core 8 physical samples.

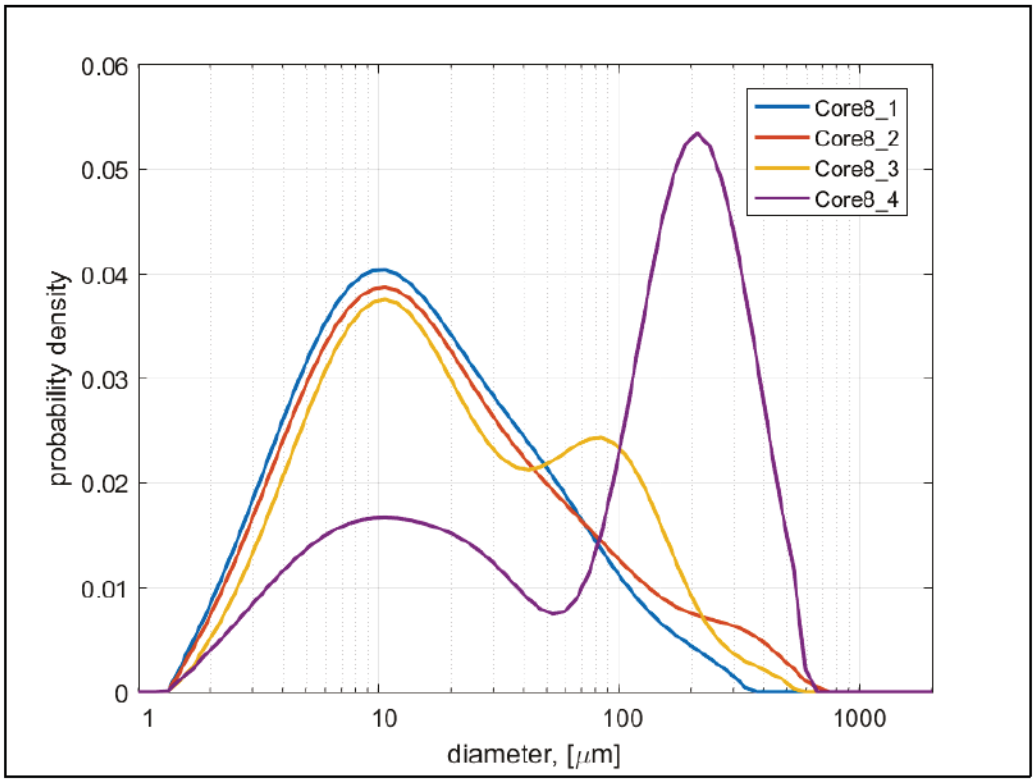

Figure A-8c. Erosion rate at a given applied stress versus depth down core (left). Class fractions and bulk density of physical samples (right) for Core 8.

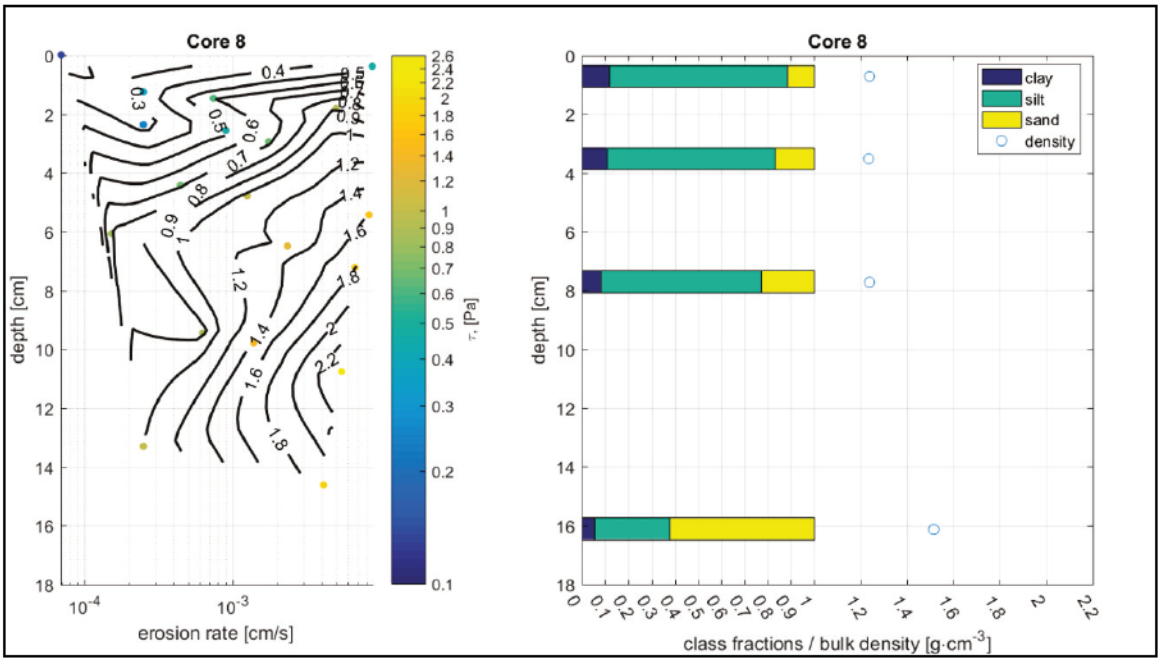

Figure A-8d. Erosion rate versus applied stress and resulting power law fit (s) for Core 8. Symbol color corresponds to depth down core.

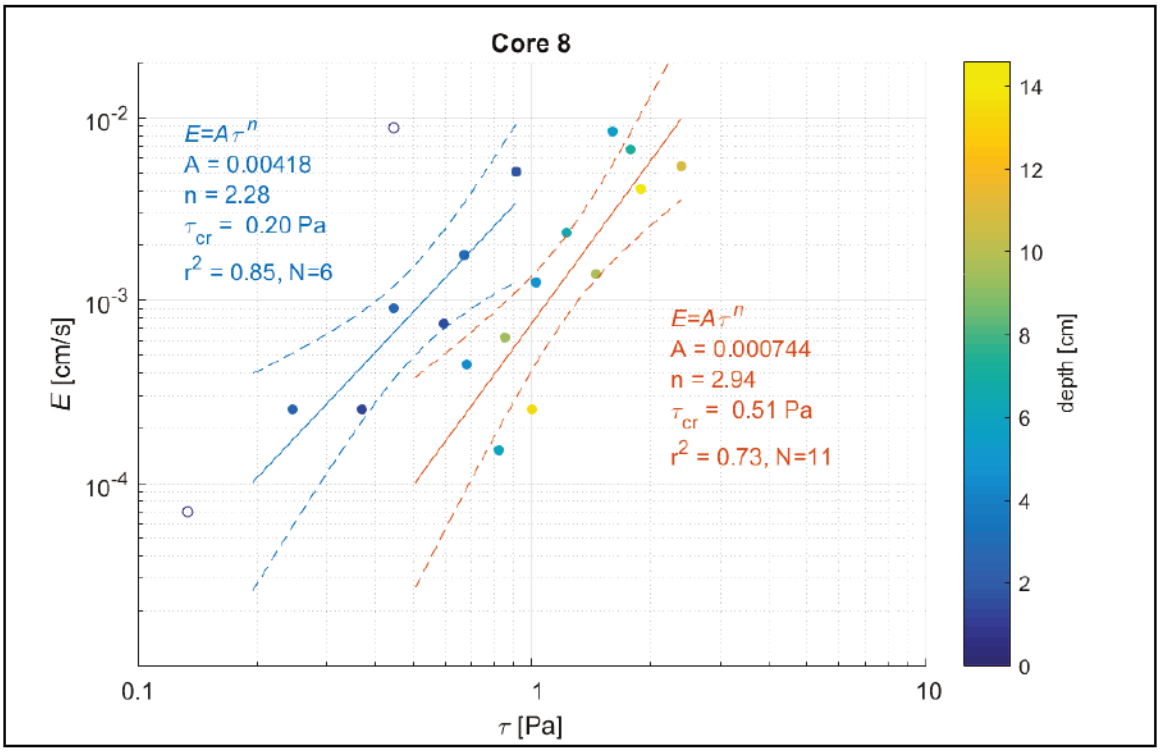

Table A-9a. Core description, Core 9b.

Photograph	Description
	Overlying water.
	Fairly level surface. Core appears sandy with mixed fines. No visible layering, but sediment appears to get darker with depth. A few voids evident at core wall, ~0.5–1.5 cm in diameter.

Table A-9b. Core surface photographs, station Core 9b.

Sample 1	Sample 2
	

Table A-9c. Descriptions of the grain size distributions of physical samples, Core 9b.

Sample	Depth [cm]	d10 [µm]	d50 [µm]	d90 [µm]	Fraction Clay	Fraction Silt	Fraction Sand
Core9_1	0.7	25.85	172.13	343.74	0.02	0.14	0.84
Core9_2	4	101.34	219.72	389.34	0.01	0.06	0.93

Figure A-9a. Cumulative grain size distributions for Core 9b physical samples.

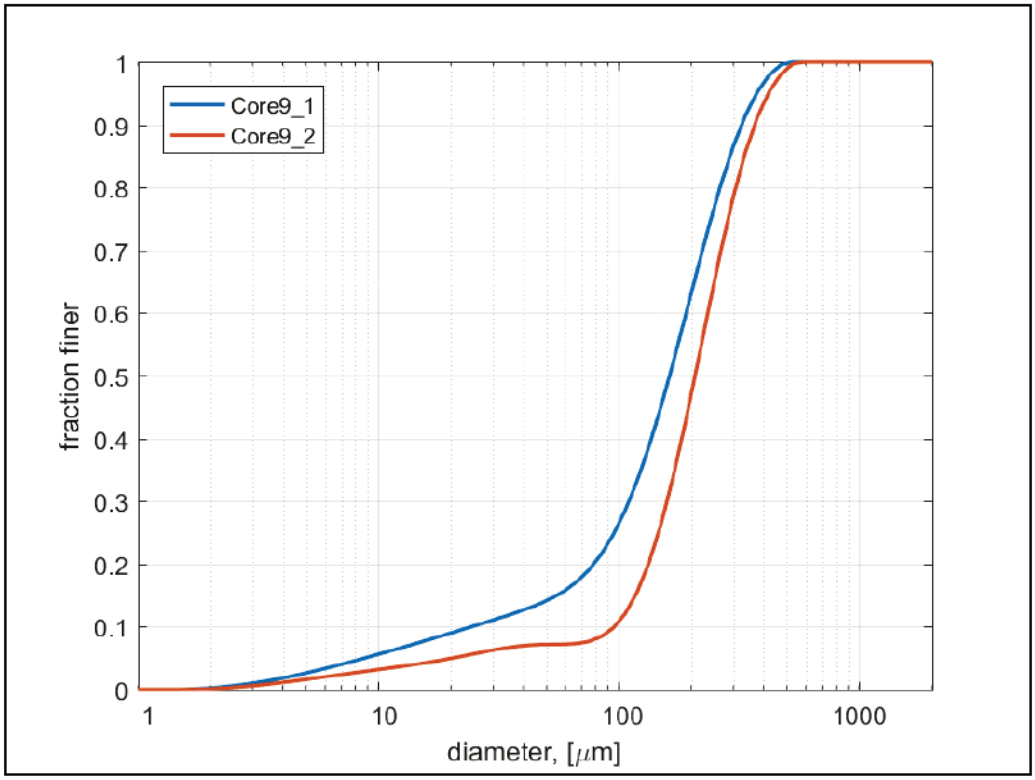

Figure A-9b. Grain size distributions for Core 9b physical samples.

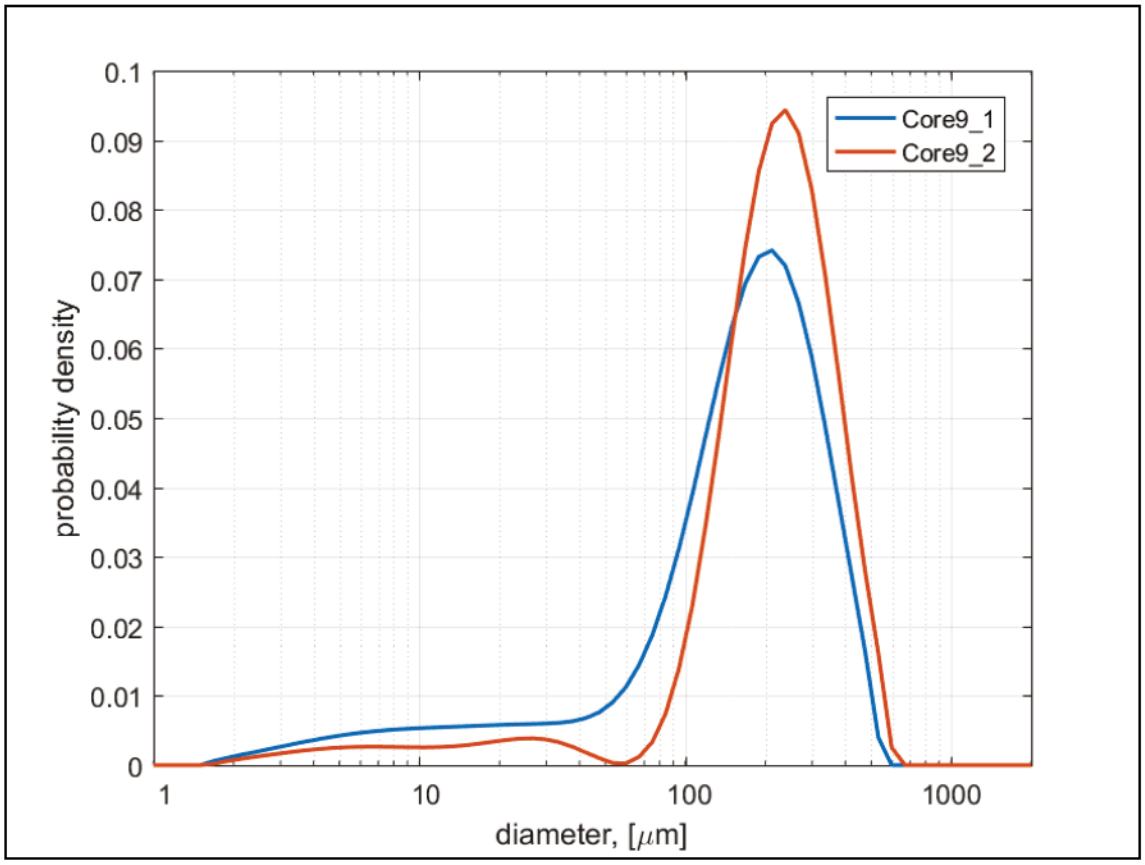

Figure A-9c. Erosion rate at a given applied stress versus depth down core (left). Class fractions and bulk density of physical samples (right) for Core 9b.

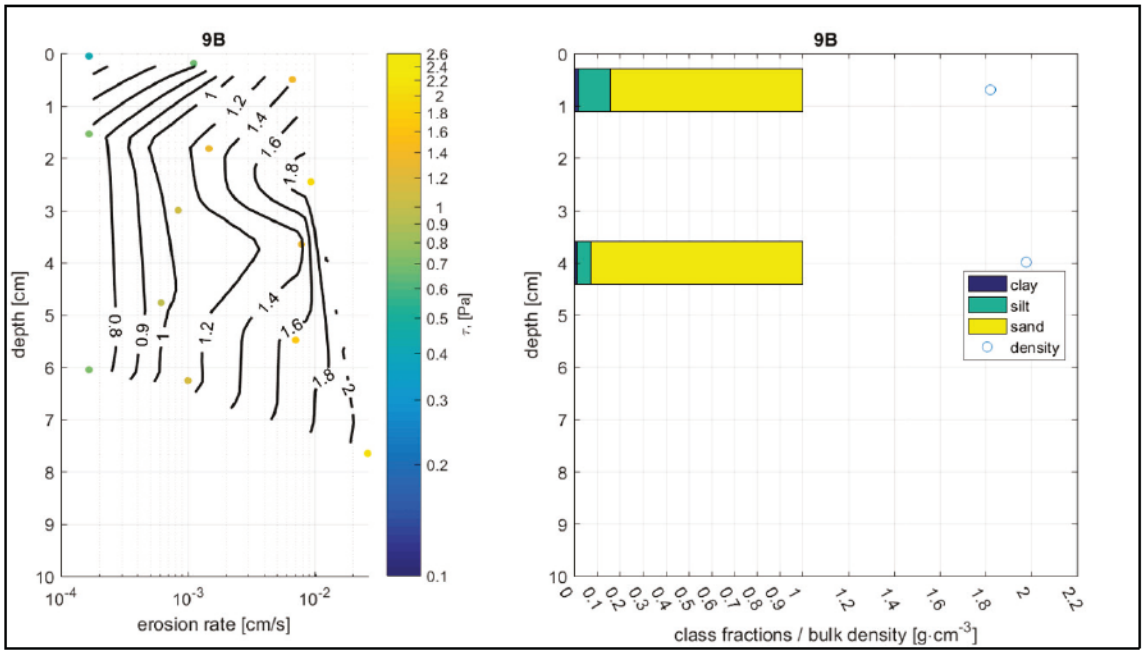

Figure A-9d. Erosion rate versus applied stress and resulting power law fit (s) for Core 9b. Symbol color corresponds to depth down core.

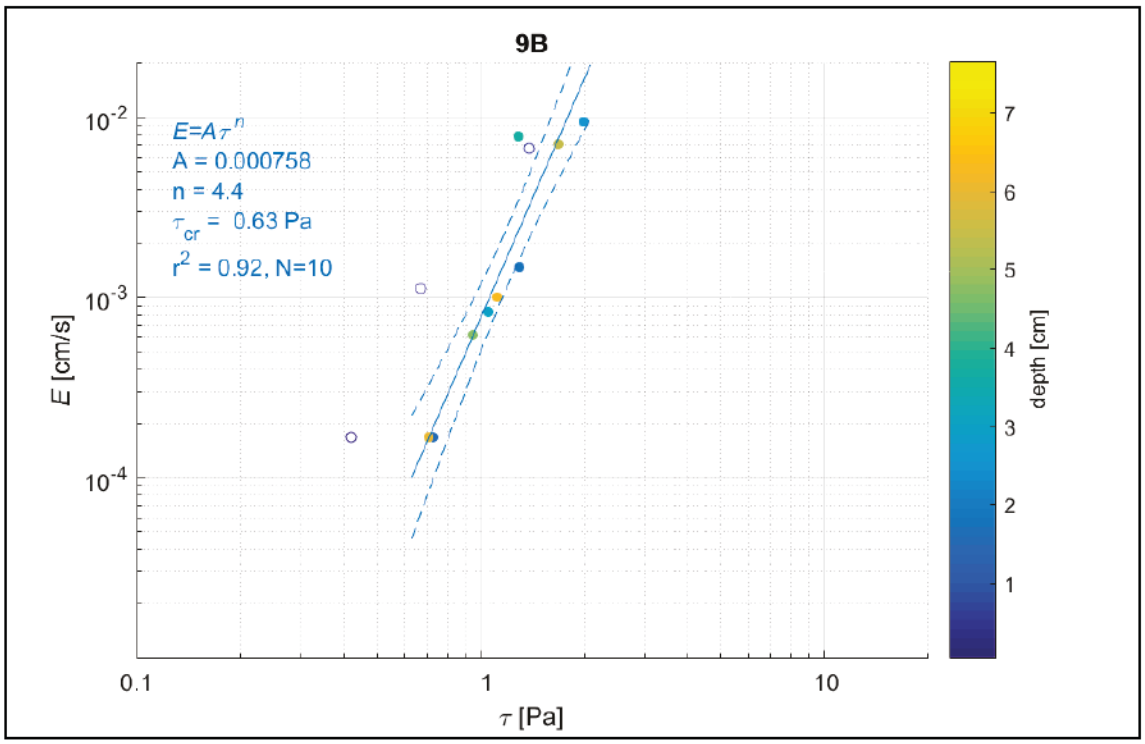

Table A-10a. Core description, Core 10.

Photograph	Description
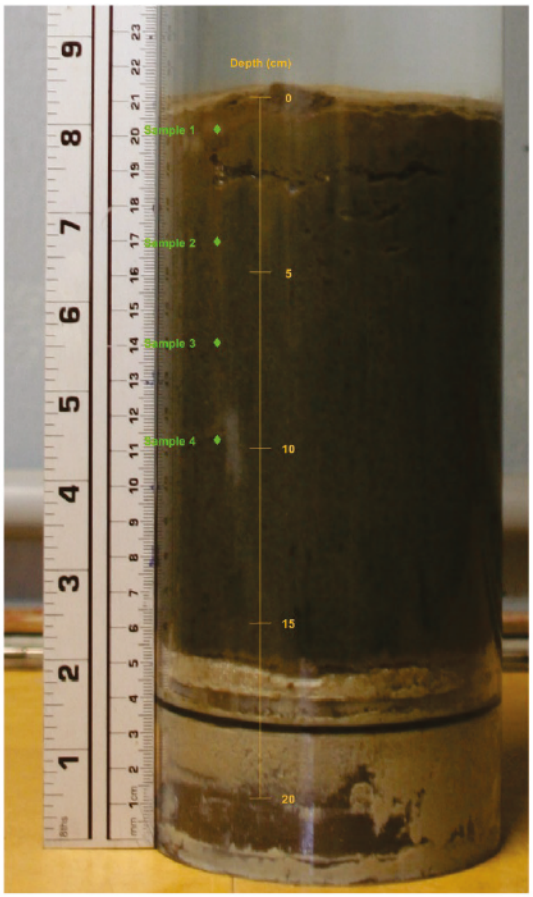	Overlying water. Smooth, flat core surface composed of fine, light brown sediment. Sediment color transitions to grey sandy material 1–2 cm below surface. This texture is consistent to the bottom of the core. Several horizontal voids visible ~ 2–5 cm below the core surface.

Table A-10b. Core surface photographs, Core 10.

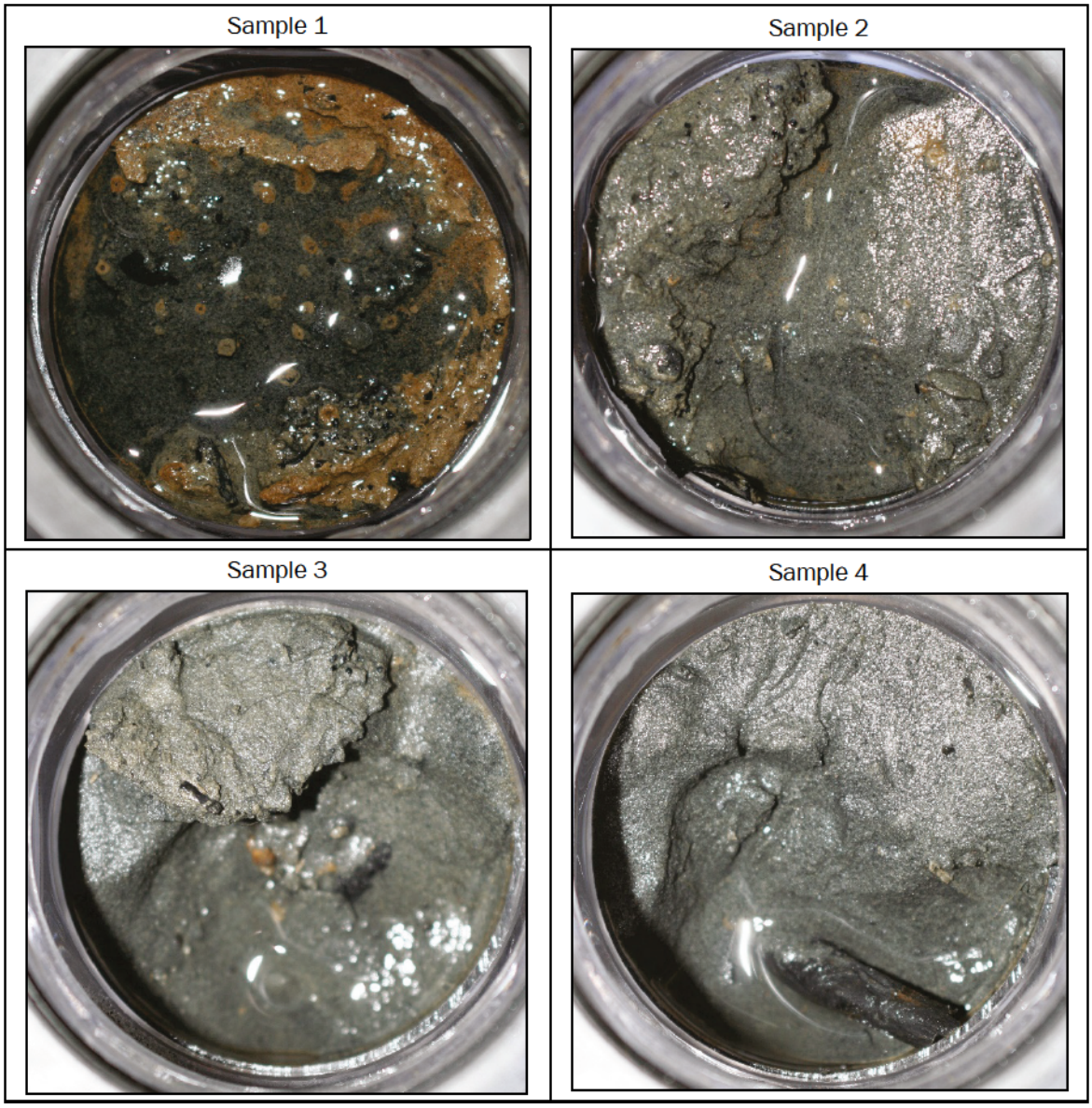

Table A-10c. Descriptions of the grain size distributions of physical samples, Core 10.

Sample	Depth [cm]	d10 [µm]	d50 [µm]	d90 [µm]	Fraction Clay	Fraction Silt	Fraction Sand
Core10_1	0.9	8.87	146.47	352.34	0.03	0.31	0.66
Core10_2	4.1	8.86	168.52	352.24	0.03	0.27	0.70
Core10_3	7	11.59	188.07	368.18	0.02	0.20	0.78
Core10_4	9.8	147.43	244.70	411.00	0.00	0.00	1.00

Figure A-10a. Cumulative grain size distributions Core 10 physical samples.

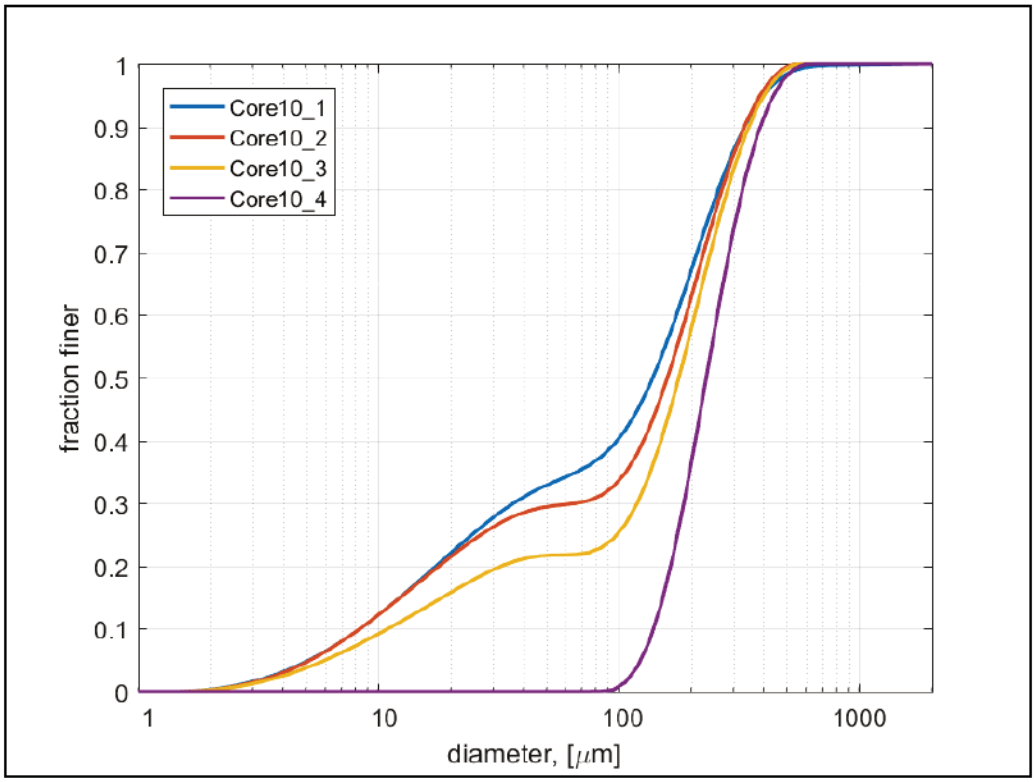

Figure A-10b. Grain size distributions for Core 10 physical samples.

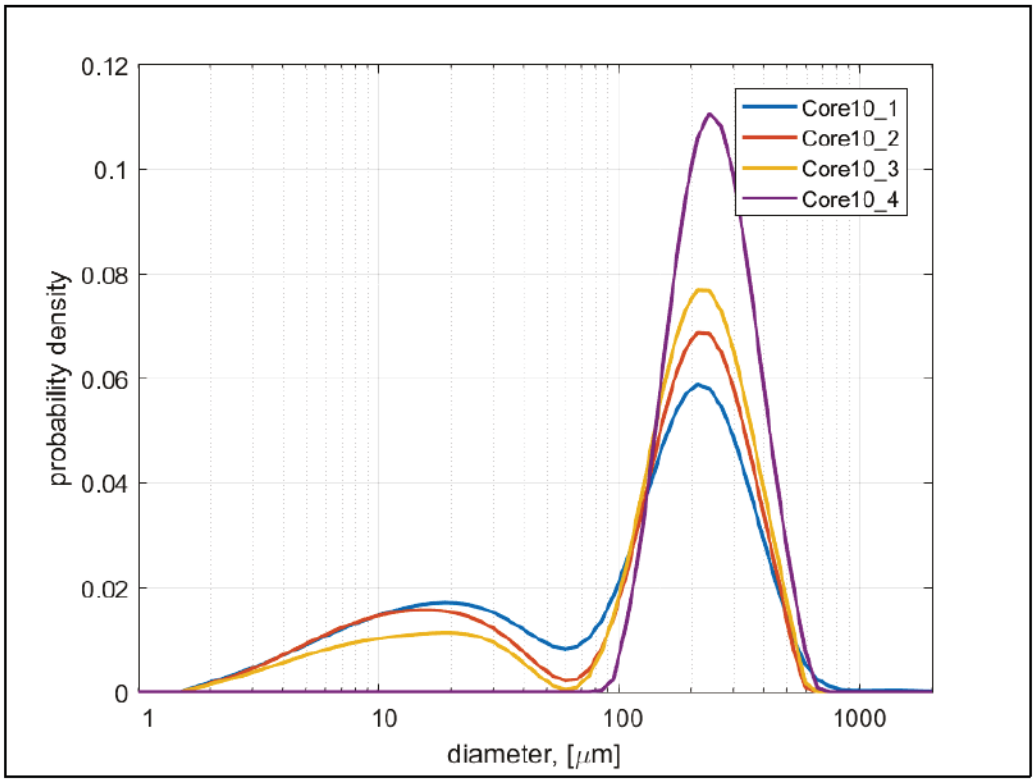

Figure A-10c. Erosion rate at a given applied stress versus depth down core (left). Class fractions and bulk density of physical samples (right) for Core 10.

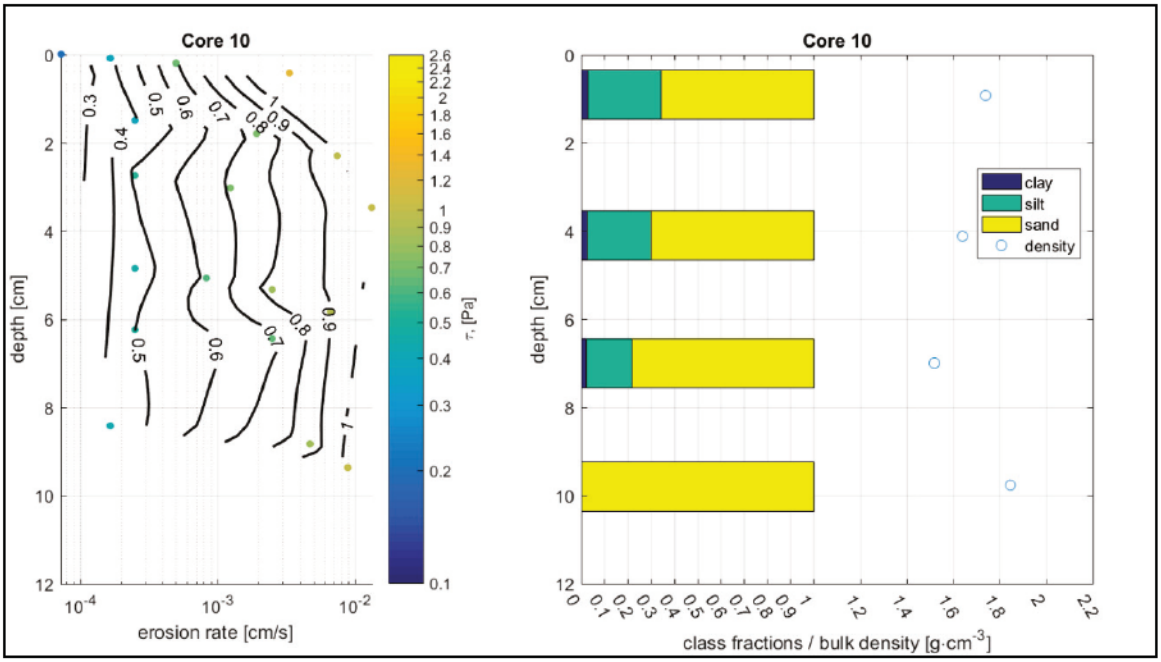

Figure A-10d. Erosion rate versus applied stress and resulting power law fit (s) for Core 10. Symbol color corresponds to depth down core.

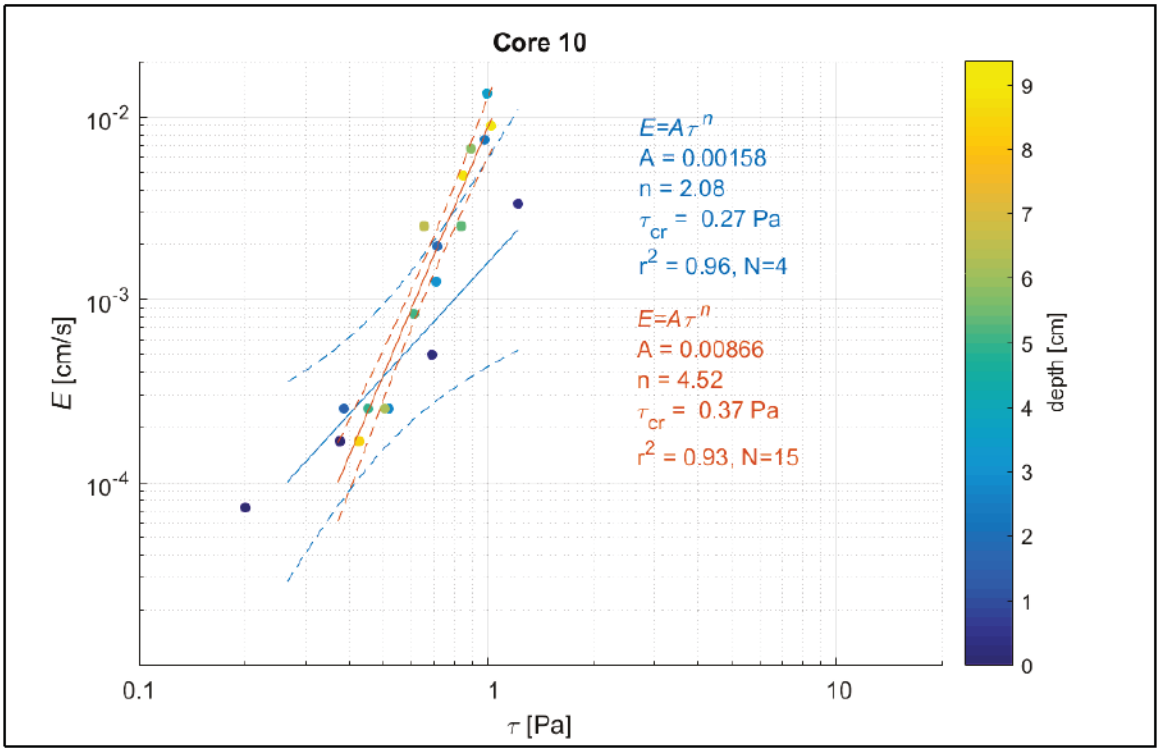

Table A-11a. Core description, Core 11.

Photograph	Description
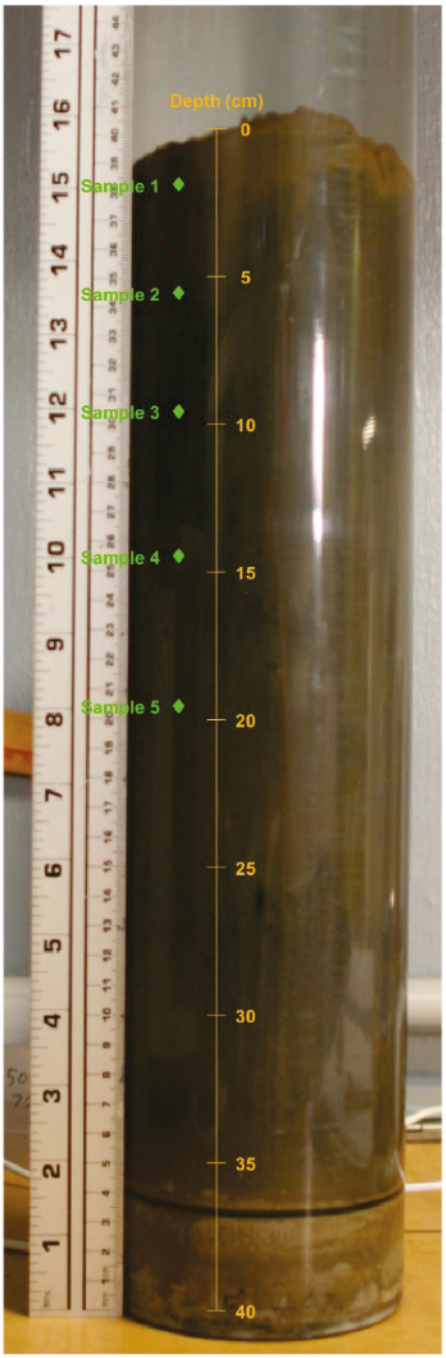	Overlying water. Sloped surface with lose mud aggregates, ~ 1 cm in diameter and light brown in color. Sediment transitions to darker gray in color throughout the remainder of the core. No visible voids or fissures.

Table A-11b. Core surface photographs, Core 11.

Sample 1

Sample 2

Sample 3

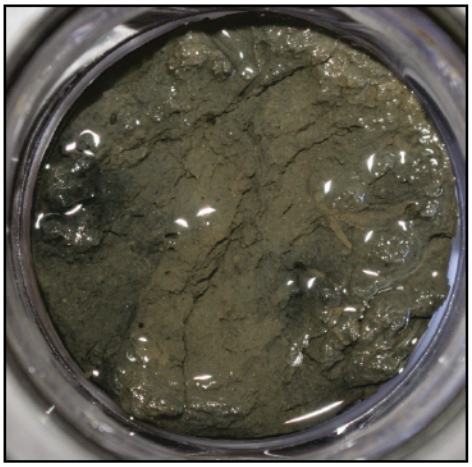

Sample 4

Sample 5

Table A-11c. Descriptions of the grain size distributions of physical samples, Core 11.

Sample	Depth [cm]	d10 [µm]	d50 [µm]	d90 [µm]	Fraction Clay	Fraction Silt	Fraction Sand
Core11_1	1.9	4.86	14.71	53.74	0.06	0.86	0.07
Core11_2	5.5	4.21	15.52	73.28	0.09	0.79	0.12
Core11_3	9.5	4.15	13.57	58.57	0.09	0.82	0.09
Core11_4	14.4	3.83	13.29	62.26	0.11	0.79	0.10
Core11_5	19.5	4.50	15.33	69.99	0.08	0.81	0.12

Figure A-11a. Cumulative grain size distributions for Core 11 physical samples.

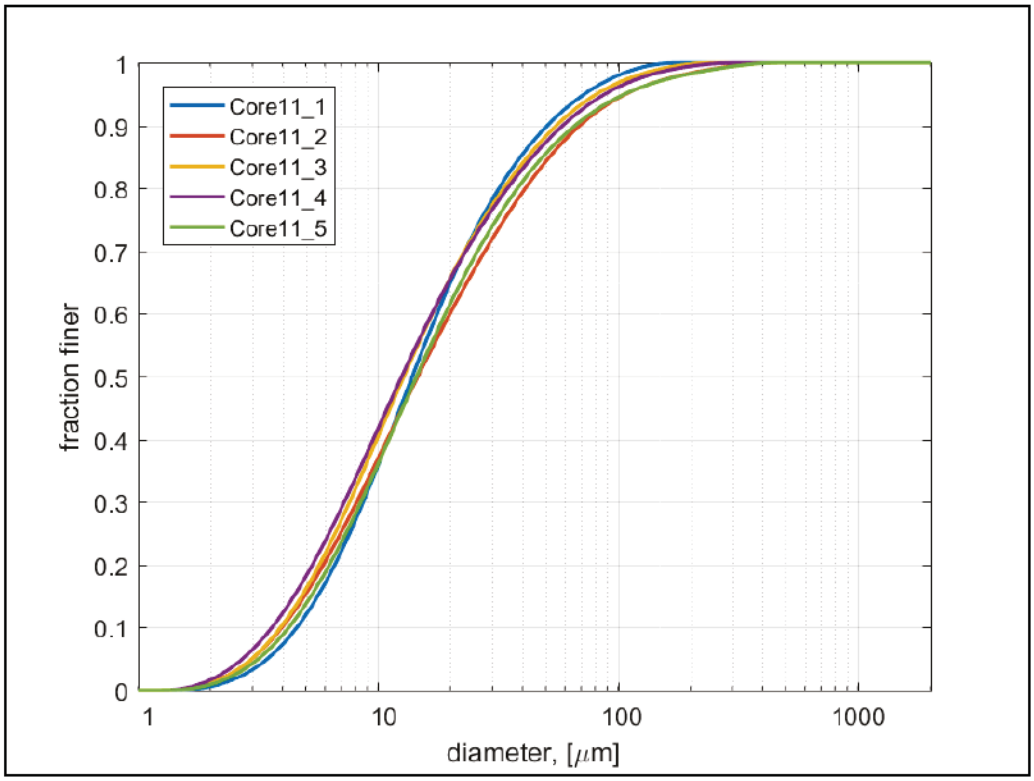

Figure A-11b. Grain size distributions for Core 11 physical samples.

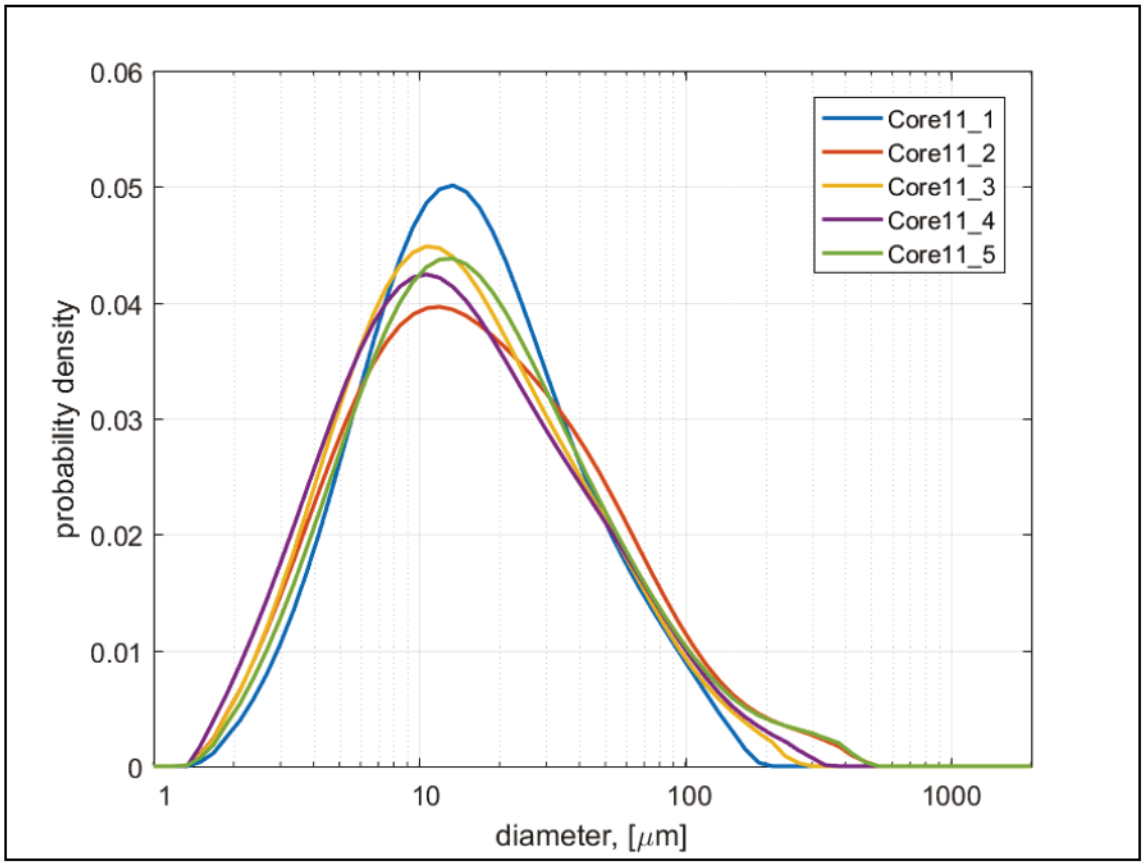

Figure A-11c. Erosion rate at a given applied stress versus depth down core (left). Class fractions and bulk density of physical samples (right) for Core 11.

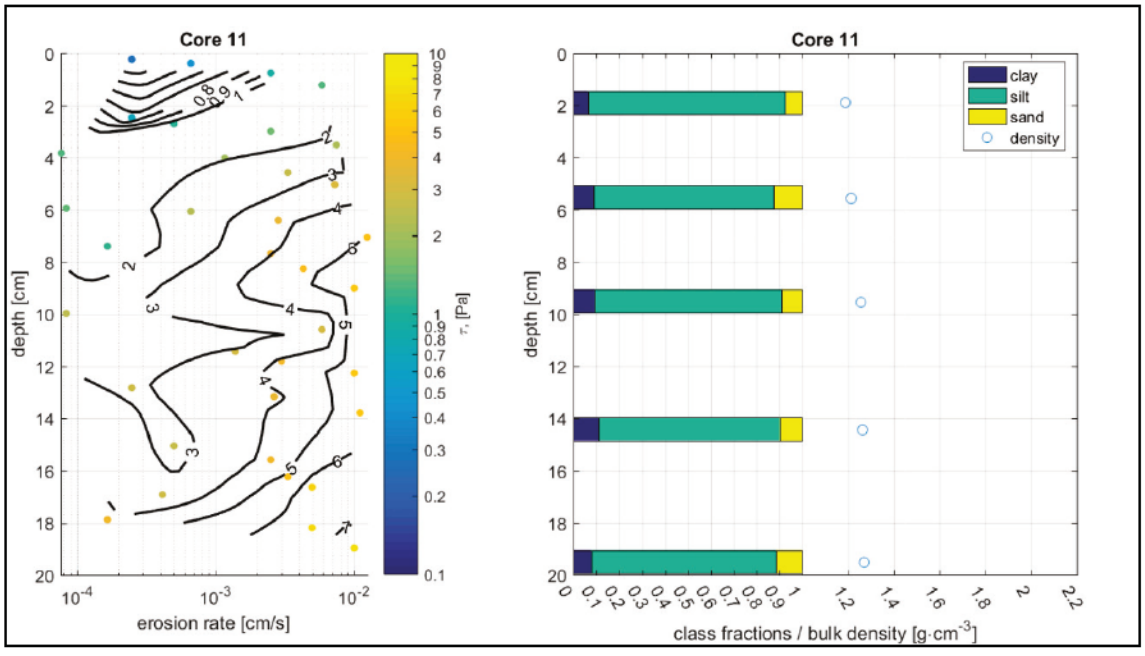

Figure A-11d. Erosion rate versus applied stress and resulting power law fit (s) for Core 11. Symbol color corresponds to depth down core.

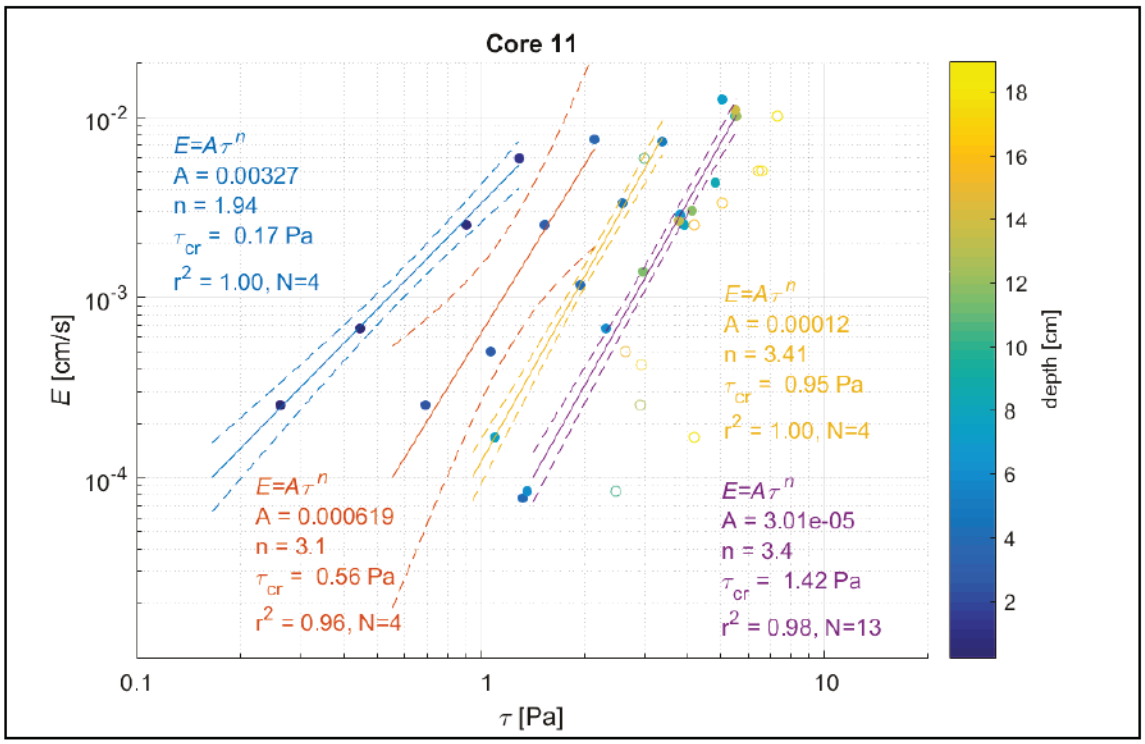

Table A-12a. Core description, Core 12.

Photograph	Description
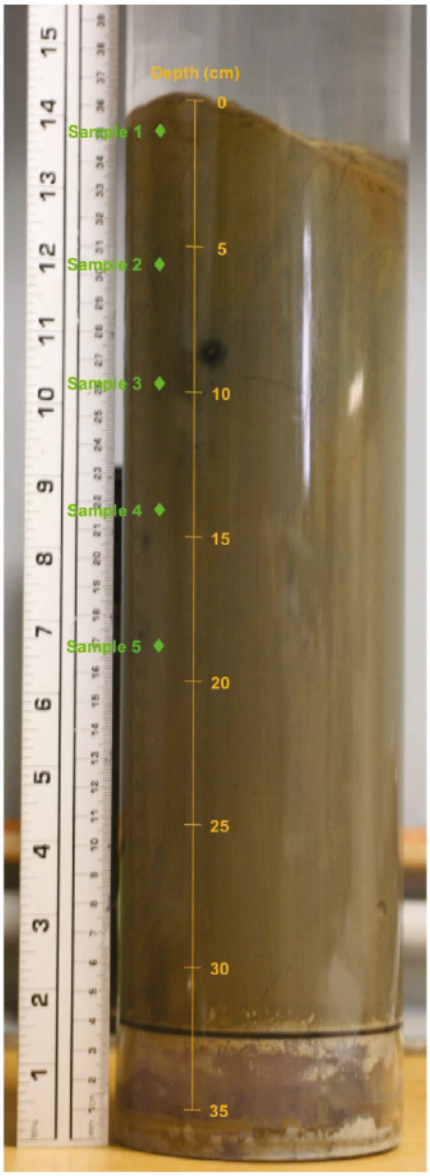	Overlying water. Severely sloped, fine, fluffy, surface composed of light brown sediments. Brownish grey coloration persistent through core below a depth of 0.5 cm. Visible evidence of worm tubes and bioturbation down to a depth of 20 cm.

Table A-12b. Core surface photographs, Core 12.

Sample 1

Sample 2

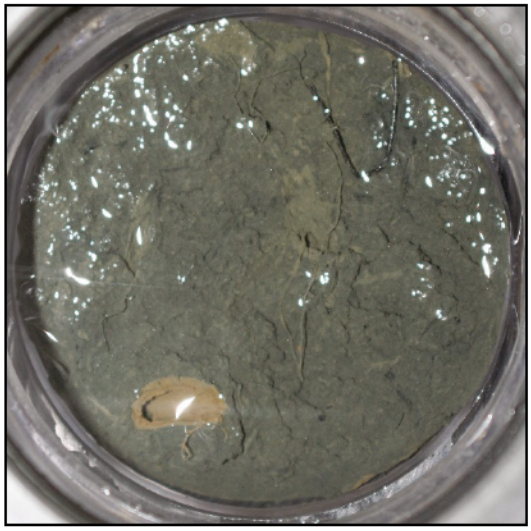

Sample 3

Sample 4

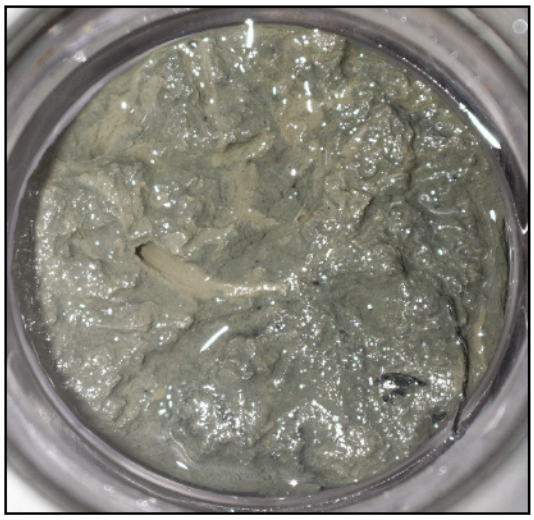

Sample 5

Table A-12c. Descriptions of the grain size distributions of physical samples, Core 12.

Sample	Depth [cm]	d10 [µm]	d50 [µm]	d90 [µm]	Fraction Clay	Fraction Silt	Fraction Sand
Core12_1	1.1	4.14	17.84	68.45	0.09	0.79	0.12
Core12_2	5.7	3.80	12.11	56.58	0.11	0.81	0.08
Core12_3	9.7	3.51	13.42	70.48	0.13	0.75	0.12
Core12_4	14.1	3.75	15.45	73.47	0.11	0.75	0.14
Core12_5	18.8	3.73	16.42	72.74	0.12	0.75	0.14

Figure A-12a. Cumulative grain size distributions for Core 12 physical samples.

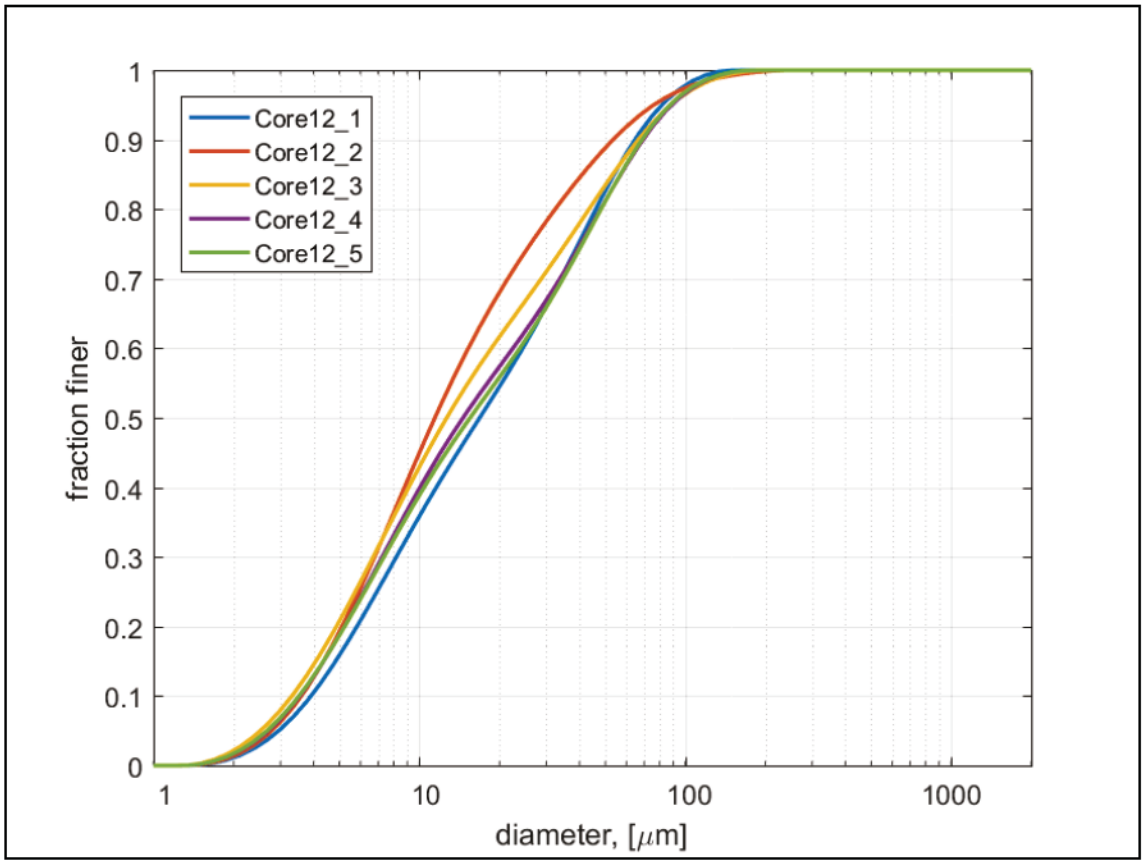

Figure A-12b. Grain size distributions for Core 12 physical samples.

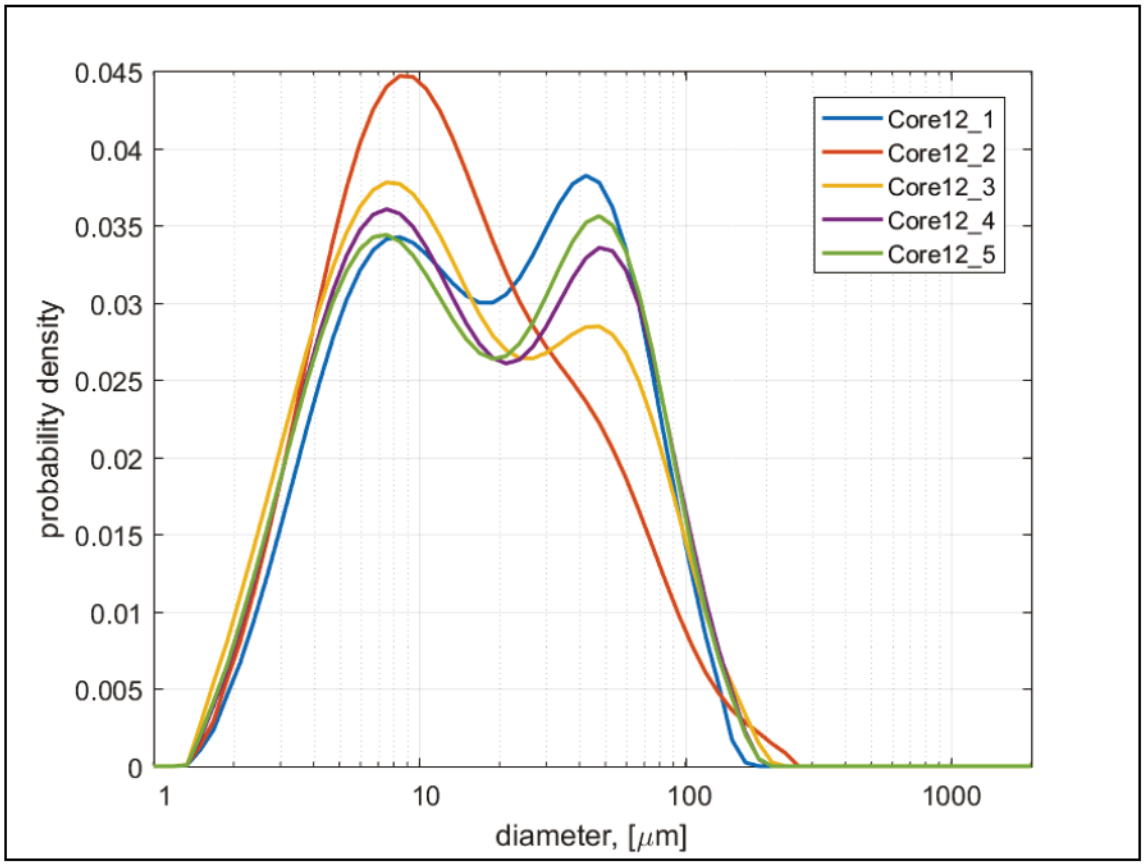

Figure A-12c. Erosion rate at a given applied stress versus depth down core (left). Class fractions and bulk density of physical samples (right) for Core 12.

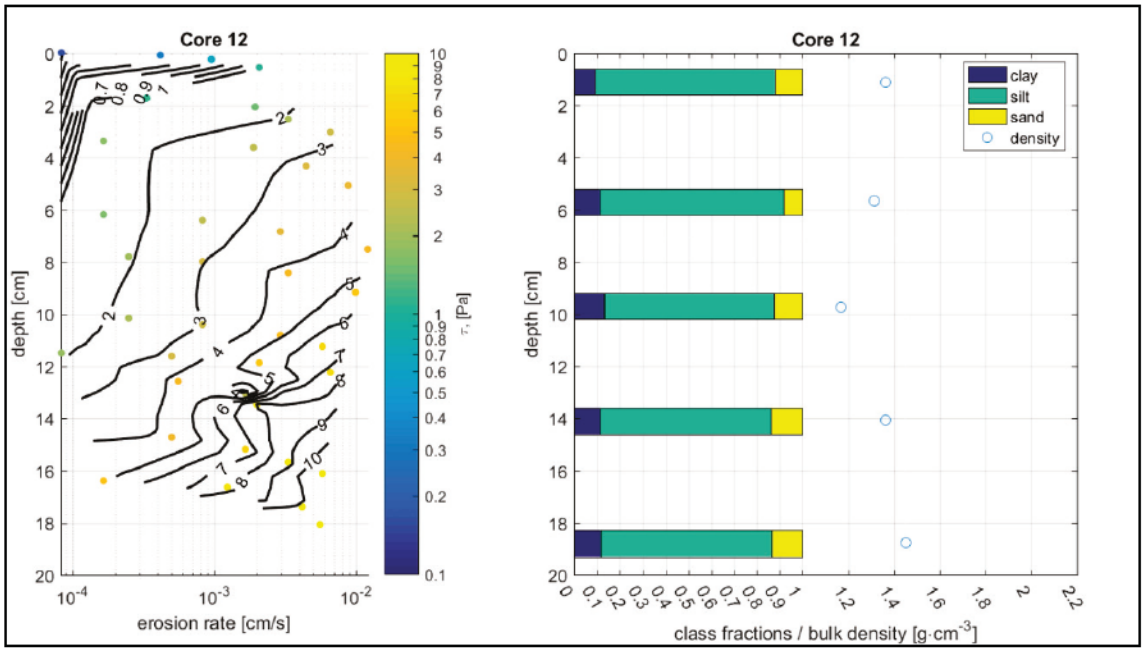

Figure A-12d. Erosion rate versus applied stress and resulting power law fit (s) for Core 12. Symbol color corresponds to depth down core.

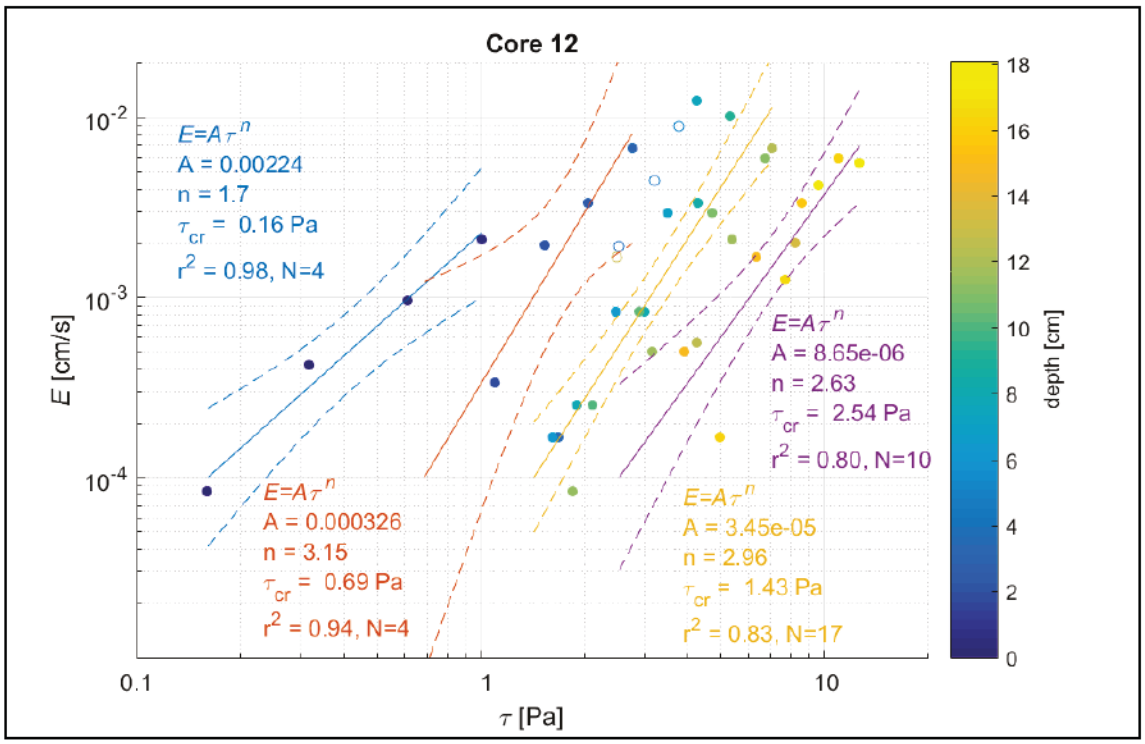

Table A-13a. Core description, Core 13.

Photograph	Description
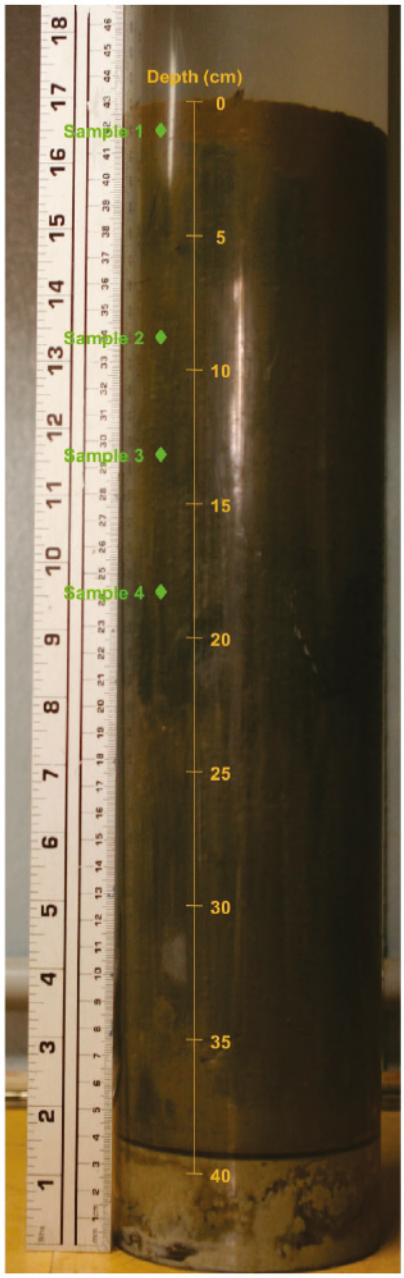	Overlying water. Smooth, slightly sloped surface composed of fine light brown sediment. Worm tubes and organic debris visible at surface. Sediment transitions to dark gray color approximately 2 cm down core. Bioturbation evident down to ~ 10 cm.

Table A-13b. Core surface photographs, Core 13.

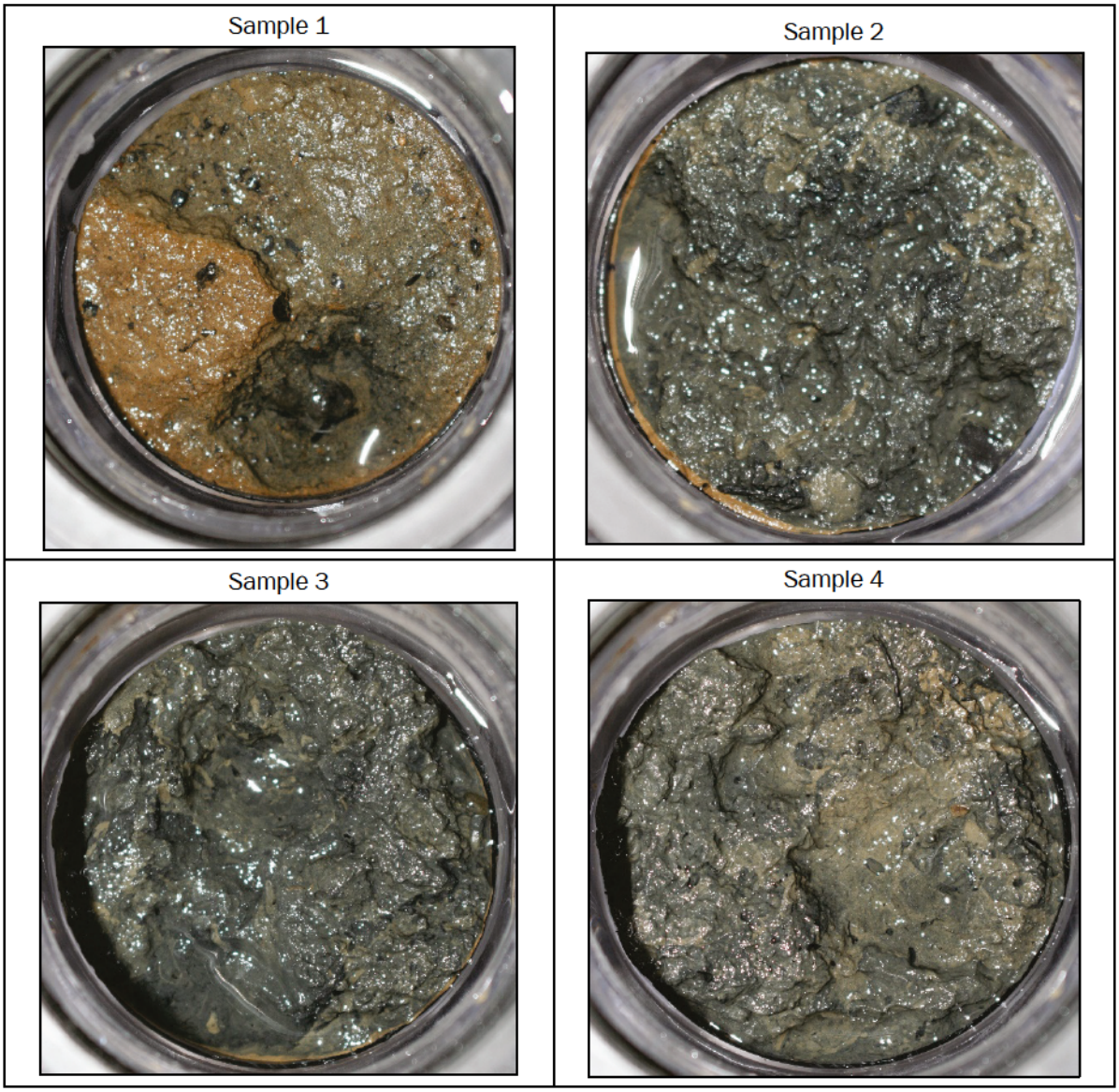

Table A-13c. Descriptions of the grain size distributions of physical samples, Core 13.

Sample	Depth [cm]	d10 [µm]	d50 [µm]	d90 [µm]	Fraction Clay	Fraction Silt	Fraction Sand
Core13_1	1.1	4.27	12.98	47.46	0.09	0.85	0.06
Core13_2	8.8	4.64	13.96	54.27	0.07	0.85	0.08
Core13_3	13.2	3.80	13.42	68.13	0.11	0.78	0.11
Core13_4	18.3	4.14	13.34	56.94	0.09	0.82	0.09

Figure A-13a. Cumulative grain size distributions for Core 13 physical samples.

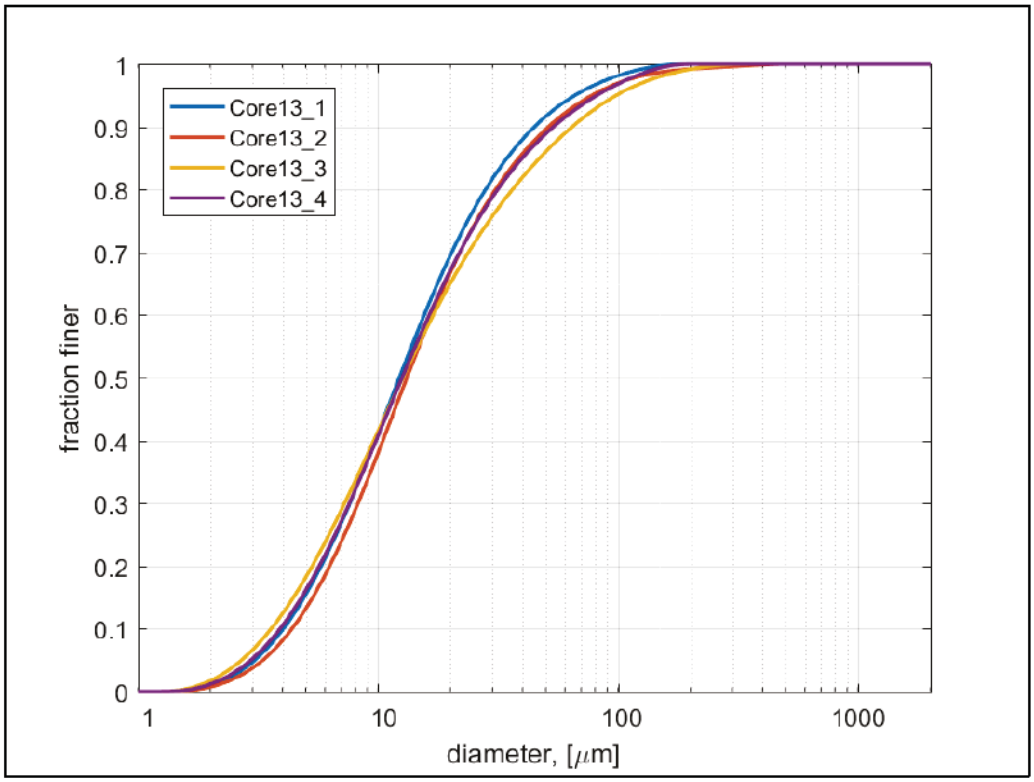

Figure A-13b. Grain size distributions for Core 13 physical samples.

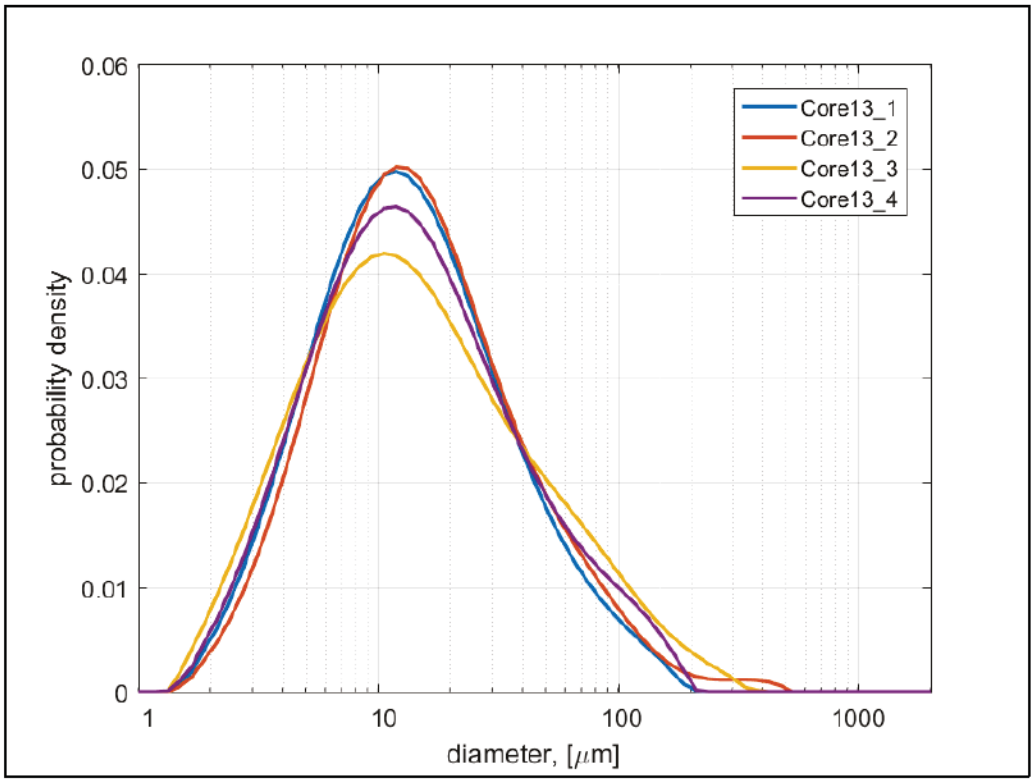

Figure A-13c. Erosion rate at a given applied stress versus depth down core (left). Class fractions and bulk density of physical samples (right) for Core 13.

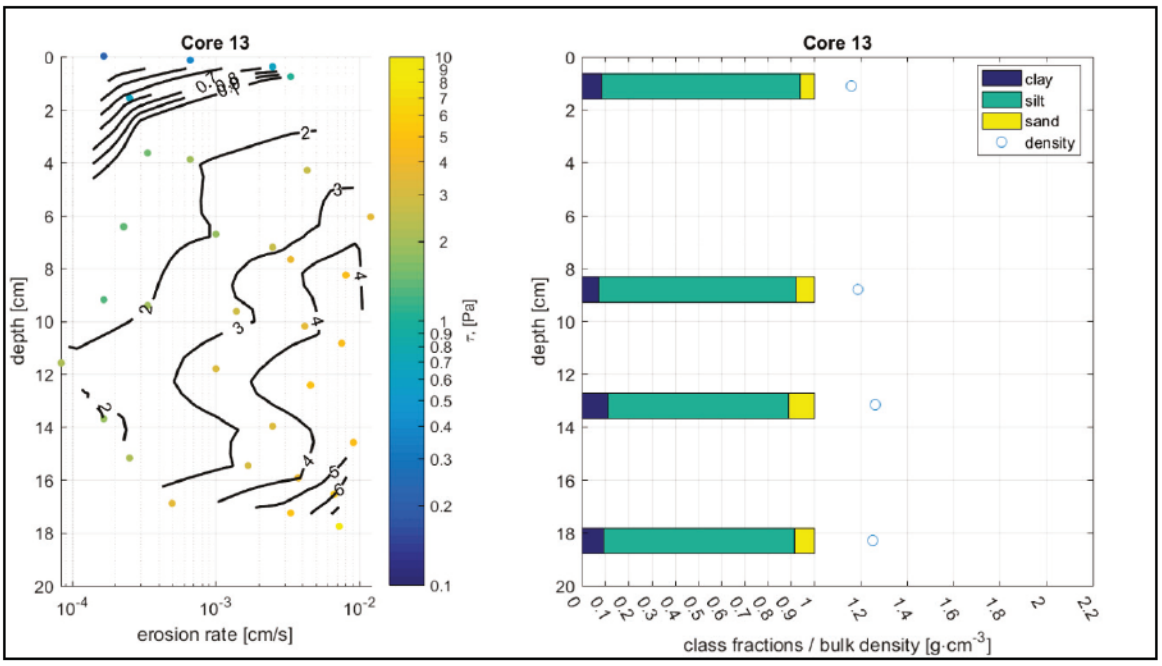

Figure A-13d. Erosion rate versus applied stress and resulting power law fit (s) for Core 13. Symbol color corresponds to depth down core.

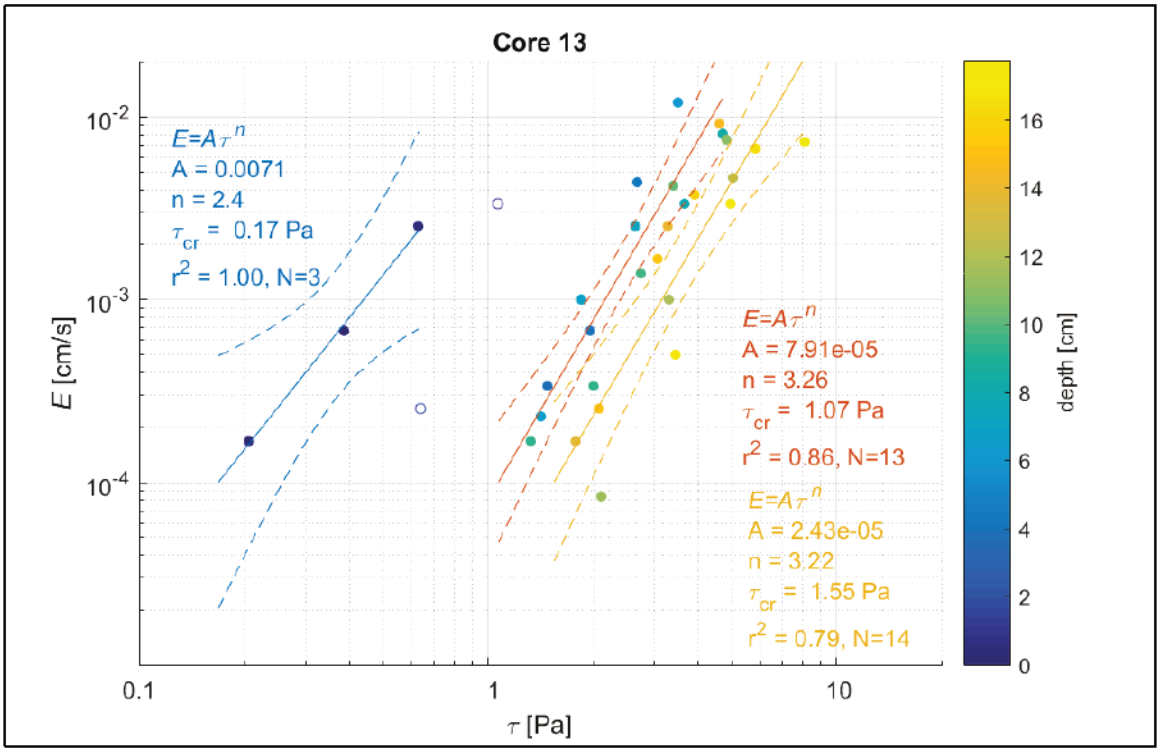

Table A-14a. Core description, Core 14.

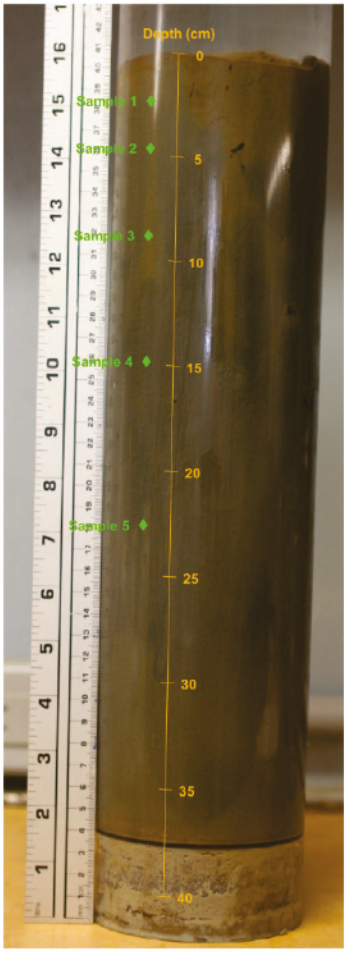	Overlying water.
	Slightly uneven surface with light brown coloration in top 1 cm.
	Grey coloration throughout remainder of the core. Visible bioturbation in the upper 2–3 cm. Small voids, ~1-5 mm in diameter, throughout the core.

Table A-14b. Core surface photographs, Core 14.

Sample 1

Sample 2

Sample 3

Sample 4

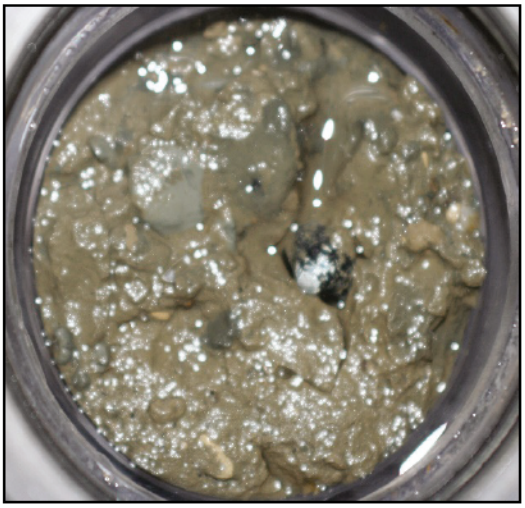

Sample 5

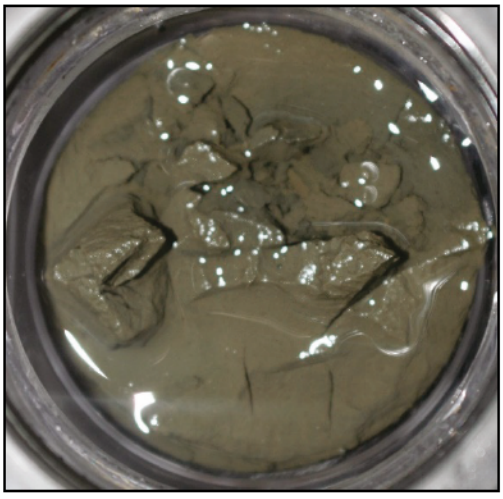

Table A-14c. Descriptions of the Grain Size Distributions of Physical Samples, Core 14.

Sample	Depth [cm]	d10 [µm]	d50 [µm]	d90 [µm]	Fraction Clay	Fraction Silt	Fraction Sand
Core14_1	1.4	4.36	15.49	62.64	0.08	0.82	0.10
Core14_2	4.7	4.67	15.44	59.51	0.07	0.84	0.09
Core14_3	9.3	4.48	13.99	51.02	0.08	0.85	0.07
Core14_4	14.9	4.14	16.20	203.23	0.09	0.70	0.21
Core14_5	22.9	4.45	13.38	48.46	0.08	0.86	0.06

Figure A-14a. Cumulative grain size distributions for Core 14 physical samples.

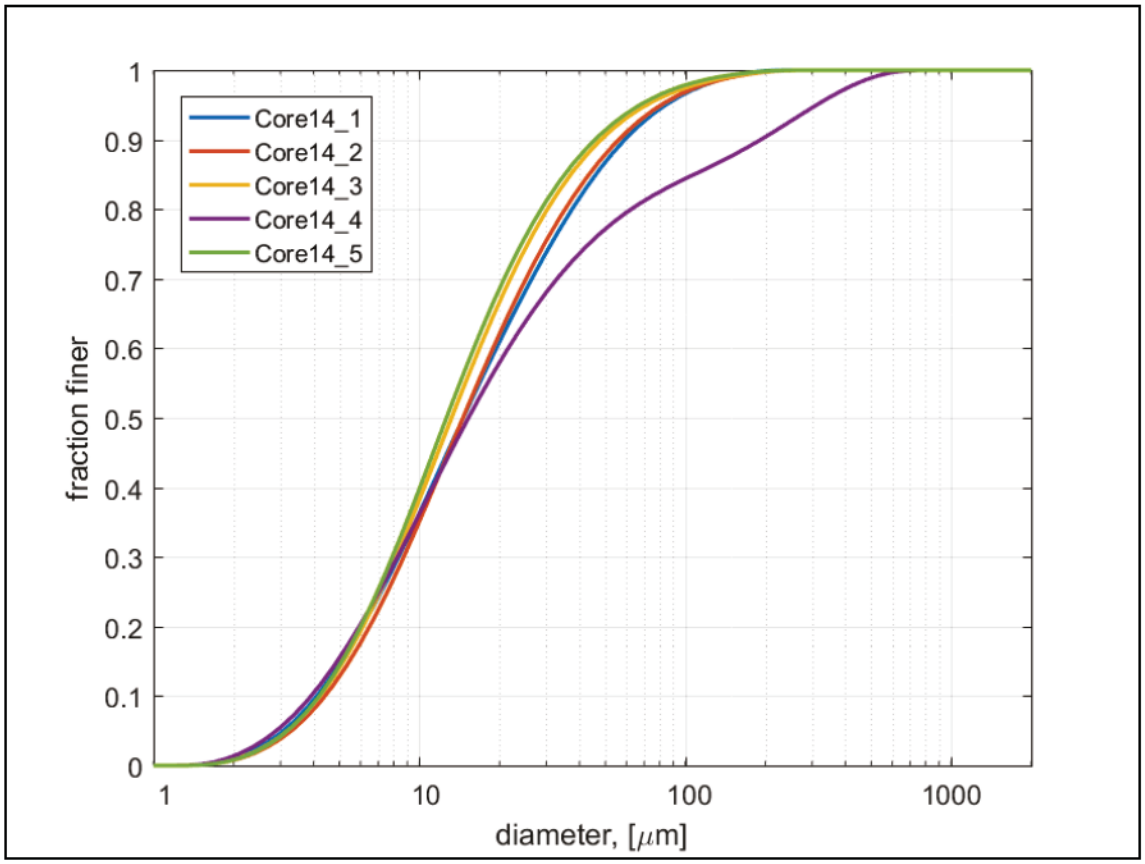

Figure A-14b. Grain size distributions for Core 14 physical samples.

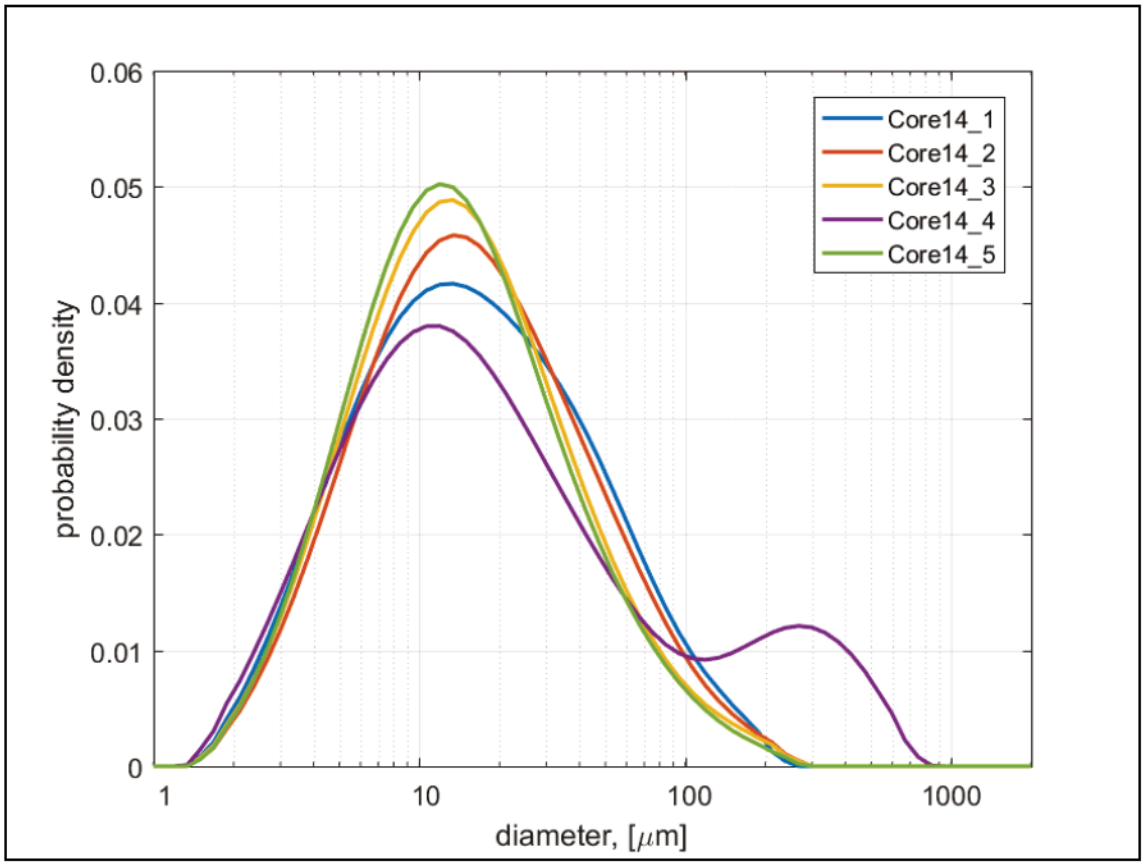

Figure A-14c. Erosion rate at a given applied stress versus depth down core (left). Class fractions and bulk density of physical samples (right) for Core 14.

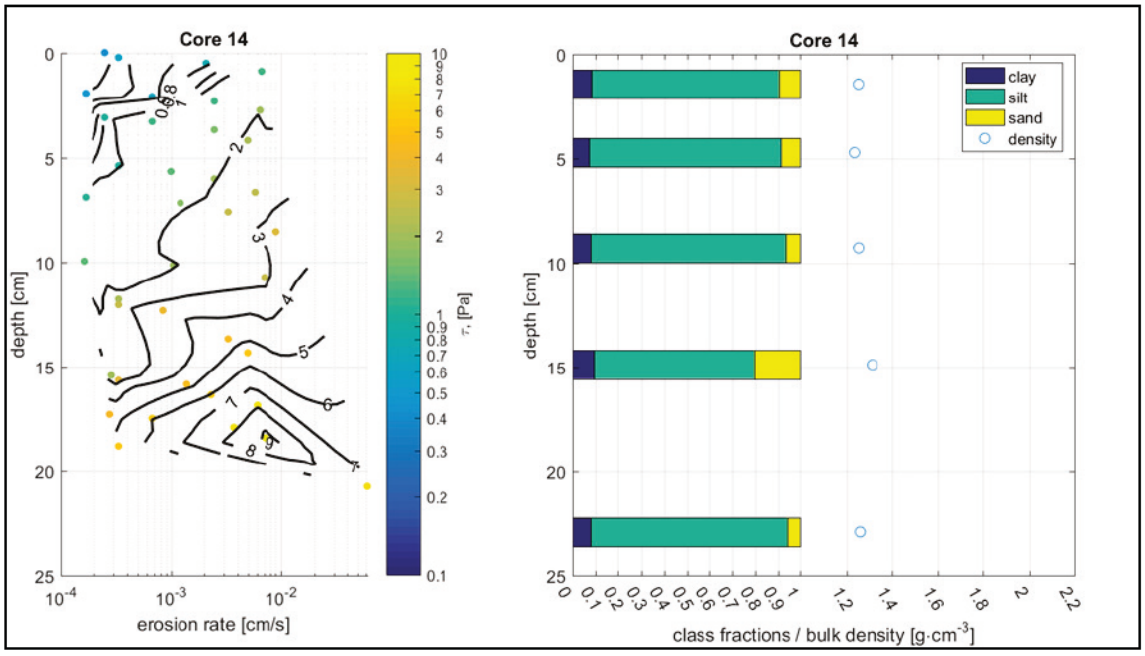

Figure A-14d. Erosion rate versus applied stress and resulting power law fit (s) for Core 14. Symbol color corresponds to depth down core.

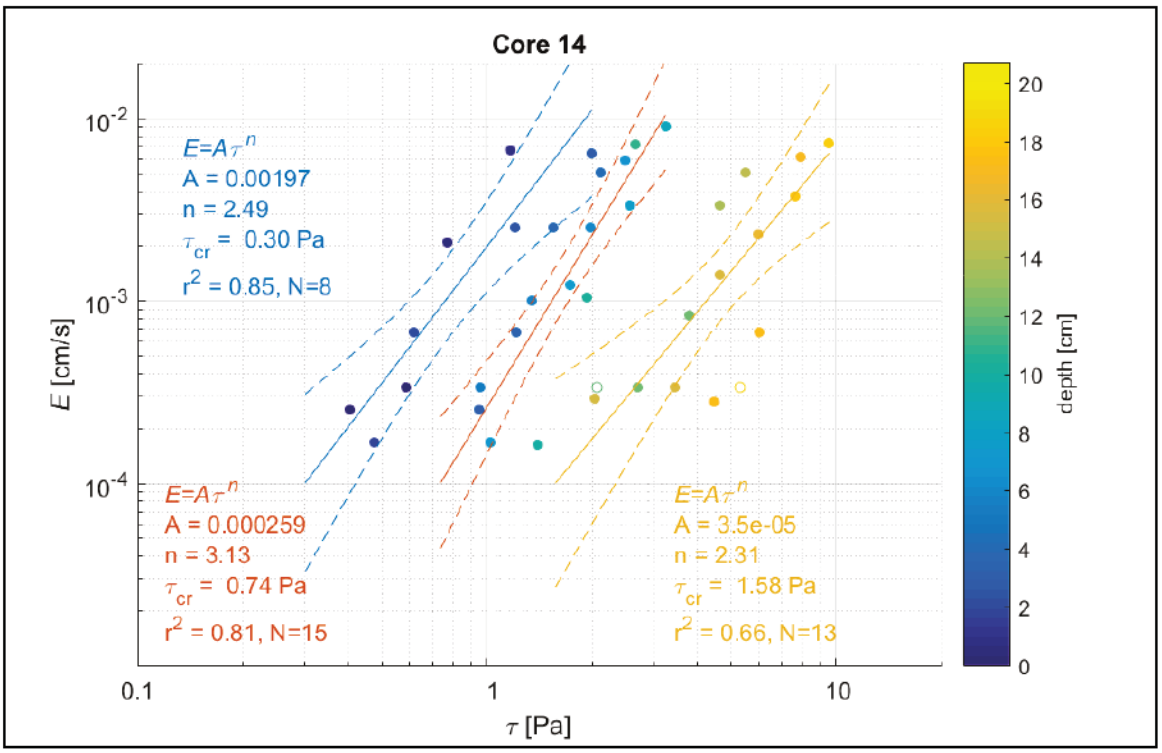

Table A-15a. Core description, Core 15.

Photograph	Description
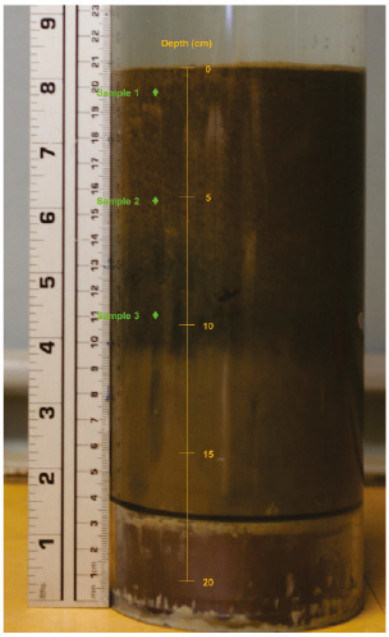	Overlying water. Smooth, level, sandy surface. Sediments with apparent sandy texture and brown-gray coloration dominate the upper 10 cm of the core. Sediment transitions to darker gray sandy material.

Table A-15b. Core surface photographs, Core 15.

Sample 1

Sample 2

Sample 3

Table A-15c. Descriptions of the grain size distributions of physical samples, Core 15.

Sample	Depth [cm]	d10 [µm]	d50 [µm]	d90 [µm]	Fraction Clay	Fraction Silt	Fraction Sand
Core15_1	1	19.81	196.10	333.56	0.01	0.16	0.83
Core15_2	5.2	93.00	204.63	337.43	0.01	0.08	0.91
Core15_3	9.7	3.93	17.31	122.94	0.10	0.71	0.19

Figure A-15a. Cumulative grain size distributions for Core 15 physical samples.

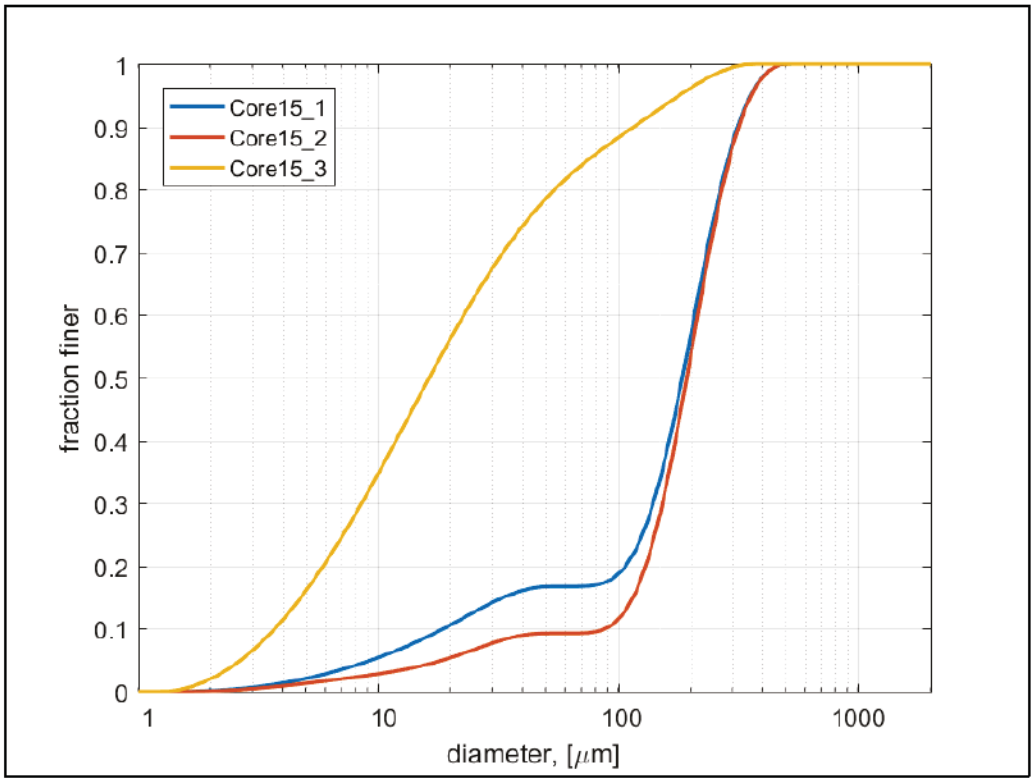

Figure A-15b. Grain size distributions for Core 15 physical samples.

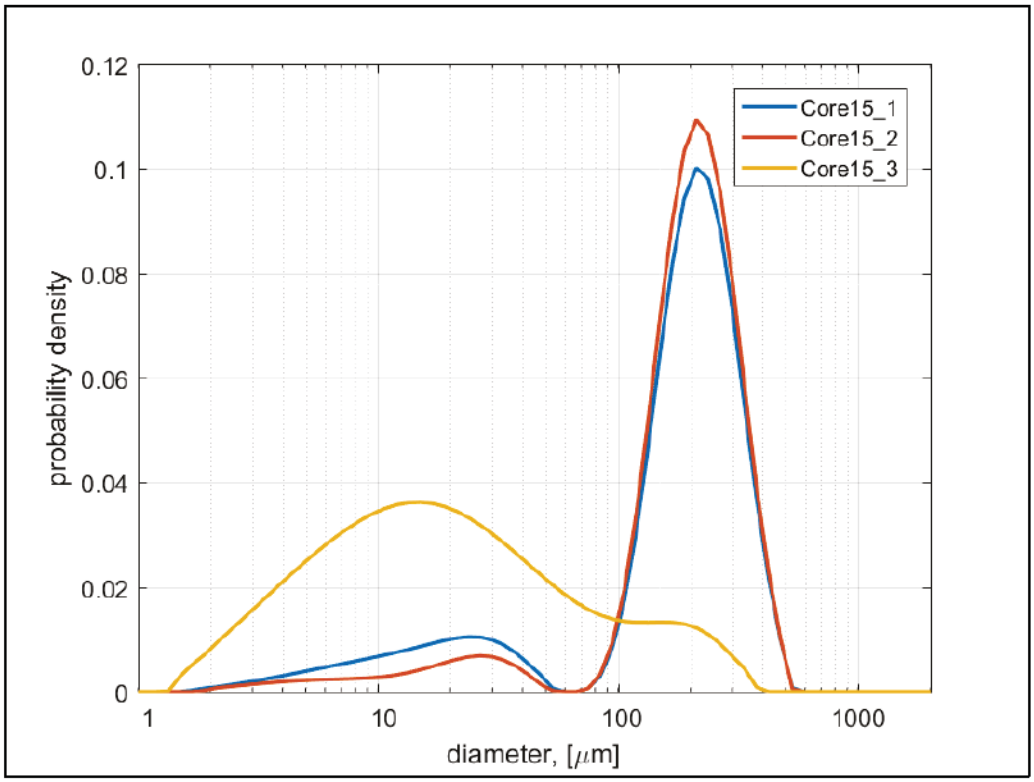

Figure A-15c. Erosion rate at a given applied stress versus depth down core (left). Class fractions and bulk density of physical samples (right) for Core 15.

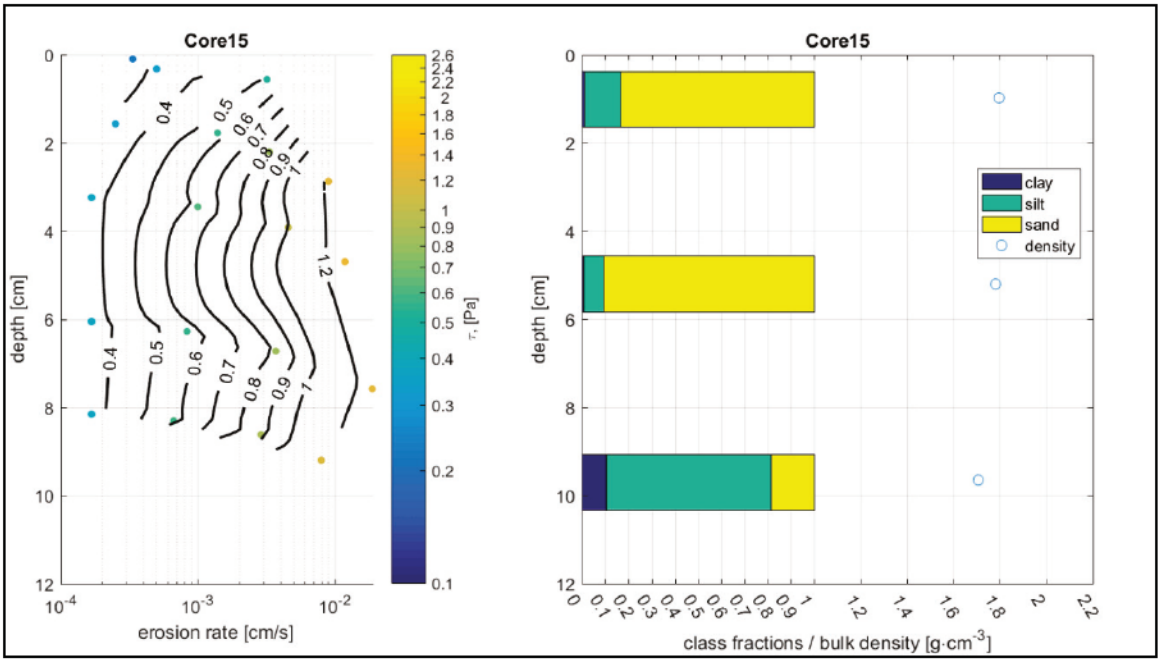

Figure A-15d. Erosion rate versus applied stress and resulting power law fit (s) for Core 15. Symbol color corresponds to depth down core.

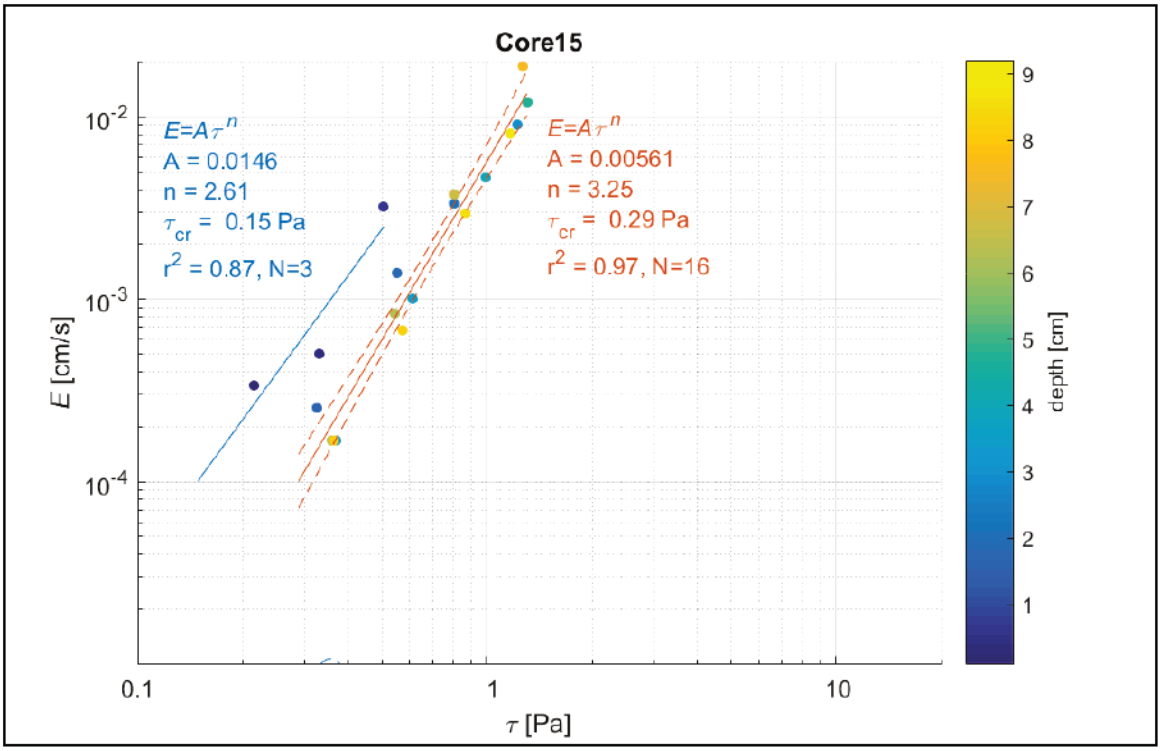

Appendix B: Aggregated and Disaggregated Size Distributions

Appendix B includes comparisons of aggregated (in situ) and disaggregated sediment size distributions (Figure B-1 through Figure B-8). The aggregated size distributions were determined by the Laser Diffraction (LD) method with a Laser In-Situ Scattering and Transmissometry (LISST-100x, Sequoia Instruments). Disaggregated size distributions are also determined by the LD method, but with a benchtop Malvern Mastersizer 2000.

Figure B-1. Aggregated (in situ, dashed) and disaggregated (solid) size distributions for samples collected at station PICS01 during Cast 01 (10 November 2017, ~0845 ET).

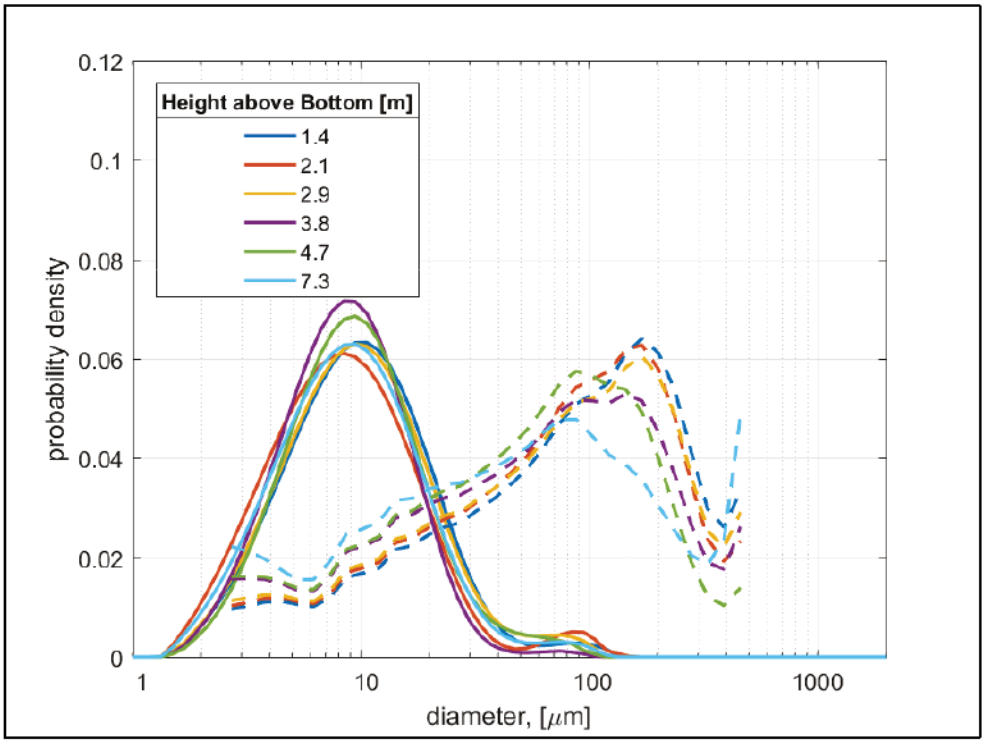

Figure B-2. Aggregated (in situ, dashed) and disaggregated (solid) size distributions for samples collected at station PICS01 during Cast 05 (10 November 2017, ~1100 ET).

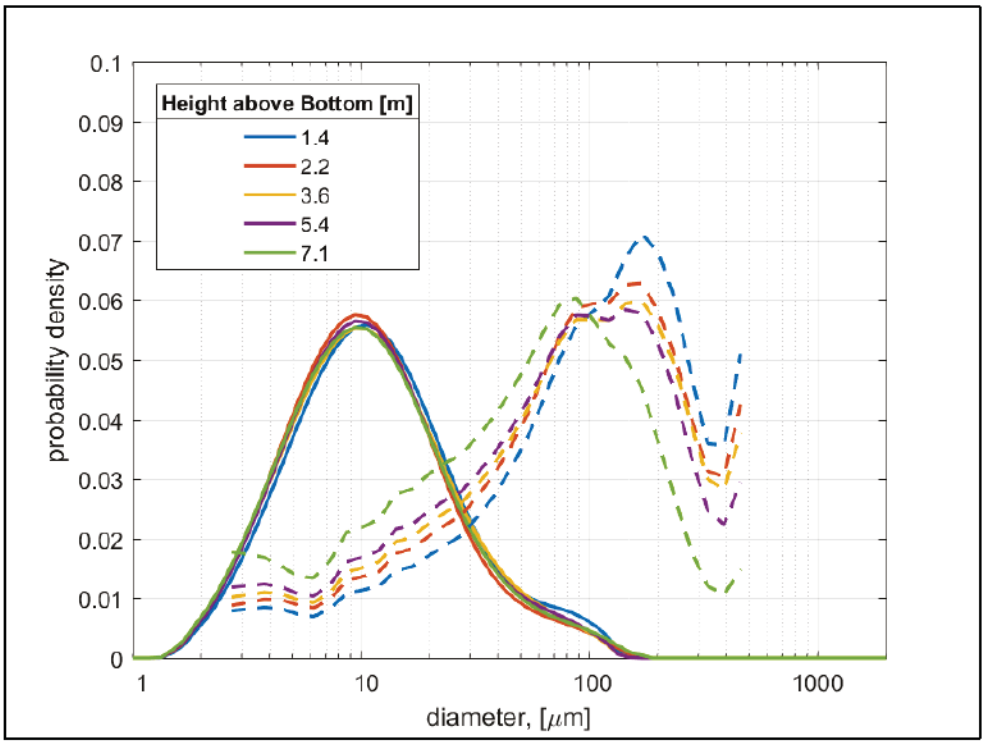

Figure B-3. Aggregated (in situ, dashed) and disaggregated (solid) size distributions for samples collected at station PICS01 during Cast 09 (10 November 2017, ~1300 ET).

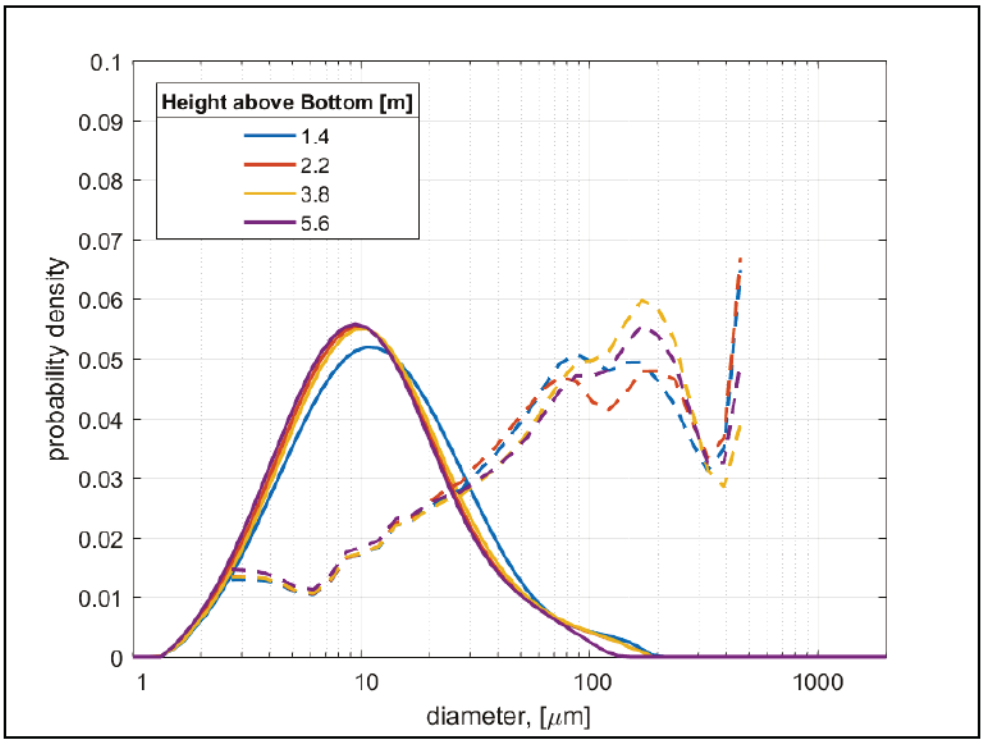

Figure B-4. Aggregated (in situ, dashed) and disaggregated (solid) size distributions for samples collected at station PICS01 during Cast 13 (10 November 2017, ~1500 ET).

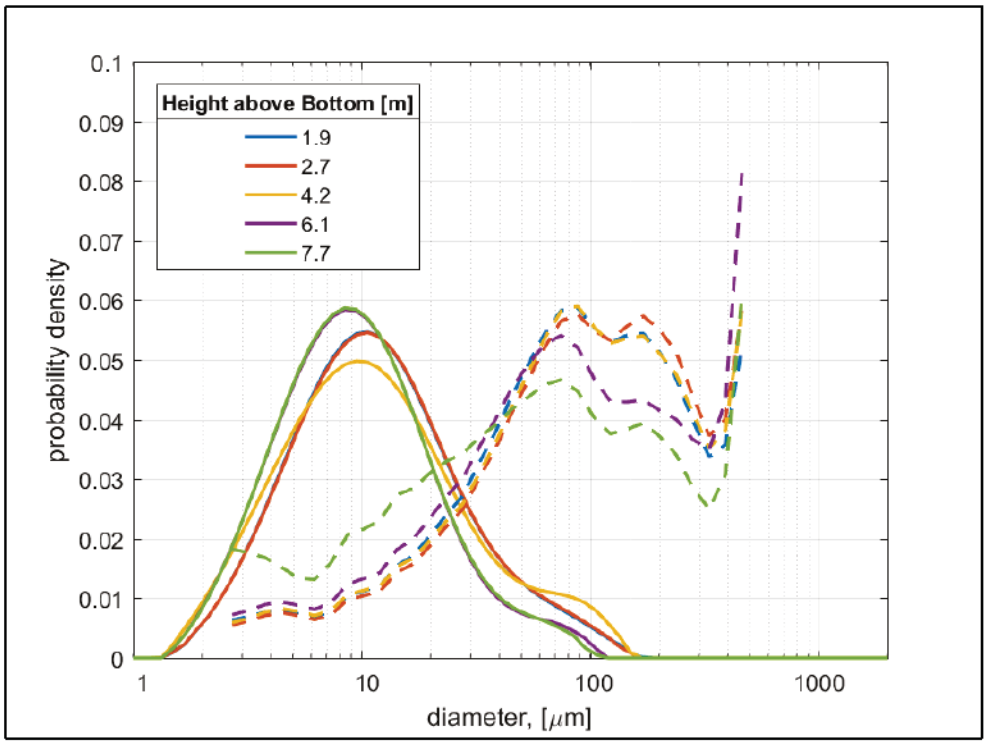

Figure B-5. Aggregated (in situ, dashed) and disaggregated (solid) size distributions for samples collected at station PICS02 during Cast 01 (11 November 2017, ~0915 ET).

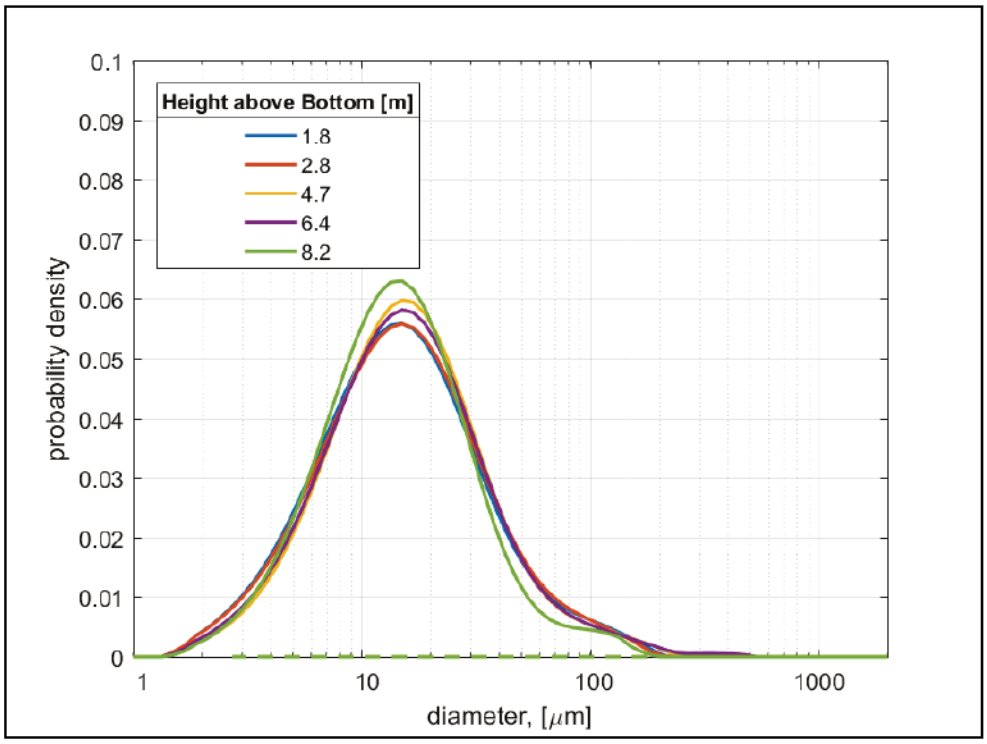

Figure B-6. Aggregated (in situ, dashed) and disaggregated (solid) size distributions for samples collected at station PICS02 during Cast 05 (11 November 2017, ~1115 ET).

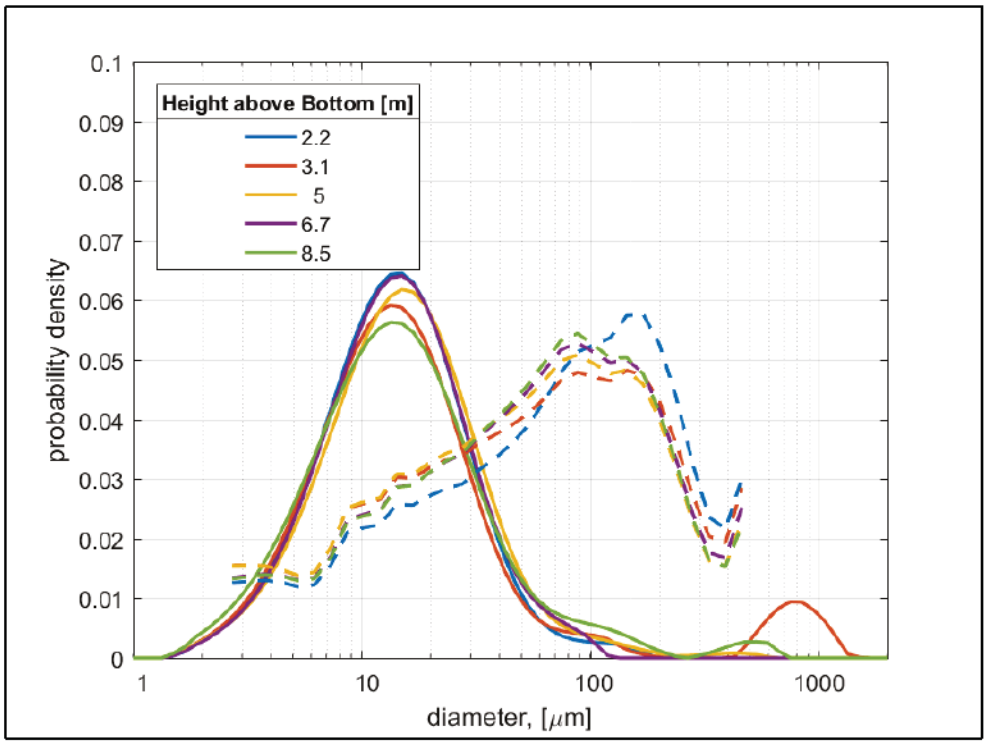

Figure B-7. Aggregated (in situ, dashed) and disaggregated (solid) size distributions for samples collected at station PICS02 during Cast 09 (11 November 2017, ~1315 ET).

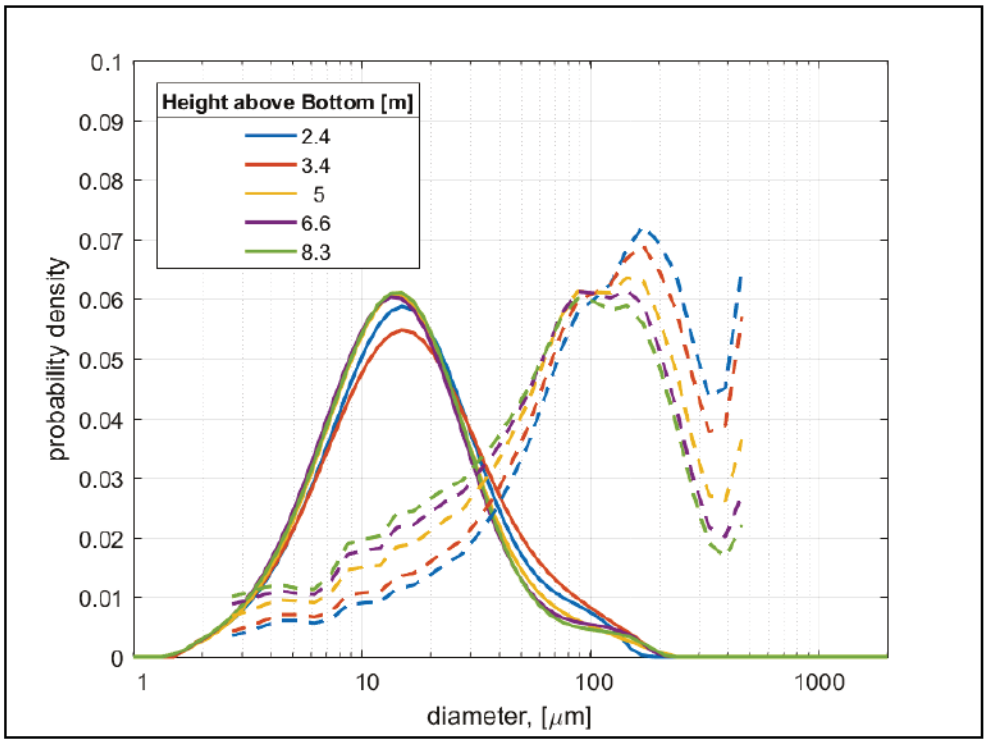

Figure B-8. Aggregated (in situ, dashed) and disaggregated (solid) size distributions for samples collected at station PICS02 during Cast 13 (11 November 2017, ~1515 ET).

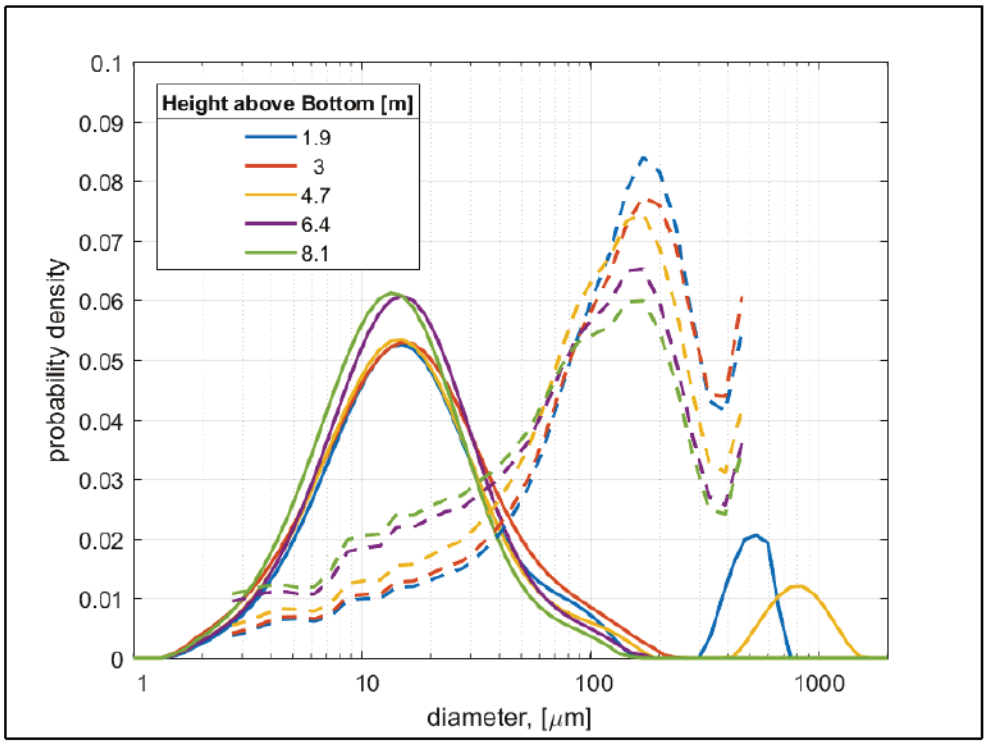

Acronyms and Abbreviations

CHL	Coastal and Hydraulics Laboratory
CTD	Conductivity-Temperature-Depth
ERDC	US Army Engineer Research and Development Center
LED	light-emitting diode
LISST	Laser In-Situ Scattering and Transmissometry
mab	meters above bed
NAO	Norfolk District
PICS	Particle Imaging Camera System
PIV	Particle Image Velocimetry
PTV	Particle Tracking Velocimetry
PVC	polyvinyl chloride
SSC	suspended sediment concentration
USACE	US Army Corps of Engineers

REPORT DOCUMENTATION PAGE

Form Approved
OMB No. 0704-0188

1. REPORT DATE	2. REPORT TYPE	3. DATES COVERED *(From - To)*
August 2021	Final Report	

4. TITLE AND SUBTITLE
Cohesive Sediment Field Study: James River, Virginia

5a. CONTRACT NUMBER

5b. GRANT NUMBER

5c. PROGRAM ELEMENT NUMBER

6. AUTHOR(S)
S. Jarrell Smith, David W. Perkey, and Kelsey A. Fall

5d. PROJECT NUMBER

5e. TASK NUMBER

5f. WORK UNIT NUMBER

7. PERFORMING ORGANIZATION NAME(S) AND ADDRESS(ES)
Coastal and Hydraulics Laboratory
US Army Engineer Research and Development Center
3909 Halls Ferry Road
Vicksburg, MS 39180-6199

8. PERFORMING ORGANIZATION REPORT NUMBER
ERDC/CHL TR-21-14

9. SPONSORING/MONITORING AGENCY NAME(S) AND ADDRESS(ES)
US Army Engineer Research and Development Center
Regional Sediment Management Program
Vicksburg, MS 39180-6199

10. SPONSOR/MONITOR'S ACRONYM(S)
ERDC RSM

11. SPONSOR/MONITOR'S REPORT NUMBER(S)

12. DISTRIBUTION/AVAILABILITY STATEMENT
Approved for public release; distribution is unlimited.

13. SUPPLEMENTARY NOTES
Funding Account Code U4356838; AMSCO Code 008303

14. ABSTRACT

Estuaries trap much of the fine sediment delivered to them by rivers. This phenomenon presents challenges to the US Army Corps of Engineers (USACE) navigation mission, which maintains navigable waterways for waterborne commerce through estuarine regions. The USACE Regional Sediment Management Program and the USACE Norfolk District are conducting a regional sediment transport modeling study to identify cost-effective sediment management schemes in the James River, a tributary estuary of Chesapeake Bay. A key element of the sediment transport modeling study is the definition of cohesive sediment transport processes, such as erosion and settling velocity. This report describes field-based measurements of cohesive sediment erosion and settling velocity conducted in November 2017. The team conducted erosion testing on 15 cores collected throughout the tidal system. Additionally, two anchor stations were occupied to measure tidal variations in vertical distributions of suspended sediment concentration, particle size, and settling velocity. Recommended cohesive sediment transport parameters were developed from the field measurements.

15. SUBJECT TERMS

Estuaries, James River (Va.), Sedimentation and deposition, Sediment transport, Suspended sediments

16. SECURITY CLASSIFICATION OF:			17. LIMITATION OF ABSTRACT	18. NUMBER OF PAGES	19a. NAME OF RESPONSIBLE PERSON
a. REPORT	b. ABSTRACT	c. THIS PAGE			S. Jarrell Smith
Unclassified	Unclassified	Unclassified	SAR	125	19b. TELEPHONE NUMBER *(Include area code)* 601-634-4310